TÉCNICO LISBOA

UNIVERSIDADE DE LISBOA

INSTITUTO SUPERIOR TÉCNICO

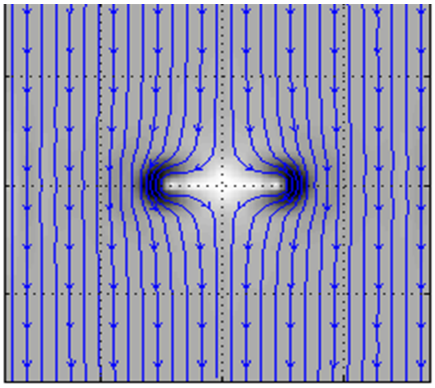

Characterization of Defects by Eddy Current Image Constructions

Dario Jerónimo Loureiro Pasadas

Supervisor: Doctor Artur Fernando Delgado Lopes Ribeiro
Co-Supervisor: Doctor Helena Maria dos Santos Geirinhas Ramos

Thesis approved in public session to obtain the PhD Degree in Electrical and Computer Engineering

Jury final classification: Pass with Distinction

Jury

Chairperson: Chairman of the IST Scientific Board

Members of the Committee:

Doctor Artur Fernando Delgado Lopes Ribeiro

Doctor Octavian Adrian Postolache

Doctor Francisco André Corrêa Alegria

Doctor Mário Fernando da Silva Ventim Neves

2017

UNIVERSIDADE DE LISBOA

INSTITUTO SUPERIOR TÉCNICO

Characterization of Defects by Eddy Current Image Constructions

Dario Jerónimo Loureiro Pasadas

Supervisor: Doctor Artur Fernando Delgado Lopes Ribeiro
Co-Supervisor: Doctor Helena Maria dos Santos Geirinhas Ramos

Thesis approved in public session to obtain the PhD Degree in Electrical and Computer Engineering

Jury final classification: Pass with Distinction

Jury

Chairperson: Chairman of the IST Scientific Board

Members of the Committee:

Doctor Artur Fernando Delgado Lopes Ribeiro, Associate Professor (with habilitation), Instituto Superior Técnico, Universidade de Lisboa

Doctor Octavian Adrian Postolache, Assistant Professor (with habilitation), Escola de Tecnologias e Arquitetura do ISCE-Instituto Universitário de Lisboa

Doctor Francisco André Corrêa Alegria, Assistant Professor (with habilitation), Instituto Superior Técnico, Universidade de Lisboa

Doctor Mário Fernando da Silva Ventim Neves, Assistant Professor, Faculdade de Ciências e Tecnologia, Universidade Nova de Lisboa

2017

Acknowledgments

My first acknowledgement is addressed to my supervisors, professor Artur Lopes Ribeiro and professor Helena Geirinhas Ramos. I want to thank them for all assistances and suggestions that they gave me during the PhD period in order to help to improve the quality of this thesis.

I have a special thanks to my colleagues and friends Tiago Rocha, Eduardo Pinheiro, Bruno Gil, Jose Goveia, Ruben Menezes, Chandra Angani and Prashanth Baskaran, for their help to overcome difficulties that arise during the work.

I also would like to thank all of my family for their continued support. I would like to send a special thanks to my wife, Ana Loureiro Pasadas, for all of her help and support during the last years.

Finally, this work was developed under the Instituto de Telecomunicacoes projects KeMANDE, OMEGA, EvalTubes and supported in part by the Portuguese Science and Technology Foundation (FCT) projects: PEst-OE/EEI/LA00008/2013, SFRH/BD/81857/2011. This support is gratefully acknowledged.

Abstract

Non-destructive testing (NDT) and evaluation (NDE) techniques are often employed for the inspection and evaluation of the material condition without impairing its future usefulness. The main purpose of this kind of technique is to provide information about the presence/absence, size and location of cracks in the inspected specimen. The tests are usually performed by skilled personnel. Whatever the method is used, the data presentations are very important to make a good judgement of the material state. Sometimes the detection of a crack is enough to substitute the material. In other cases, defect characterizations are required to evaluate the defect state to decide if the material must be substituted or not. The defect characterization is not easy to obtain, hence, defect features evaluation methods are still in investigation.

The work presented in this thesis combines several areas of knowledge, including electromagnetism, electronics, signal processing, inverse problems and image reconstruction methods to evaluate cracks in non-ferromagnetic conductive materials. The tests were performed in aluminium plates and stainless still tubes.

In the evaluation of cracks on aluminium plates, the involved electromagnetic phenomenon is based on the induction of eddy currents in metallic specimens, exploring the invariance of the primary excitation field for small spatial translations. Simulation and experimental tests were performed to investigate the magnetic field response and the eddy currents paths in the proximity of a metallic structure. New eddy current probes with planar coils and magnetic sensors were explored with the aim of improving the measurement of the perturbed magnetic field in the proximity of cracks. The planar coils architectures were designed to provide the uniform magnetic field in the magnetic sensor surroundings. The sensors used to measure the magnetic field were giant magneto-resistors (GMR)'s and anisotropic magneto-resistors (AMR)'s with high sensitivity to the magnetic field perturbations and wide frequency bandwidth response. The perturbations occurring in the measured magnetic field in the vicinity of a crack were used as the starting point of the investigation presented in this work. The setups, the implemented electronics, and the implemented signal processing methods that were used to perform the experimental tests are explained in detail. The determination of surface and subsurface crack's depths applying a uniform magnetic field distribution was studied. The work contains several simulation and experimental results which illustrate our main ideas. For the characterization of the cracks shape, an inversion problem algorithm was implemented to the measured magnetic field to obtain the path of the eddy currents surrounding the defect that provide relevant information about the defect geometry. The main idea was the achievement of the geometric profile of cracks using the path

of eddy currents surrounding the crack, when the sinusoidal excitation field with uniform magnetic field distribution was applied. Discrete Fourier Transform (DFT), Tikhonov and Total Variation (TV) regularizations were used to help in the application of the inverse problem solution. For our implemented inverse problem solution, the performance of the Tikhonov and Total variation regularizations were compared. The choice of an adequate regularization parameter value was required in order to obtain a stable solution in the reconstructed data. Two methods were applied and compared to estimate automatically the regularization parameter value. The feasibility of the implemented inverse problem solution in the evaluation of geometric defect characterization was demonstrated. An optimized probe was constructed to induce uniform currents with different orientations on the metallic surface without rotating the probe during the scan in order to improve the characterization of cracks with arbitrary geometric profiles.

Finally, simulations and experimental results were performed for the detection of cracks in stainless steel tubes. In that case, the remote field eddy current testing method was used to perform the tube tests. This method is based on the through-wall indirect coupling that allows the diffusion of the field both inside and outside the tube. Two remote field eddy current probes were built to compare detection and characterization capabilities in standard defects like longitudinal and transverse defects. The performance of GMR and AMR sensors for remote field eddy current testing in stainless steel tubes was compared.

Keywords

Non-destructive evaluation, eddy current testing, inverse problems, geometrical characterization of cracks, non-ferromagnetic conductive materials.

Resumo

Os ensaios não destrutivos representam um conjunto amplo de técnicas que são muito utilizadas para a inspecção da integridade dos materiais, potencialmente defeituosos/danificados, sem lhes causar qualquer dano. Estas técnicas servem para obter informações sobre a presença/ausência, tamanho e localização de defeitos nos materiais inspeccionados. Os ensaios não destrutivos são normalmente realizados por uma pessoa qualificada. Seja qual for o método utilizado, o modo de visualização dos resultados é muito importante para fazer um bom julgamento do estado do material. Nalguns casos, a detecção de um defeito é suficiente para avaliar o estado do material e solicitar a substituição do material danificado. Nos restantes casos, a avaliação das características dos defeitos é necessária de modo a determinar a longevidade do material. A avaliação do estado do material com defeitos continua a ser um problema bastante complexo, e por isso, novos métodos de avaliação continuam a ser investigados para melhorar a caracterização actual dos defeitos.

O trabalho apresentado nesta tese associa várias áreas de conhecimento, abrangendo o electromagnetismo, a electrónica, o processamento de sinal, os métodos de inversão e de reconstrução de imagem para avaliar fissuras em materiais condutores não-ferromagnéticos. Os ensaios foram realizados em placas de alumínio e tubos de aço inoxidável.

Na avaliação de defeitos em placas de alumínio, o fenómeno electromagnético envolvido é baseado na indução de correntes de Foucault no material em teste, explorando a invariância do campo primário aplicado para pequenas translações espaciais. Simulações e ensaios experimentais foram realizados para investigar a resposta do campo magnético na proximidade de uma estrutura metálica assim como, as correntes de Foucault induzidas no material. Foram investigadas novas sondas com bobinas planares e sensores magnéticos a fim de melhorar a medição do campo magnético perturbado na proximidade de uma fissura. A arquitectura das bobinas planares foi especialmente desenhada para criar um campo magnético uniforme em torno de um sensor magnético posicionado no centro da região uniforme. Os sensores utilizados neste trabalho para a medição do campo magnético foram as magneto-resistências gigantes e as magneto-resistências anisotrópicas. Estes sensores foram escolhidos por possuírem uma alta sensibilidade à variação de campo magnético que não depende da frequência. As perturbações ocorridas no campo magnético medido na proximidade de uma fissura foram utilizadas como ponto de partida da investigação apresentada nesta tese. O sistema de medida, a electrónica implementada e os métodos de processamento de sinal implementados para a realização dos testes experimentais estão explicados em detalhe neste documento. Foram realizadas simulações e testes experimentais para a determinação das profundidades

das fissuras a partir da medição do campo magnético perturbado aplicando uma campo de excitação com distribuição uniforme. Para a caracterização da forma geométrica da fissura, foi resolvido o problema de inversão do campo magnético medido, de forma a determinar a configuração espacial das linhas de corrente no material. A transformação de Fourier discreta, assim como as regularizações por Tikhonov e por variação total foram usadas para ajudar na resolução do problema inverso. O desempenho dos dois métodos de regularização foi comparado. Devido às exigências dos métodos de regularização necessários no processo de inversão, a escolha apropriada do parâmetro de regularização foi necessário para obter uma solução estável nos dados reconstruídos. Dois métodos foram implementados para estimar automaticamente o valor do parâmetro de regularização. A avaliação da caracterização da forma geométrica dos defeitos a partir dos dados reconstruidos foi demonstrada. Uma sonda optimizada foi construída para induzir correntes uniformes com diferentes orientações sobre a superfície metálica sem rodar a sonda durante o teste, a fim de melhorar a caracterização da forma geométrica das fissuras mais complexas.

Por fim, foram realizadas simulações e testes experimentais em tubos de aço inoxidável. Nesse caso, o método de ensaio de corrente de Foucault de campo remoto foi utilizado para realizar os ensaios. Este método é baseado no acoplamento indirecto existente na parede do tubo que permite a difusão do campo com a mesma intensidade tanto na parede de dentro como na parede de fora do tubo. Duas sondas foram construídas para testar o desempenho das magneto-resistências gigantes e das magneto-resistências anisotrópicas na detecção de defeitos longitudinais e transversais em tubos. Os resultados obtidos são apresentados e os desempenhos das duas sondas são comparados.

Palavras Chave

Ensaios não destrutivos, correntes de Foucault, problemas inversos, caracterização geométrica de defeitos, materiais condutores não-ferromagnéticos.

Contents

List of Figures

List of Tables

List of Acronyms

AMR	Anisotropic Magnetoresistors
DC	Direct Current
ECT	Eddy Current Testing
ECP	Eddy Current Probe
GMR	Giant Magnetoresistors
FEM	Finite Element Method
NDE	Non-Destructive Evaluation
NDT	Non-Destructive Testing
RFECT	Remote Field Eddy Current Testing
SDP	Standard Depth of Penetration
SQUID	Superconducting Quantum Interference Devices
ACFM	Alternating Current Field Measurement
TFD	Truncated Fourier Decomposition
TV	Total Variation
DFT	Discrete Fourier Transform

1

Introduction

Contents

1.1 Motivation

Non-destructive testing (NDT) represents an important role in the maintenance of components for several industries, where many techniques of non-destructive testing are used to inspect and analyse potential defects in an object or material without impairing its future usefulness [1].The term non-destructive evaluation (NDE) is also used to describe this techniques. They involve different principles according to their purpose. Eddy current testing (ECT) technique is widely used to detect and localize defects, and non-destructive evaluation activity is related not only with detection and localization, but also with a characterization of the defect in metallic structures. However, this technique still needs to be improved. The determination of geometric characteristics about defects and their depth using this technique are not completely solved. In the last two decades, the progress of magnetic sensors technology has been attracting researchers to study the sensor performance on NDE. Nowadays, industries like aerospace, railways, nuclear or pipelines are examples of industries that need a hard inspection in their equipments and structures to provide safety, security, and productivity for the companies and their customers. To this purpose, this work deals specifically about ECT based on electromagnetic phenomenon to test metallic structures.

1.2 State of the Art

In this thesis the characterization of defects inside conductive non-ferromagnetic materials is made using the eddy current phenomenon and imaging methods. Eddy current testing (ECT) is an effective method to detect and analyse defects caused by stress or corrosion on the metallic surfaces [2–6]. It is based on the electromagnetic principles. A time-varying magnetic field is generated in the metal proximity and eddy currents are induced in the metallic surface. The induced eddy currents intensity diminishes exponentially with the material depth [7, 8]. In the presence of structural defects, the eddy currents are deviated from their normal geometrical configuration, and the magnetic field perturbation produced by these eddy currents can be measured by magnetic sensors. The magnetic field can be applied by a wire loop where an electric current circulates with different time-varying forms, such as sinusoidal [9–11] or pulsed [12, 13]. The excitation may be also produced by velocity induction [14, 15] using a motion of a DC magnetic field. The sinusoidal excitation benefits from working in a steady-state periodic regime, while the pulsed and velocity excitation are usually analysed in the time-domain. Several types of eddy current probes (ECPs) are used to evaluate the surface under test and each one is adapted according to its purpose. Each probe needs a magnetic field detector/sensor to measure the magnetic field perturbation originated by the presence of defects inside the metal. The signal obtained from this magnetic sensors can contain unwanted noise that affects the correct judgement of the material state. To interpret correctly the signal obtained from a magnetic sensor, it is essential to take into account the unwanted noise that affects the relevant signal information. The two common sources of these unwanted signals are the lift-off effect [11, 16, 17] and the edge effect [18]. The lift-off effect occurs when it is not possible to keep a constant distance between the probe and the metallic plate under test. The non-constant distance between the probe and the metal under inspection can

be caused by the irregularity of the material surfaces or by the probe movement during the inspection. The edge effect occurs when the probe is in the proximity of the edges, corners or ends of the metal under inspection. In that situations, the patterns of eddy currents are obstructed and the measurement of magnetic field is affected. The influence of this effect depends on the coil dimensions, the material properties and the test frequency.

To evaluate a metal surface using the eddy current testing method, a simple probe solution to detect eddy currents can be made by measuring the impedance of the excitation coil. However, this method provides low sensitivity and low resolution. Differential inductive eddy current probes (ECPs) based on excitation/detection pickup coils are currently used to detect and characterize flaws in metallic structures. An excitation coil is used to induce eddy currents in the conductor and two sensing coils are used as detectors to measure the values of the magnetic flux density inside the excitation coil. The two sensing coils are connected in series and they are in opposite winding directions, in order to attenuate the noise effect and to only measure the differential voltage between the two sensing coils. This ECP is very sensitive to detect the eddy currents perturbation near the surface under test [19]. However, the sensitivity of the pickup coils is proportional to the excitation frequency, and their use as sensing elements is insufficient to detect deep subsurface defects. The low excitation frequency required to make the eddy current penetrate deeply enough into the material is the main disadvantage of this probe. The increasingly importance of industries that need a hard inspection in their equipments and structures has caused significant progress on the technological development of other magnetic sensors as sensing elements. Solid-state magnetic sensors such as superconducting quantum interference devices(SQUID) [20–22], flux-gates [23], Hall sensors [24], anisotropic magnetoresistors (AMR) [25, 26] or giant magnetoresistors (GMR) [26, 27] have been introduced in eddy current systems as an alternative to detect coils, giving better sensitivity to low frequency signals. Each one is adapted to a probe according to their costs, size and characteristics. Table 1 summarizes the specifications of the magnetic sensors above mentioned.

Table 1.1: Magnetic Sensors Specifications.

Magnetic Sensors	**Sensitivity**	**Magnetic Field Range**	**Frequency Bandwidth**
Pick-up Coil	$\frac{d\Phi}{dt}$	≈1 nT to more than 10 T	≈3 kHz to more than 5 MHz
SQUID	Φ	≈1 pT to 1 T	DC to 10 kHz
FLUXGATE	B	≈10 nT to 1 mT	DC to 1 kHz
Hall	B	≈ 1 mT to 10 T	DC to 10 kHz
AMR	B	≈10 μT to 1 T	DC to 1 MHz
GMR	B	≈1 μT to 10T	DC to 1 MHz

The SQUID sensor is the most sensitive detector of magnetic flux signal using low frequency signal (DC to 10 kHz), and seems to be the best sensor to complement the low efficiency of the detector coils in the detection of sub-surface defects. However, due to their unavoidable higher cost and huge size due to the required refrigeration, the SQUID sensors are not widely used in non-destructive evaluation. The discovery of magnetoresistive effects has allowed the development of small solid-state magnetic sensors such as AMR sensors and GMR sensors that have constant high sensitivity to the variation of magnetic field along their wide bandwidth. The use of magnetoresistive

sensors as sensing element can replace more expensive sensors and can be easily embedded in low cost systems. Our prior investigation presented a low cost system using a planar coil with sinusoidal excitation and a GMR sensor to detect surface and sub-surface cracks in conductive material [28]. The use of a planar coil that provides an uniform contact between probe and the surface plates under test allowed to obtain less lift-off effect than other conventional probes. The commercial equipment used in manual inspection presents an output curve on a display, usually referred as a signature. These typical crack signature obtained by a commercial equipment that use eddy current testing with pick-up coil probe was compared with two low cost systems using GMR probes to detect sub-surface cracks in a metallic plate[29].

The methods used to relate the measured signals with the defect characteristics can be divided in two types: phenomenological methods and methods based on mathematical algorithms [30]. The first method solves the so-called direct problem, where a model of the acquired signal is solved for a known material defect and it is compared with the experimental measures obtained. After this comparison, the shape of the defect is changed until it minimizes the difference between the two sets of data. This process is repeated iteratively until the error is inferior to a pre-defined maximum value. The second method uses mathematical algorithms to identify signatures containing information relative to the defect characteristics. Such examples are based on neural networks [31] or other classification methods based on automatic learning [32, 33]. Our prior work presented a support vector machine (SVM) approach using pulsed eddy current method for assessing metal plate thickness [33]. The presented approach has permitted to realize good plate thickness classification and estimation up to 6 mm thickness plate with classification errors lower than 1.52%.

Uniform magnetic field probes referred by Koyama [34] has shown good results in weld defect detection. Also, a non destructive system based on uniform current distribution was already patented [35]. This technique requires a metal inspection under different probe angles due to the impossibility to detect small cracks that are parallel to the induced current flow. Despite this requirement, the use of an alternating current with a spatially uniform excitation current to create a spatially uniform current distribution on the metal surface makes the current flow more predictable, simplifying the interpretation of the magnetic field perturbation when a defect is present in the metal. Recently, the alternating current excitation with uniform path was applied in a moving rail to detect notches in rail grade steel [36]. This technique got good results in the detection of surface notches with different shapes and sizes. Another work concerning this technique was applied by a probe with a sensor array for pipe crack inspection [37]. The sensor array was mounted along the inner circumference of the probe to improve the detectability of the cracks. The term alternating current field measurement (ACFM) is also widely used to describe this technique. Researchers have investigated the use of planar probe using uniform current distribution in order to characterize defects in metallic specimens [38]. Recently, a planar probe with a rotating electromagnetic field excitation and GMR sensors shows uniform sensitivity by detecting cracks in all radial directions around fastener holes and in getting the information of the crack orientation [39].

In this thesis, a special attention is paid to the presentation of results in the form of eddy current

density images, in order to characterize the size and the geometry of cracks in non-ferromagnetic materials. A scanning system was used to create a two-dimensional image of the magnetic field perturbation around a plate with defect. From this two-dimensional image, researchers have already shown that the size and the orientation of the defect can be estimated. However, the defect geometry is not directly visible in the obtained image. In this work, an inverse problem was solved to obtain the two-dimensional image of the eddy current distribution inside the material under test in order to improve the characterization of defect geometries. The method involved the determination of the transformation kernel and the application of regularization algorithms that are based on image reconstruction techniques [40]. Several regularization methods are used in inverse problems in imaging and each one is adapted according to its purpose. Truncated Fourier decomposition (TFD)regularization and Tikhonov regularization are the most commonly used regularization methods of ill-posed problems or ill-conditioned problems. In inverse problems applications, both regularization methods work as low-pass filters in order to restore the desired image. As example, a experimental and simulation study of image reconstruction with Tikhonov regularization and simultaneous iterative reconstruction techniques presented satisfactory conductivity results [41]. However, Tikhonov and TFD regularizations are not well suited to deal with data non-homogeneities. For this type of imaging problems, a regularization solution called total variation (TV) can be used to penalize highly oscillatory solutions preserving the edges present on the restored image [42].

1.3 Objectives

The aim of our research is the detection and determination of geometrical characteristics of surface and subsurface defects in conductive non-ferromagnetic plates and tubes. The procedures used to meet these objectives were:

- Literature review of articles based on non-destructive testing (NDT) and eddy current testing (ECT).
- Identification of the type of equipments needed to meet the objectives.
- Choice of the appropriate sensors for the detection and characterization of defects in the metallic plates in analysis.
- Construction of probes able to produce a magnetic field with uniform distribution.
- Design of several defects to be machined on plate and tube materials for experimental tests.
- Acquisition of experimental results.
- Comparison between the experimental and simulation results.
- Development of inversion algorithms able to reconstruct the eddy currents inside the material under test.
- Estimation of the defect geometrical characteristics, such as length, width and depth.

1.4 Relevant Work Tasks

In the presented work, we are considering the characterization of defects inside conductive non-ferromagnetic materials using eddy currents and imaging methods. As a consequence, the most relevant work made to accomplish the characterization of the defects is briefly introduced in the next subsections.

1.4.1 Design of Defects

Homogeneous sample plates and sample tubes were acquired to make experimental tests. Several defects at several depths of material were machined to provide experimental samples to be tested with the built probes and to evaluate defect depth, length and width. All defects were designed in our laboratory, however some were machined in a mechanical workshop.

1.4.2 Probes Construction

In eddy current testing, each probe includes one excitation coil and a magnetic sensor to measure the magnetic perturbations around a metal that needs to be evaluated. In this work, the planar coils were designed and built taking into account the inverse problem algorithm that was necessary to obtain information of the eddy current distribution in the material under test. The planar coil has a zone with uniform current distribution, where a magnetic sensor is located. When a time-varying excitation current is applied to the excitation coil, a spatially invariant field around the sensor is measured. In the presence of a defect, the eddy current uniformity is perturbed and these perturbations are essential in the inverse problem solution presented in this work. Giant magnetoresistors (GMR) and anisotropic magnetoresistors (AMR) were chosen as magnetic sensors due to their high constant sensitivity along a wide frequency bandwidth (from DC to 1 MHz) that allows easy detection of superficial defects at higher frequencies and sub-superficial defects at lower frequencies. The built probes are presented in chapter 5 . Other probes were built to inspect tubes in order to test the performance of the GMR and AMR sensors for defect detection and characterization in tube inspection. These probes are presented in chapter 6.

1.4.3 Signal Processing

In eddy current testing, it is essential to minimize the noise which is superimposed to the signal that contains information to interpret correctly the magnetic field perturbation caused by defect presence. For this purpose, two algorithms were implemented to suppress the noise that is superimposed to the signal with information. This work uses sinusoidal excitation with uniform current distribution. Thus, a three-parameter sine-fitting algorithm is used to minimize the effect of quantization error and random noise, compressing the information in amplitude and phase for each point of a scan. The second algorithm is used after a scan to remove lift-off effect, excitation field presence and edge effect. These two algorithms are presented in chapter 5, section 5.4

1.4.4 Defect Reconstruction Algorithm

An inverse problem algorithm was implemented to obtain the eddy current distribution in a metallic plate from the measured magnetic field. The algorithm involves inverse problem regularization applied to image reconstruction technique. The solution found in the inverse problem algorithm to get the eddy current distribution was obtained considering a kernel map that contains the calculated magnetic field in the direction of the sensing axis of the sensor originated by a single dipole with a unit current. This field was computed taking into account the distance between the metallic surface and the plane where the magnetic sensor was positioned. In the inverse problem algorithm, Tikhonov and Total Variation regularizations are used and the two regularized solutions are compared. A proper choice of the regularization parameter value was automatically obtained applying the logarithmic energy derivative method and the L-curve criterion.

1.5 Original Contributions

The thesis presents an algorithm to find the inverse problem solution to obtain the eddy current distribution in non-ferromagnetic and conductive materials from the measured magnetic field. A signal processing algorithm was implemented to improve the information content in the measured magnetic field to minimize the lift-off effect, the edge effect and the superimposed excitation field. Due to the good results obtained with an uniform eddy current probe by Koyama et al. [34], planar probes were designed, built and tested to produce an uniform excitation field in the conductor in order to guarantee a spatially invariant excitation field around the magnetic sensor in use during the scan. The probes combine the uniform field produced by a planar coil with magneto-resistor sensors that have a higher magnetic field sensitivity from Direct Current (DC) to 1 MHz. This kind of planar probes can be easily built in a flex-probe to inspect uneven surfaces, while the lower frequencies required to test the deeper subsurface defects can be provided with the magneto-resistor sensors. Starting with the magnetic field component measured by the magnetic sensor, an inversion algorithm was developed to evaluate the geometry of the cracks. The main result of this inversion algorithm is the determination of the shape of the cracks using the reconstructed eddy current pattern inside the specimen. The results show good characterization of the geometry of cracks that are not parallel to the current flow. These reconstructed patterns give the indication of the orientation and geometry profile of the crack. Several studies were made to improve de characterization of the shape of the cracks. In a initial stage, probe rotation was required to observe the cracks parallel to the current flow. In a second stage, a new probe and excitation method were developed to induce eddy currents with different orientation on the metal surface without rotating the probe during the scan.

1.6 Thesis Structure

The thesis is composed of seven chapters. This chapter contains the introduction, where the motivation, state of the art, objectives and original contributions of this work are included.

In chapter 2, an overview of the fundamental ideas of the eddy current testing method is explained in detail. An historical introduction to the eddy current phenomena is presented focusing mostly on the eddy current testing. The influence of the coil dimension, material property, test frequency, skin effect and crack orientation in eddy current testing is described. Also, an introduction to the remote field eddy current phenomena that occurs in the metallic tube is presented. Finally, the coil design and sensors used in this work are also introduced in this chapter.

Chapter 3 is focused on the simulation work using sinusoidal excitation with uniform current distribution. The obtained simulation results allow to make a careful analysis of the perturbed magnetic field and the eddy current density in the plate when the material under inspection contains a crack. Results are presented in order to study the lift-off effect, the edge effect and the eddy current density in the plate.

In the Chapter 4, the proposed approach to obtain the geometrical characteristics of defects in conductive materials is introduced and explained in detail. The approach was tested in analytical and simulated data and it focuses on the determination of the 2D map of eddy current distribution in the metal around a crack from the 2D map of electromagnetic field component measured with the magnetic sensor by solving the inverse problem. The kernel maps that allow the inversion of data are presented. The direct and inverse problem are described in detail and the regularization methods used in the inverse problem algorithm are compared. Also in this chapter, a study of the evolution of the current density map as a function of the regularization parameter is presented, and a proper choice of the regularization parameter was manually obtained by careful analysis of the eddy current density maps. In the end of this chapter, the reconstruction maps of the eddy current distribution in the plate using the three magnetic field components (B_x , B_y, B_z) are presented. These reconstructed patterns give the indication of the orientation and geometry profile of the crack.

Chapter 5 is focused on the the experimental inspection of defects in aluminium plates using invariant excitation field with sinusoidal excitation. The type of experimental probes used in this work are presented in this chapter. The experimental system used to inspect the metallic plate is explained in detail, and the signal processing techniques developed to improve the measurement data are introduced. Experimental and simulation results are presented in order to study the depth of superficial and sub-surface defects. To obtain the geometric profile of the cracks, the inverse problem algorithm was applied. Regularization methods were applied and a proper choice of the regularization parameter value was automatically obtained. The methods are described in this chapter. According to the shape of a defect, the distribution of eddy current is different and the profile of five different defects were obtained and presented. Several studies were applied in order to improve the defect characterization. The experimental setup and the type of probe were improved and the final prototype is presented in the end of this chapter.

In chapter 6, the experimental work made in the inspection of metallic tubes using the remote field eddy current testing (RFECT) method is described. The fundamental concepts of the RFECT method are presented in order to understand the magnetic field diffusion along a metallic tube. Two probes were designed to compare the detectability of the giant magneto-resistor (GMR) sensor and anisotropic magneto-resistor (AMR) sensor in remote field inspection. The experimental setup used to realize the measurement is described in this chapter.

The last chapter contains the final discussions and conclusions about the developed work.

2

Eddy Current Method

Contents

2.1 Chapter Summary

Fundamental concepts of eddy current method for defect detection in conductive materials are presented in this chapter.The historical evolution of the physical phenomena that originated the appearance of eddy current testing (ECT) to detect cracks in metal is described in section 2.2. An overview of the eddy currents phenomenon and inspection technique in order to understand the essential details of the eddy current method in non-destructive testing (NDT) is presented in the section 2.3. The main idea used to construct a new eddy current probe that combines the technique of alternating current with uniform current distribution in the material and the type of eddy current perturbation produced by the defect in the plate is presented in section 2.4. The eddy current phenomena that occur inside a metal tube are presented in section 2.5. Section 2.6 presents a review of some eddy current probes mentioned in the literature. In the same section, the coil and sensors used in this work are also introduced with more detail.

2.2 History

The history of eddy current testing can be traced back to the discovery of the electromagnetism phenomenon in the beginning of the 19th century. In 1820, Hans Christan Oersted made a surprising observation about the interaction between electricity and magnetism. He noticed a deflected compass needle when an electric current was switched on through a wire. This electrical current had produced a magnetic field strong enough to cause the deflected compass needle. In 1831, knowing the results of Oersted, the english physicist Michael Faraday discovered that a varying magnetic field can induce an electrical current in a conductor. This phenomenon is called electromagnetic induction.

In 1855 the french Jean Bernard Leon Foucault was credited for having discovered the eddy currents. He discovered that the force required for the rotation of a copper disc becomes greater when there is a strong magnetic field involved. He also observed that the disc, at the same time, became heated by the eddy current induced in the metallic surface. However, it was not until 1879 that David Hughes performed the first recorded eddy currents testing. The eddy current testing gained prominence only after World War II. In 1948, Germany Reutlingen Institute developed measuring instruments with the eddy current method. The eddy current method has been used by many authors both theoretically and experimentally. The seminal analytical work of C. V. Dodd and W. E. Deeds calculating analytically the impedance of one coil over a metal stratified material [43] is still used as a reference. Since the eddy current testing exists, this method is used in industrial applications due to its sensitivity to several variations, such as conductivity, permeability, discontinuities, lift-off effect and material thickness. The use of ACFM probes that includes a uniform alternating current in the area on test and detects magnetic field perturbation in that zone was made in the early of 1990.

In the last twenty years, major development have been done in this particular area due to the developments in the electronic field, sensors, instrumentation and good performance computers with excellent tools for modelling.

2.3 Eddy Current Phenomenon

The eddy currents are based on induction of currents in electrically conducting materials. The involved electromagnetic phenomena can be described by the quasi-stationary condition of the Maxwell's equations in a integral form by

$$\mathrm{Maxwell-Faraday}\quad \mathrm{law}: \quad \oint_c \vec{E}\cdot\vec{dl} \;=\; -\frac{\mathrm{d}}{\mathrm{d}t}\iint_{S_c}\vec{B}\cdot\mathrm{d}\vec{S}, \tag{2.1}$$

$$\mathrm{Maxwell-Ampere's}\quad \mathrm{law}: \quad \oint_c \vec{H}\cdot\vec{dl} \;=\; \iint_{S_c}\vec{J}\cdot\mathrm{d}\vec{S}, \tag{2.2}$$

and the constitutive relationships

$$\vec{B} = \mu\vec{H} \quad , \tag{2.3}$$

$$\vec{J} = \sigma\vec{E} \quad , \tag{2.4}$$

where $\vec{E}$ is the electric field, $\vec{H}$ is the magnetic field, $\vec{B}$ is the magnetic flux density, $\vec{J}$ is the current density. In equation 2.2, the displacement current density $(\frac{\partial D}{\partial t})$ has been neglected because the testing regime is in the order of few kHz. So, the displacement current density is much less than the eddy current density in the conductor. The quantities μ, σ are respectively the magnetic permeability and the electric conductivity of a material. According to Maxwell-Faraday equation 2.1, an electric current is induced in a conductor when a time varying magnetic field is applied. This phenomenon is called electromagnetic induction. From equations 2.1 and 2.2, S_c is a surface bounded by the closed path c. In equation 2.1, an electric field $\vec{E}$ exists along c and $\vec{B}$ is the magnetic flux density through the surface S_c taken in the direction compatible with the Stokes rule. In equation 2.2, a magnetic field $\vec{H}$ exists along the closed path c and $\vec{J}$ is the current density that crosses the surface S_c, also according to the Stokes rule.

Figure 2.1 shows the eddy currents phenomenon when an alternating current flows through a coil producing a varying primary magnetic field around it. Placing this excitation coil in the proximity of a metallic surface, electromotive forces are induced in the material and the eddy currents shall take place inside the conductor. If a defect is present in the material, the eddy currents deviate from their normal configuration. This disturbance is manifested by their own magnetic field that can be assessed by a measuring device.

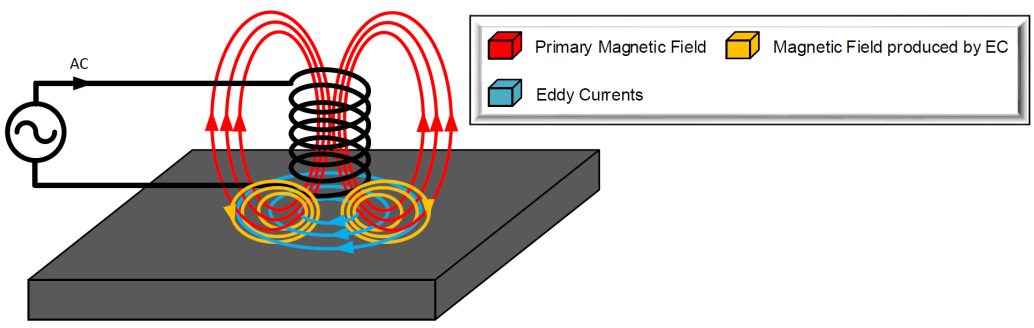

Figure 2.1: Representation of the Eddy Current Phenomenon.

2.3.1 Eddy Current Characteristics

The information of the defect presence in a conductive plate is the most important aspect in defects characterisation. The eddy currents that flow in the metallic structure are sensitive to the following variations:

- Conductivity and permeability of the material;
- Test Frequency;
- Lift-off Effect;
- Edge Effect;
- Defect Orientation;

Each one of them is described in the next subsection.

2.3.1.A Conductivity, Permeability and Test Frequency Influence

In a metallic structure without defect, the distribution of eddy currents in the material is influenced by the material properties, such as electrical conductivity and magnetic permeability. These material properties influences the depth of penetration of the eddy currents in the metallic structure. For lower conductivity or low magnetic permeability of non-ferromagnetic materials, the eddy current achieves deeper penetration. For a given material, the test frequency and the geometric form of the excitation coil determine the depth of penetration of eddy currents in the material. At higher test frequencies, the eddy currents are closer to the material surface. On the other hand, at lower frequencies the penetration of eddy currents is greater. Thus, the selection of the test frequency has to be a compromise that depends on the thickness of the material, desired depth of penetration and degree of sensitivity required.

2.3.1.B Lift-off Effect

One of the problems that affects the obtained results of all kinds of probes is the lift-off effect. This effect occurs when there is a variation in the distance between the probe and the metallic material. The sources of this variation can be caused by the irregular material surfaces or by the probe movement during the tests without keeping a constant distance between the probe and the sample surface. Therefore, the lift-off effect is considered as a source of problem that can affect all kinds of probes and is undesirable in defect detection and defect characterization. To minimize this effect, the distance between the probe and the metallic surface must be as constant as possible during the test. Intending to keep the probe close to the metallic surface, we are dealing with a higher relative variation of the lift-off in the measured data. However, if the distance between the probe and the surface of the specimen increases, the obtained measurement from the probe suffers a signal attenuation that causes the loss of details of the eddy current perturbations.

2.3.1.C Edge Effect

The edge effect occurs when the probe is at the limit of the metallic surface test. This effect is due to a large portion of the eddy currents that cannot flow out of the material boundary. The influence of the edge effect increases as a function of the probe proximity to the edge of the material. Like the lift-off effect, the edge effect is considered a noise source that affects the inspection of metallic materials, when defect detection and defect characterization are required.

2.3.1.D Defect Orientation

The defect position and orientation relative to the distribution of eddy currents are important for defect detection and characterization. Material discontinuities such as a defect oriented perpendicularly to the eddy current lines creates maximum eddy current perturbations and allows maximum defect information. On the other way, the eddy current perturbations caused by discontinuities oriented parallel to the current lines are minimal and the defect detection is limited. In that condition, the smaller the size of the defect, the more undetectable it is. For this case, a scanned area is required moving the probe with hight resolution for defect detection. Figure 2.2 illustrates the two cases described above.

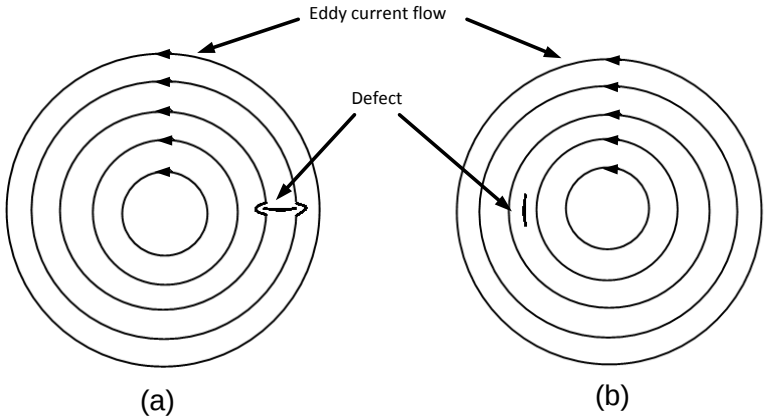

Figure 2.2: Representation of the eddy current flow in the presence of a defect. (a) Defect orientation perpendicular to the current lines. (b) Defect orientation parallel to the current lines.

2.3.2 Standard Depth of Penetration - Skin Effect

The flow of eddy currents in a metal is maximum at the material surface and it is attenuated with increasing depth. Considering a sinusoidal current with a angular frequency equal to ω (rad/s) in a homogeneous metal with an electrical conductivity σ (S/m) and magnetic permeability μ (H/m), a surface current density in the metal with uniform distribution along the x-axis ($J_x = J_o$) and only changes along depth z (m), the current density is described by

$$J(z,t) = J_x(z,t)\,\overrightarrow{u_x} = J_o e^{-\frac{z}{\delta}} \cos\left(\omega t - \frac{z}{\delta}\right) \quad [Am^{-2}] \quad \text{with} \quad \delta = \sqrt{\frac{2}{\omega\mu\sigma}} \quad [m] \quad , \tag{2.5}$$

where δ is the standard depth of penetration SDP.

In the complex form, the current density may be expressed as

$$J(z) = J_o e^{-\frac{z}{\delta}} e^{-j\frac{z}{\delta}} \quad . \tag{2.6}$$

From equation 2.6, it is possible to conclude that the amplitude of the current density diminishes exponentially along the depth z and the phase of the current density along the depth z is delayed with respect to the current density at the boundary surface by a angle of $\frac{z}{\delta}$ (in radian units). For one depth δ, the amplitude of the eddy current density is $\frac{1}{e}$ of its surface density and the phase delay of the eddy current is 1 rad. The skin effect phenomenon for the amplitude current density along depth z is represented in Figure 2.3.

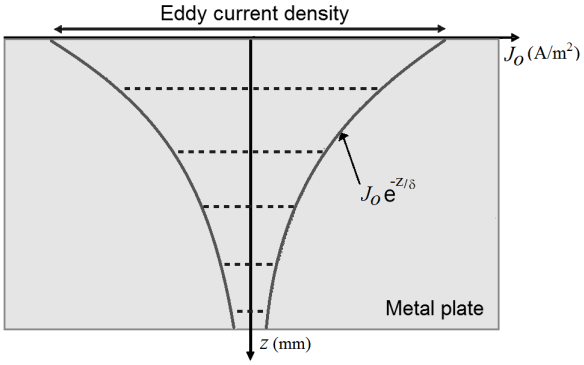

Figure 2.3: Penetration Depth of eddy currents in a metallic plate.

From equation 2.5, it possible to say that the flow of eddy currents in the volume of the metal plate depends on the frequency f of the sinusoidal current imposed on the excitation coil. For a given material, the only way to control the eddy currents penetration is by varying the test frequency. As an example, considering a imposed sinusoidal field such that the current density at the surface is $J_o = 1A/m^2$ on a ten mm thickness aluminium plate with permeability $\mu = \mu_0 = 4\pi \times 10^{-7} H/m$ and conductivity $\sigma = 3.57 \times 10^7 S/m$, Figure 2.4 shows the exponential decay of the current density inside the metal for two different frequencies (500 Hz and 5 kHz), where the solid line corresponds to the lower frequency test and dashed line corresponds to the higher frequency test.

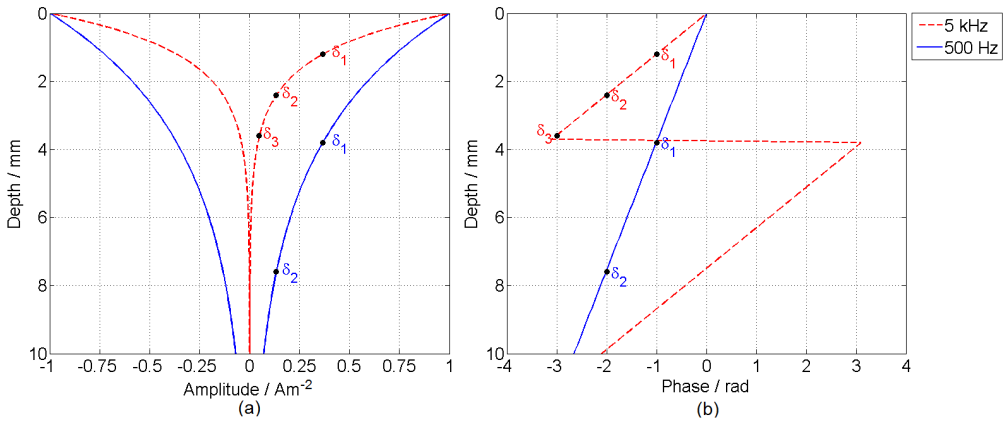

Figure 2.4: Representation of the current density in an aluminium plate at frequencies of 500 Hz and 5 kHz: (a) Exponential decay of the amplitude of the current density ($e^{-z/\delta}$); (b) Linear decay of the phase of the current density $J(z)$ between $\pm\pi$.

It is possible to say that lower test frequencies should be used for greater material thicknesses to examine subsurface characteristics, as defects. In the other way, higher test frequencies should be chosen to examine surface defects. For different materials, the standard depth of penetration (SDP) changes as a function of the conductivity and permeability. Starting with equation 2.5, Figure 2.5 shows the SDP as a function of frequency for the materials used in our laboratory.

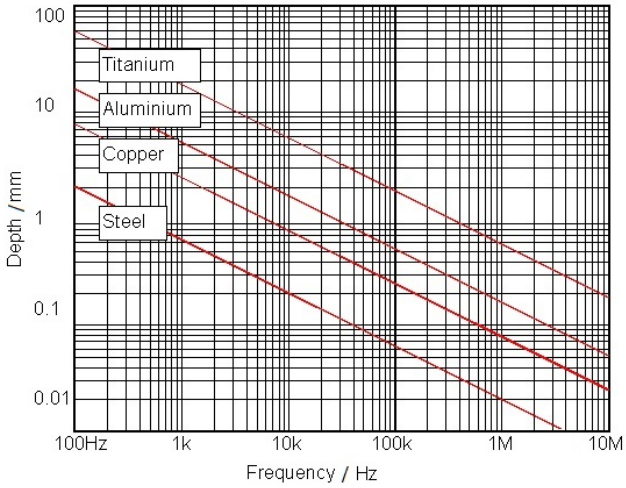

Figure 2.5: Penetration depth of eddy currents in different materials as a function of frequency.

2.4 Alternating Current with Uniform Current Distribution

Alternating current with uniform current distribution is a technique for NDT derived from the methods used in Eddy Current Testing (ECT). The considerations and phenomena described above in this chapter are available for this technique. As previously mentioned in the above sections, an excitation coil is required to induce eddy currents in the metallic plate under test and a magnetic field detector is used to measure the magnetic field at the zone of highest concentration of induced eddy currents. The main difference between this method and the traditional eddy current testing method is that, in this method, the eddy currents generated inside the metal by induction will be spatially uniform inside the restricted area under the magnetic sensor. This means that when the metal surface is scanned by the probe, the excitation field in the region of the scan remains an invariant. In a situation without defects, the induction currents follow parallel lines oriented in the same direction of the excitation, but with a phase whose difference to opposition depends on the material conductivity.

In the presence of a defect in that zone, the uniform eddy current lines are forced to deviate from the defect. Figure 2.6 depicts the situation characterized above.

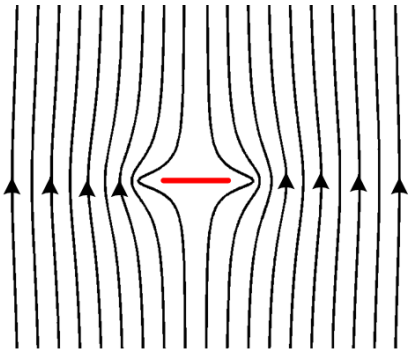

Figure 2.6: Representation of the uniform eddy current flow in the metallic plate with defect presence.

The use of this technique that forces an alternating current with uniform distribution in the material makes the current flow more predictable, simplifying the interpretation of the magnetic field perturbation when defects are present in the metal. This method can help to estimate the size and length of a crack. However, the presence of a defect oriented parallel to the current flow is harder to detect with this technique, making impossible to detect smaller defects parallel to the current flow, as illustrated in Figure 2.7.

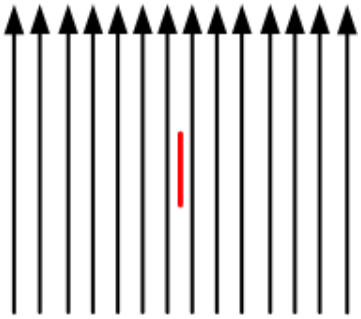

Figure 2.7: Representation of the eddy currents flow with defect parallel to the current flow.

Hence, using this technique, the metal under test should be analysed with uniform alternating current under several current flow orientations when the defect orientation is unknown.

2.5 Remote Field Eddy Current Phenomenon

The Remote Field Eddy Current Testing (RFECT) is a method that can be applied with eddy currents in order to find cracks in pipelines and tubes [44]. In theory, the remote field testing is based on the through-wall indirect coupling that allows the diffusion of the field both inside and outside the tube [45, 46]. This diffusion reduces the attenuation of the magnetic field along the tube making it an attractive NDT method for the analysis of several defects. A remote field testing probe is moved inside the tube wall to detect internal and external discontinuities with approximately equal sensitivity.

In Figure 2.8, it is represented the three operating zones that exist when the remote field testing method is applied.

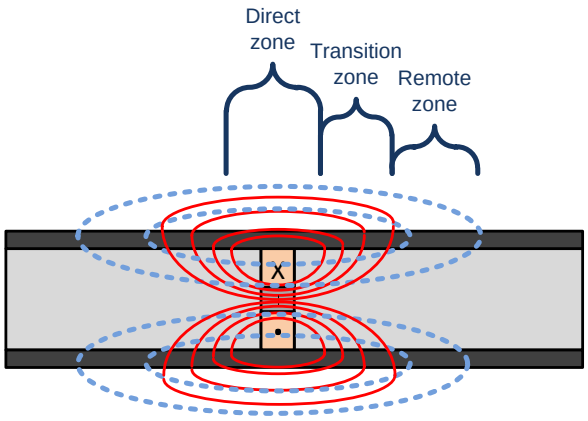

Figure 2.8: Representation of the several operating zones in RFECT .

The direct zone has an intense varying magnetic field from the excitation coil which doesn't allow the detection of the defect. The transition zone is where the excitation field is replaced by the field produced by the eddy currents, which is in phase opposition with the excitation, resulting in minimum magnetic field amplitude in this zone. The remote zone is the region where the sensed magnetic field is only produced by the eddy currents. Hence, this is the best zone to place a magnetic sensor. The distance between the excitation coil and the magnetic field sensor is fixed while they are moved inside the tube wall to detect defects.

2.6 Eddy Current Probe

As mentioned previously in section 1.2 (State of The Art), several types of ECP are used to evaluate metallic materials and each one is adapted to its purpose. However, all them are similar in one point: an excitation coil and a magnetic sensor are required to be used in ECT. Usually, a vertical axis coil is used as excitation solution to induce eddy currents in the conductor. To sense the eddy current perturbation in a material with defects, the magnetic field perturbation caused by one defect is acquired and the information is analysed by the magnetic sensor. The magnetic sensors most mentioned in the literature are the sensing coils, flux-gates, Superconducting Quantum Interference Devices (SQUID)s, Hall sensors and magnetoresistive sensors.

In this work, a planar coil with uniform distribution was developed to guarantee an uniform alternating magnetic field around the zone on test. As magnetic sensor, magnetoresistive sensors are used because of their high sensitivity to the magnetic field perturbation in a very large frequency range (DC - 1 MHz). The uniform current distribution and magnetoresitive sensors characteristics used in this work are detailed in subsection 2.4 and subsection 2.6.2, respectively.

2.6.1 Coil Design

The coil design was based on the eddy current testing with uniform alternating current distribution. The geometry of the coil is represented in Figure 2.9. The black arrows represents the current flow in the coil and the white zone represents the uniform current zone where the magnetic sensor should be placed.

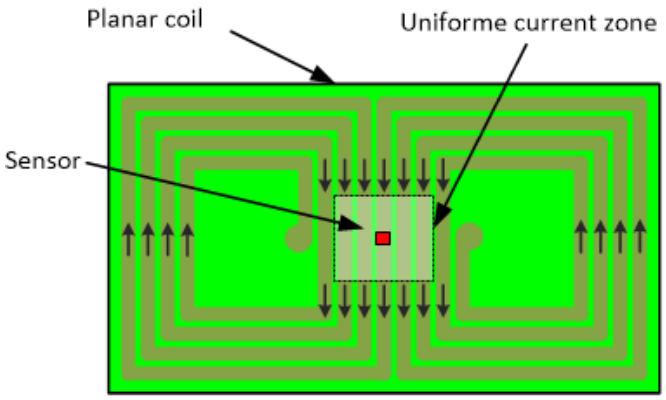

Figure 2.9: Representation of the planar coil design used into the probe.

2.6.2 Magnetoresistive Sensors

There are several magnetic sensors capable of determining values of magnetic flux density. As mentioned previously in section 2.6, the high sensitivity provided by the magnetoresistive sensors along their wide frequency bandwidth make them good candidates in the application of defect detection. The high sensitivity in a low frequency operation allow a greater penetration of the eddy currents in the material thickness on test helping to examine subsurface defect characteristics when the metal is thick. This phenomenon was already explain in 2.3.2.

2.6.2.A Anisotropic Magnetoresitors

Anisotropic Magnetoresitors are devices based on the variation of the electrical resistance due to the presence of a magnetic field. The AMR effect occurs in ferromagnetic materials. The sensor is termed anisotropic because it depends on the angle θ between the electric current and the magnetization direction. The resistance of the AMR is given by

$$R = R_0 + \triangle R \cos^2 \theta \quad [\Omega] \quad , \tag{2.7}$$

Figure 2.10 the equation above in function of θ. It possible to see that the resistance is maximum at 0 or 180 degrees, and minimum at 90 degrees. The optimum operating point is at 45 degrees that corresponds to the point with maximum sensitivity and linearity.

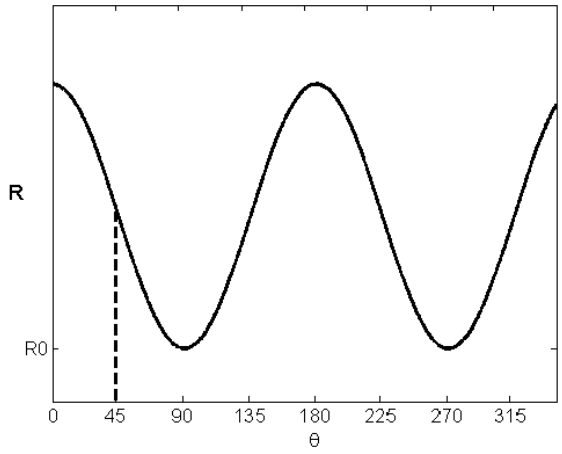

Figure 2.10: The variation of △R as a function of angle between the current and the magnetization.

The best use of AMR elements for magnetic field sensors is with a Wheatstone bridge configurations as depicted in Figure 2.11. The resistance R of all four AMR elements is the same. The bridge is supplied between Vcc to Gnd, causing current to flow through the resistors. A crossed applied field H causes the magnetization in two of the oppositely placed resistors to rotate towards the current, resulting in an increase in the resistance R. In the remaining two oppositely-placed resistors magnetization rotates away from the current resulting in a decrease in the resistance R. The voltage output sensor is proportional to a applied external magnetic field. The HMC10xx family of sensors from Honeywell's utilize Anisotropic Magnetoresistive technology that provides a high sensitivity of 120 μG to 6 G with wide frequency response (DC to 1 MHz). However, they have a limited magnetic field range meaning that their saturation field is quite low. A set/reset drive circuit providing pulses of electrical current is needed to force the sensor to operate in the high sensitivity mode. In the last decades various solid state magnetic sensors have been created with one, two and three axis to allow the measurement of magnetic fields in several directions.

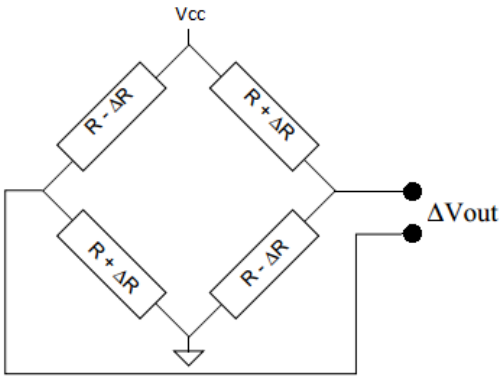

Figure 2.11: Wheatstone bridge configuration of an AMR sensor produced by Honeywell's.

2.6.2.B Giant Magnetoresistors

Giant magnetoresistors are devices based on the giant magnetoresistivity phenomenon. This phenomenon is also based on the variation of electrical resistance due to the presence of a magnetic field. It consists of several layers of ferromagnetic metal separated by non-magnetic metal layers as spacers. To obtain the GMR effect, the ferromagnetic layers must be placed in opposite polarizations to block the passage of electrons from the adjacent layers. In the presence of an external magnetic field, the magnetic layers are aligned in the same direction that allow an easier passage of electrons through the ferromagnetic layers and change the electrical resistance of the GMR. In Figure 2.12 the phenomenon is shown.

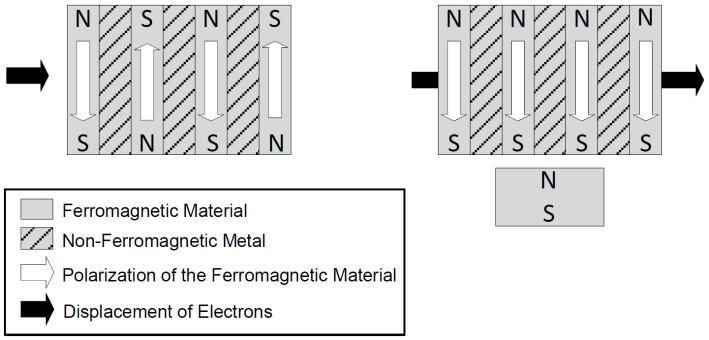

Figure 2.12: Illustration of the giant magnetoresistivity phenomenon.

The commercial GMR packages type A002-02 from Non-Volatile Electronics (NVE) were used in this work. These packages include four giant magnetoresistances configured in a Wheatstone bridge, where two of them are sensing elements and the other two are shielded. Figure 2.13 (a) depicts the internal configuration of the giant magneto-resistors sensor AA002-02. A +/-12 V power supply was used to power the GMR sensor (Wheatstone bridge).

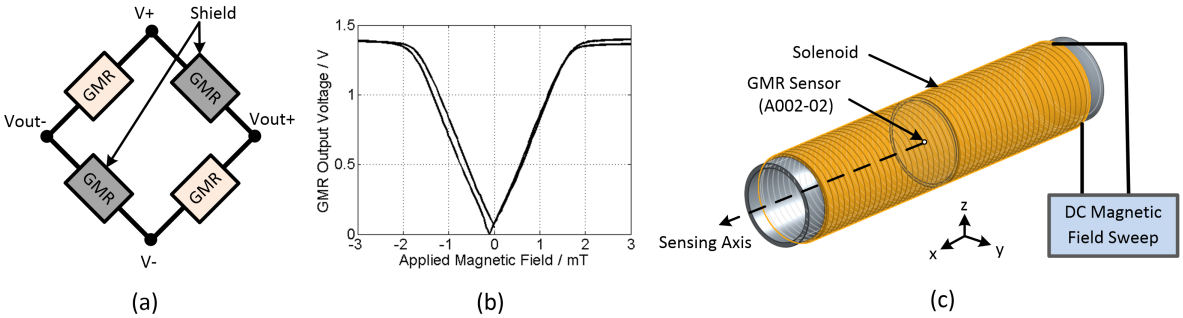

Figure 2.13: Magnetic Sensor Characterization: (a) Wheatstone bridge configuration of a typical GMR sensor; (b) Magnetic characteristic profile of the GMR sensor AA002-02 when it is driven by 12 V; (c) Experimental Setup used to obtain the magnetic sensor characteristic profile.

The presence of an external magnetic field in the vicinity of the GMR sensor package causes the sensing elements to change their resistances while the reference resistors remain unchanged, resulting in a voltage difference in the bridge output. The differential voltage output changes when the sensor crosses over a defect due to the variations of the external magnetic field produced by the eddy currents. When the two unshielded GMRs are equidistant from the center of a crack, the differential

output voltage is zero. The characteristic profile of the A002-02 sensor is depicted in Figure 2.13 (b) and it was obtained experimentally by using a solenoid to apply an uniform magnetic field that is parallel to the sensing axis of the GMR package. The sensor was carefully positioned in the center of the solenoid, as depicted in Fig. 2.13 (c). A sweep in the DC magnetic field was applied to obtain the characteristic profile of the sensor. The solenoid has 3 layers of copper wire with 370 turns in each layer, a radius of 1.25 cm, and length (*l*) of 12.5 cm. As the solenoid length is much longer than its radius, the following equation 2.8 was employed in order to calculate the applied magnetic field *B*.

$$B = \frac{\mu_0 N I}{l} \quad , \tag{2.8}$$

Figure 2.13 (b) shows that the GMR output is not linear along the complete range of magnetic field sweep applied, but it is quite linear if only the ascending (or descending) branch is considered. Thus, it is necessary to bias the magnetic sensor to the linear zone of the characteristic curve to obtain a linear behaviour. In this work, this is achieved by placing a small permanent magnet in the vicinity of the sensor.

3

FEM Simulations Using Uniform Alternating Current in Plate Inspection

Contents

3.1 Chapter Summary

To investigate the magnetic field response to defect presence using uniform alternating current, simulations were performed on an Intel® Quad Core PC with 16GB RAM using Finite Element Method (FEM). In this section, the simulations were performed using FLUX and COMSOL Multi-physics [47] software. The modelling works investigate the lift-off effect, the edge effect, the current density, the depth of penetration and the magnetic field perturbation around defects in aluminium plates using a spatially invariant excitation field. For several linear defect dimensions, results of eddy current densities in a conductor plate were obtained by FLUX software and they are presented in section 3.2. A study of the lift-off effect and the edge effect were made and presented in section 3.3 and section 3.4, respectively. Other simulations will be presented in chapter 4 and in chapter 5 as complementary results to experimental inspection.

3.2 Magnetic Field Response to Defect Dimension Changes

In this section, a study concerning the perturbation of the magnetic field and eddy currents when the defect dimension changes were made, in order to extract relevant information that allows the determination of the defect characteristics. Numerical simulations based on a commercial finite element model (FLUX) were carried out.

3.2.1 Simulation Model

Figure 3.1 depicts the modelling work investigated in this subsection. An aluminium plate with 4 mm of thickness and an area equal to (80×80) mm^2 was used as sample test. The used electromagnetic proprieties of the sample were σ=50 MS/m and μ_r=1.

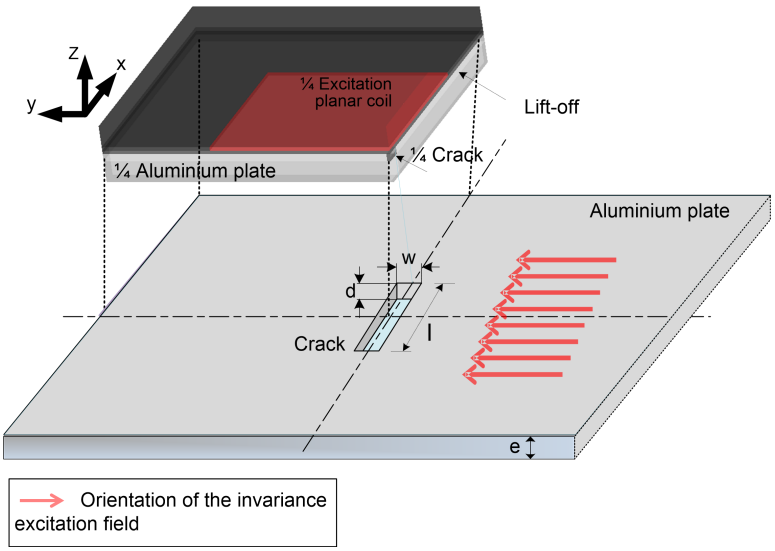

Figure 3.1: Representation of the sample plate under test, the linear defect dimensions, and the symmetries made in the simulations.

The simulations were made for linear defects with a rectangular shape of width (w) equal to 1 mm, different lengths (l) from 2 mm to 12 mm and depths (d) that vary from 1 mm to 3 mm. The excitation coil above the plate includes 25 parallel wires having a 50 mm $\times$ 50 mm shape and produces a invariant excitation field that induced a linearly distributed eddy current pattern in the plate when there are no defects at the plate. The simulations were carried out for an excitation current of 1 A and with an operating frequency of 5000 Hz. Two symmetry planes were used to decrease the volume to be discretized. In the xz plane the symmetry was defined as tangent magnetic field and yz plane the magnetic field was defined as normal.

3.2.2 Results and Discussion about Defect Dimensions

To predict and evaluate the magnetic field perturbation in a conductor plate with different defects, some simulations were performed and the magnetic field components (B_x and B_y) obtained for a linear defect 2 mm deep and 12 mm long are presented in Figure 3.2. The B_x map is the magnetic field at points (x,y) along the x direction, while the B_y map is the magnetic field at points (x,y) along the y direction. The perturbations of the secondary magnetic field along the x direction are mainly related with the induced eddy currents in the yz plane, which appear when, in the presence of a discontinuity, they have to pass beneath or parallel the crack. The perturbations of the secondary magnetic field along the y direction comes from the induced eddy currents in the xz plane, which appear when, in the presence of a discontinuity, they have to pass beneath or perpendicularly the crack. It can be observed in Figure 3.2 that the estimation of the length can be approximately made by the obtained magnetic field perturbation. A dotted line representing the defect is drawn on the image for clarity purposes. Probably, B_x that has only one peak is easier to interpret. But both components of magnetic field allow defect length and position estimation.

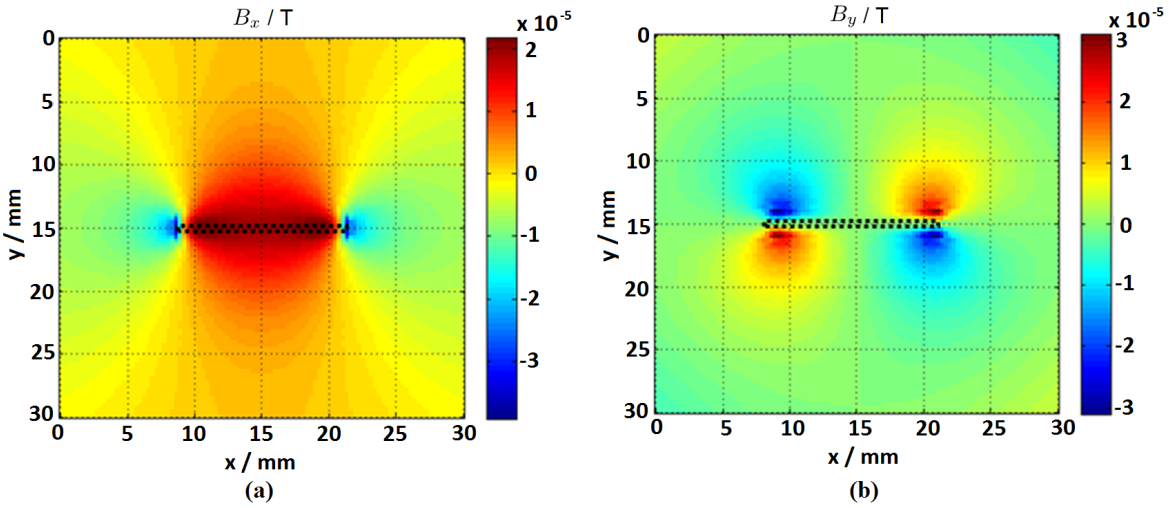

Figure 3.2: Simulated magnetic field perturbations for a 12 mm long defect and 2 mm deep: (a) x component of the magnetic field (B_x) ; (b) y component of the magnetic field (B_y).

To estimate and evaluate the defect depth from the measured magnetic fields is harder than the defect length estimation. In the next results, the eddy current density in the material is presented

with gray scale, where the black color zones correspond to no current density and the white color zones corresponds to the maximum current density. Comparing the eddy current densities depicted in Figure 3.3 and Figure 3.4 obtained for long defects of 2 mm and 12 mm of length, respectively, having three different depths (d = 1, 2 and 3 mm). The results show that the intensity of currents that cross underneath the defect depends on the length/depth ratio of the defect.

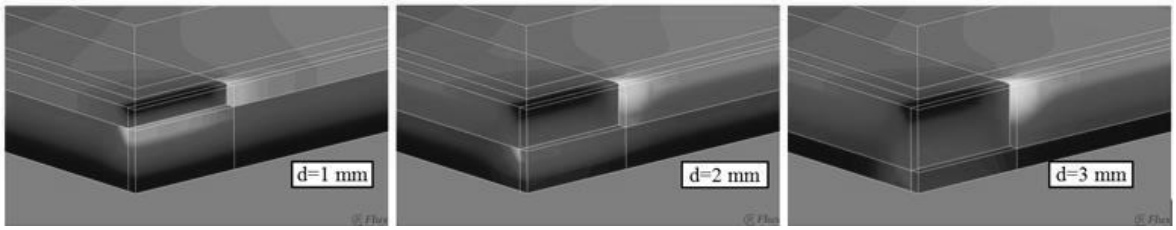

Figure 3.3: Simulated eddy current density for a 12 mm long defect at three different depths (d=1, 2 and 3 mm).

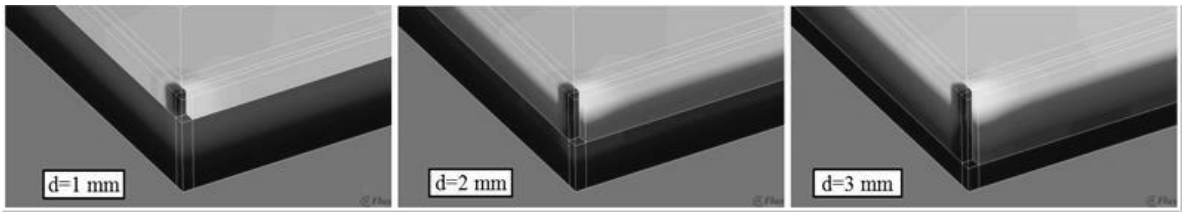

Figure 3.4: Simulated eddy current density for a 2 mm long defect at three different depths (d= 1, 2 and 3 mm).

In order to clarify the understanding of this effect, defects were classified in two types: long defects, with length much bigger than depth and short defects with length shorter than depth. Figure 3.3 shows that for a long defect some current will pass underneath the defect to short the current's path, whereas Figure 3.4 shows that for a short defect most current will go around it, rather than beneath it. Taking this into account, it is expected that the magnetic field measured right above the defect will change less with the depth, when compared to long defects. In fact, after a certain depth, when all the currents are going around the defect and none is crossing beneath it, there will be no change to the paths of any currents, hence no change will happen to the magnetic fields as well. This effect can be also observed in the eddy current densities obtained for a constant depth of defect (d=2.5 mm) as depicted in Figure 3.5, and with three different lengths (l=1, 3 and 10 mm).

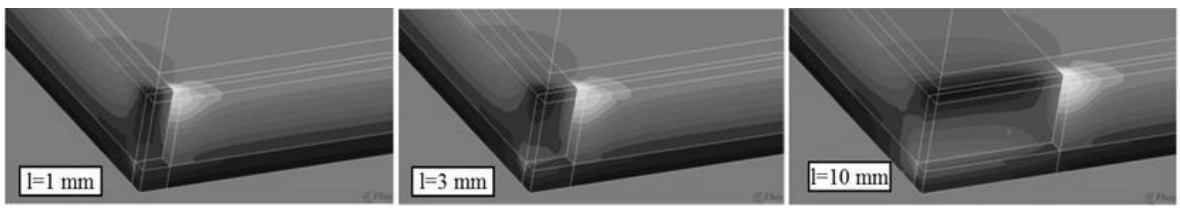

Figure 3.5: Simulated eddy current density for a 2.5 mm deep defect at three different length (l = 1, 3 and 10 mm).

Note that the simulations were performed for a test frequency of 5000 Hz, which corresponds to a standard penetration depth (δ) equal to 1 mm. Nevertheless, as depicted in Figure 3.3, the eddy currents penetrate into the material more than δ. For test frequency much higher than 5000 Hz,

the standard penetration depth (δ) decreases and the intensity of currents that cross underneath the defect (l=12 mm at d=1 mm) also decreases.

3.3 Magnetic Field Response to Defect when Lift-off Changes

To investigate the lift-off effect using eddy current technique with an invariant excitation field, some simulations were performed using COMSOL Multiphysics and presented in the next subsections.

3.3.1 Simulation Model

Figure 3.6 depicts the modelling work used to evaluate the magnetic field response to defect when lift-off changes. In this modelling work, the lift-off effect was investigated in an aluminium plate with a linear defect with 2 mm of depth and 10 mm long. The end and center of the defect were analysed in points along four straight lines (with 0.5 mm of step between each point). These straight lines positions were chosen to be in the region were maximum amplitude of the magnetic field perturbation were obtained in the presence of a linear defect, as already shown in Figure 3.2.

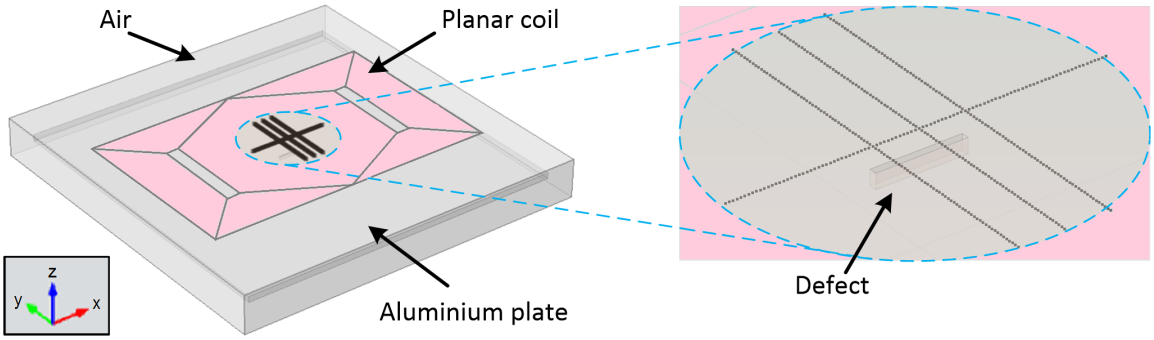

Figure 3.6: Modelling work used to investigate the lift-off effect.

A xz cross section view of Figure 3.6 at the defect position is depicted in Figure 3.7. For each test, the distance between the probe (planar coil with measuring points) and the surface of the aluminium plate was modified. Simulated magnetic fields B_x and B_y were computed for 10 different lift-off probe positions between 0.5 mm to 5 mm with steps of 0.5 mm. The excitation coil and the computed points were moved for each lift-off situation. Details of the model setup are presented in Table 3.1.

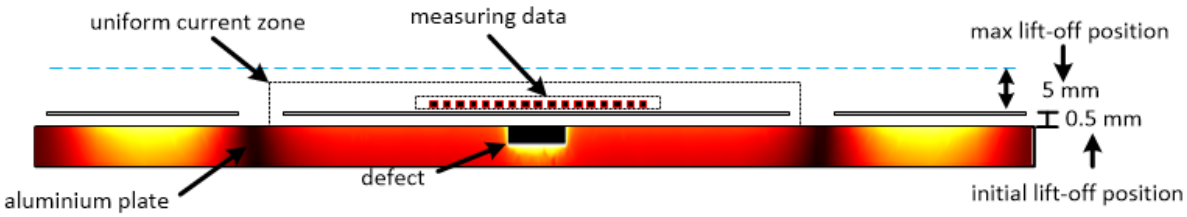

Figure 3.7: xz Cross section view of Figure 3.6 at the defect position.

Table 3.1: Simulation model details to investigate the lift-off effect.

Aluminium Plate	
Size (mm)	$210 \times 210 \times 4$
Conductivity (MS/m)	35.59
Planar Coil	
Excitation Current (A)	1
Coil Turns in the Invariant Excitation Field Zone	50
Scan	
Scan Step Size (mm)	0.5

3.3.2 Results and Discussions about Lift-off Effect

To evaluate the lift-off effect, tests were performed applying an excitation frequency of 420 Hz that corresponds to 4 mm standard depth of penetration (δ) in an aluminium plate. The B_x component of the magnetic field perturbation along x direction and across y direction of the defect at the center position are depicted in Figures 3.8 and 3.9. The B_x component was divided in two parts, where Figure 3.8 (a) correspond to the constant amplitude value of the signal at each lift-off value and Figure 3.8 (b) correspond to the amplitude signal of the magnetic field perturbation. In Figure 3.8 (a), it possible to observe that the constant amplitude value of the magnetic field component (B_x) increases when the lift-off value also increases. This is due to the lower amplitude of the eddy current induced in the plate when the distance between plate and probe increases, making the excitation field increasingly dominant in the field measurement.

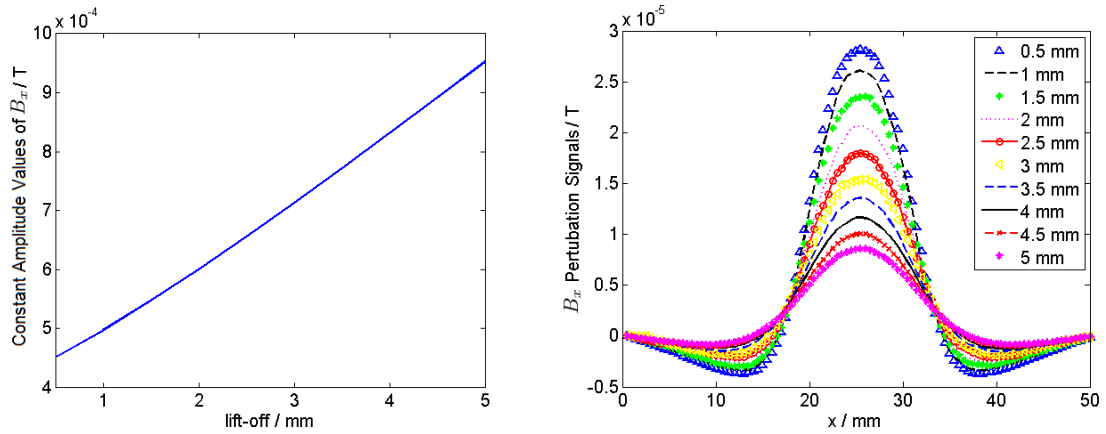

(a) **(b)**

Figure 3.8: Simulated magnetic field response B_x to different lift-off probe to a straight line obtained crossing the center of the defect along x axis: (a) Constant amplitude values of B_x component; (b) Defect perturbation change of B_x component due to lift-off effect.

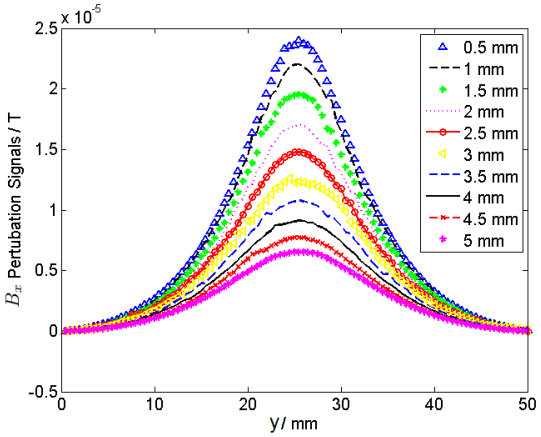

Figure 3.9: Simulated magnetic field response of B_x component to different lift-off probe to a straight line obtained crossing the center of the defect along y axis.

The results show that when the lift-off changes, the amplitude values of the signals also changes. Hence, it is possible to say that a constant lift-off distance should be guaranteed between the probe and the sample on test to have constant field measurement about the defect perturbation signal. The use of planar coils in quasi-contact with surface on test can be a solution to minimize lift-off effect. Otherwise, the lift-off effect has to be taken into account to obtain defect dimensions. In that case, a lift-off probe calibration can be used before test purpose to store information of lift-off effect in a know type and size of material without defect, in order to be used in post-processing signal. Figure 3.10 depicts the B_y component of the magnetic field response in the straight lines over the edge of the defect for the different lift-off probe. The results also show clearly the changes of the magnetic field response due to lift-off effect. In that case, the magnetic field component B_y is perpendicular to the excitation magnetic field with null magnetic field responses for any lift-off probe when no defect is detected.

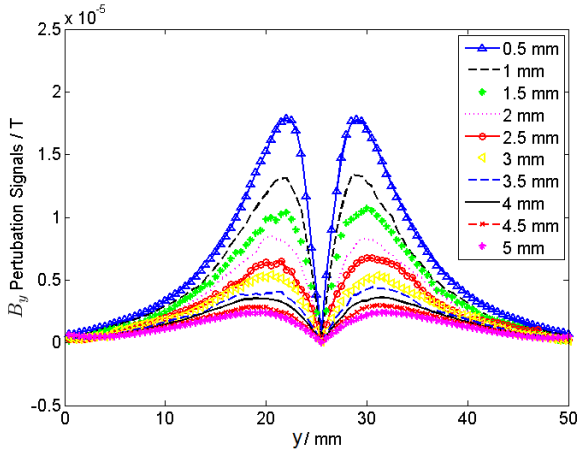

Figure 3.10: Simulated magnetic field response B_y to different lift-off probe to a straight line obtained crossing the edge of the defect.

3.4 Magnetic Field Response in the Proximity of the Plate Edges

To study the edge effect using a planar coil with an invariance excitation field zone, some simulations were performed using COMSOL Multiphysics and presented in this subsection. These simulations were made in an aluminium plate without defect. The planar coil design is similar to the previous simulation presented in 3.3.1.

3.4.1 Simulation Model

Figure 3.11 depicts the modelling work to predict the magnetic field response in the proximity of the plate border. The simulation was made by moving a planar coil over the plate along the x axis as illustrated in Figure 3.11 (b) with a dashed line. Details of the model setup are presented in Table 3.2.

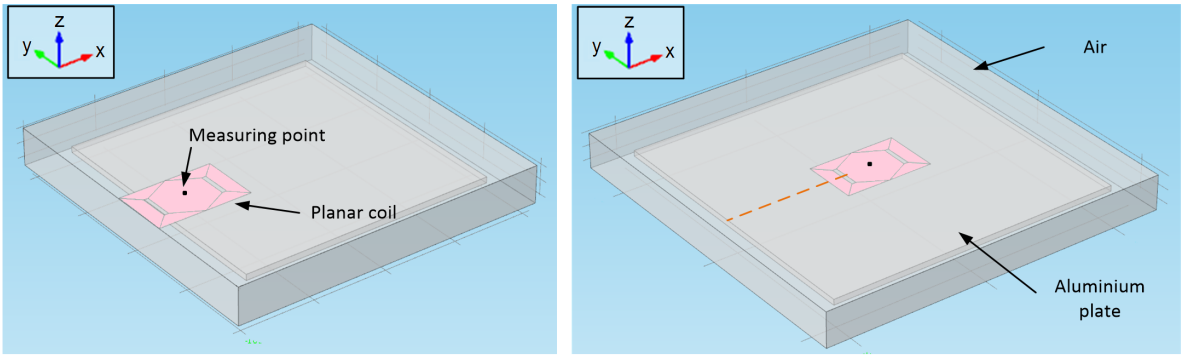

Figure 3.11: Modelling work used to investigate the edge effect. (a) Started point of the simulation; (b) Ended point of the simulation.

Table 3.2: Simulation model detail to investigate edge effect.

Aluminium Plate	
Size (mm)	$170 \times 170 \times 4$
Conductivity (MS/m)	35.59
Planar Coil	
Excitation Current (A)	1
Coil Turns in the Invariant Excitation Field Zone	50
Length of the Invariant Excitation Field Zone (mm)	40
Scan	
Scan Step Size (mm)	1
Number of Points Obtained	65

Figure 3.12 depicts the top view of the eddy current distribution induced in the aluminium plate.

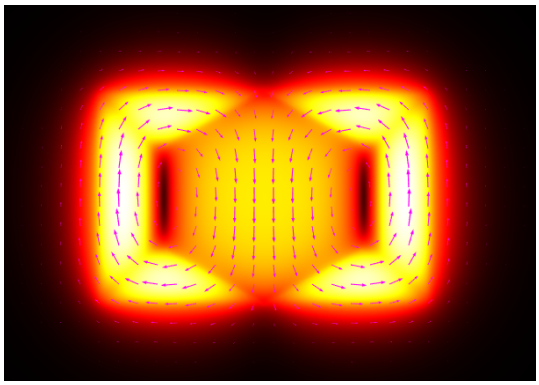

Figure 3.12: Simulated eddy current distribution in the aluminium plate for a planar coil designed to produce invariant excitation field in the measuring zone.

3.4.2 Results and Discussions about Edge Effect

The magnetic field response B_x along the scan line was examined applying several chosen excitation frequencies according to the standard depth of penetration. The used frequencies are 269 kHz; 6.720 kHz; 2.989 kHz; 1.681 kHz; 1.076 kHz; 747 Hz; 549 Hz and 420 Hz that corresponds to 0.5 mm to 4 mm standard depth of penetration with step of 0.5 mm, respectively. Figure 3.13 depicts the field component B_x for the several applied excitation frequencies and a line was added to the figures to mark the first moment that the coil is completely in the surface of the aluminium plate.

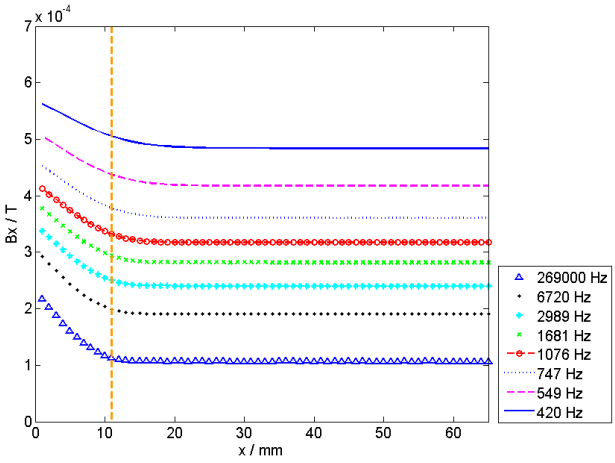

Figure 3.13: The obtained magnetic field component B_x along the scanned line.

Observing Figure 3.13, the results for B_x show that the influence of the edge proximity using an invariant excitation field depends on the excitation frequency used to scan the conductor material under test. As observed, the lower the excitation frequencies, the larger the distance between the coil and the plate edge is needed. Otherwise, signal corrections are required to fit the edge effect. Measuring the B_y component, the obtained magnetic field is approximately zero along the scanned line. This is due to the geometry of the coil that produce only B_x component of excitation field in the region of measuring point. Thus, it is impossible to observe edge effect measuring B_y.

4

ECT Using Image Processing Technique

Contents

4.1 Chapter Summary

This chapter presents an inverse problem solution in order to obtain the geometrical characteristics of defects by the determination of the spatial distribution of eddy current around a defect in a metallic plate. Section 4.2 presents the characteristics of the problem involved to make a geometric profile of the defect. The direct problem is presented in section 4.3, while the inverse problem is presented in section 4.4. An example of a linear defect of length 20 mm is presented. The eddy current distribution is obtained by an analytical conformal transformation when uniform current distribution is imposed at the surface, around the defect. In the inversion problem method, Tikhonov and Total Variation regularizations are used. Simulations were performed to verify the results.

4.2 Introduction to the Proposed Approach in ECT

In the past few years, important advances in the practice of inverse problems have been developed. In ECT, the current work on defect reconstruction uses inverse modelling where the reconstruction is performed using iterative machine learning methods such as neural networks. In this work, an original inverse solution is presented to characterize defects in metallic structures, where a relationship between the eddy currents and the magnetic fields is used to map the profile of a defect. By analysing the problem, it is possible to say that it is a well-posed problem because the solution exists, is unique and the inverse mapping is continuous. The problem is non-linear because the sum of the measurements obtained for two defects inspected separately is different from two close defects inspected together. However, the relation between the eddy currents and the magnetic fields produced by them is linear. Inducing eddy currents with uniform distribution in a metal at the location of a defect, the eddy current uniformity is perturbed and these perturbation patterns are taken into account in the inversion problem solution presented in this work. Figure 4.1 shows an example of eddy current lines in a metal plate when a defect is present in the uniform current zone. The total current lines on the plate with a crack are depicted in Figure 4.1 (a). These eddy currents lines can be decomposed into a component with uniform density presented in Figure 4.1 (b) and a perturbation component presented in Figure 4.1 (c).

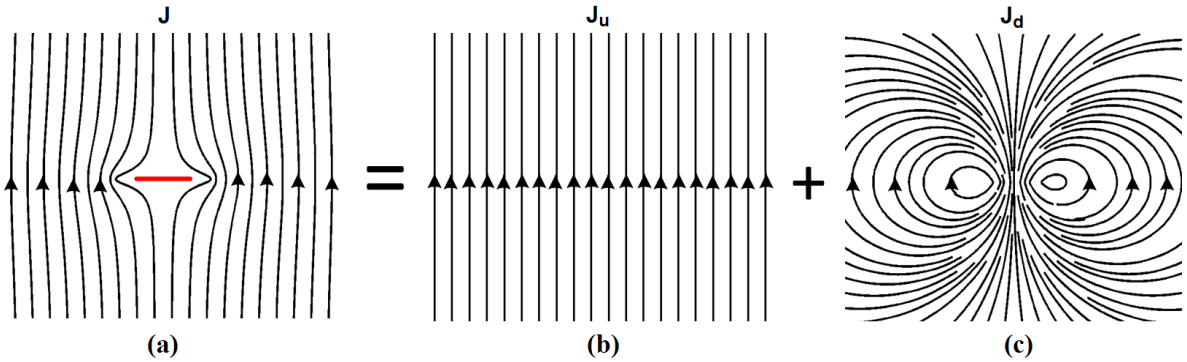

Figure 4.1: Representation of the eddy current lines on a plate with defect: (a) Total currents lines J; (b) Uniform current lines J_u; (c) Perturbed current lines J_d.

The perturbation component can be represented as a dipole current density [48–50] whose representation in a discretized space must be obtained. Assuming this distribution for the current perturbations, the kernel map b (in equation 4.1) can be represented as the magnetic field that should be sensed at (m,n) point when a unit dipole current is positioned at (i,j). This field can easily be computed taking to account the specific form of the unit current dipole that is being considered and the distance between the sensing point of the sensor and the plate surface. Hence, the measured field component B may be represented as

$$B(m,n) = \sum_{i,j} b(m-i, n-j) \times J_d(i,j) \quad , \tag{4.1}$$

where B is a map with the perturbation of magnetic field sensed by the GMR sensing axis for any single component, J_d is a matrix with the perturbation current dipoles induced in the plate, and b is the kernel matrix that maps J_d into B. In order to reconstruct the distribution of the total current lines into the plate, the sum of a current component that is spatially uniform along the axis of excitation has to be made as illustrated in the previous Figure 4.1.

The space discretization of the perturbation was decomposed into square loops with edges equal to the position step between each measurement taken Δ and is represented in Figure 4.2.

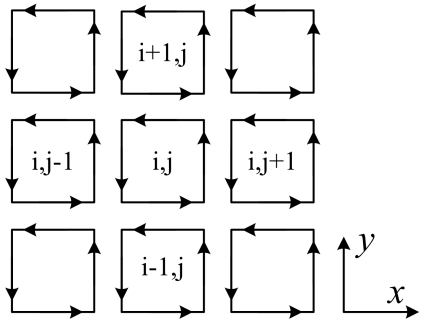

Figure 4.2: Discretization of the perturbation current into square loops.

The current perturbation in the metallic plate was determined in terms of a superposition of dipolar currents circulating in square loops and the current density which results on each element was calculated by:

$$\begin{aligned} J_x(i,j) &= \frac{(J_d(i+1,j)-J_d(i,j))+(J_d(i,j)-J_d(i-1,j))}{2\Delta y} = \frac{J_d(i+1,j)-J_d(i-1,j))}{2\Delta y} \\ J_y(i,j) &= \frac{(J_d(i,j-1)-J_d(i,j))+(J_d(i,j)-J_d(i,j+1))}{2\Delta x} = \frac{J_d(i,j+1)-J_d(i,j-1))}{2\Delta x} \end{aligned} \tag{4.2}$$

To obtain the reconstruction of the total currents, a spatially uniform current along the axis of excitation must be summed with a constant amplitude which is chosen in order that the total current density at the metallic surface is non-negative. This operation must be considered as the reverse of what was depicted in Figure 4.1.

To finish and clarify the chosen solution, a total current density map in the plate will be estimated from a magnetic field map containing the perturbation originated by the deviation of the eddy currents

in the plate and vice-versa, applying the direct and inversion algorithm with the kernel map b suggested. In the inverse problem case, regularization is required because the problem is ill-conditioned. The geometry of the defect will be estimated by the observation of the distribution of the eddy current density on the plate.

4.3 The Direct Problem

To interpret the measured data and find a solution that allows to identify the geometric characteristics of the defect from the eddy current distribution, it is essential to resolve the direct problem first. In this section, a preview of the measurements of the magnetic field is obtained by an analytical process. Considering the two-dimensional problem of current flow (uniform distribution in the absence of crack) around a linear defect with end points at (-L/2,0) and (+L/2,0), it is possible to use a conformal transformation to determine the geometric configuration of the current lines in the presence of a defect. The conformal transformation (P) used to obtain the current density deviating from a linear defect in a limited area [51, 52] is given by

$$P = K[Z^* \cos\alpha - j(Z^* - \left(\frac{L}{2}\right))^{\frac{1}{2}} \sin\alpha] \quad , \tag{4.3}$$

Where $Z^* \in \mathbb{C}$, L is the length of the defect and K is a positive real constant and P is the complex potential. The current lines vary with the angle α . When $\alpha = \frac{\pi}{2}$, the current lines are perpendicular to the defect direction. Figure 4.3 represents the obtained current density around a linear defect with 20 mm of length in an region of 50 mm x 50 mm.

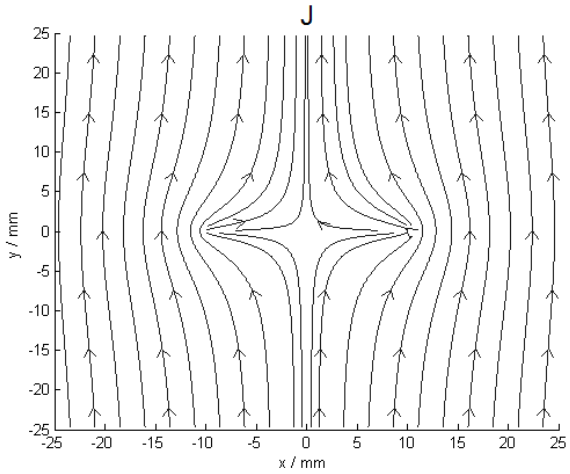

Figure 4.3: Representation of the current density around a linear defect with 20 mm of length by current lines.

Figure 4.4 represents the matrices of each adjacent component J_y and J_x of the spatial current density represented in Figure 4.3

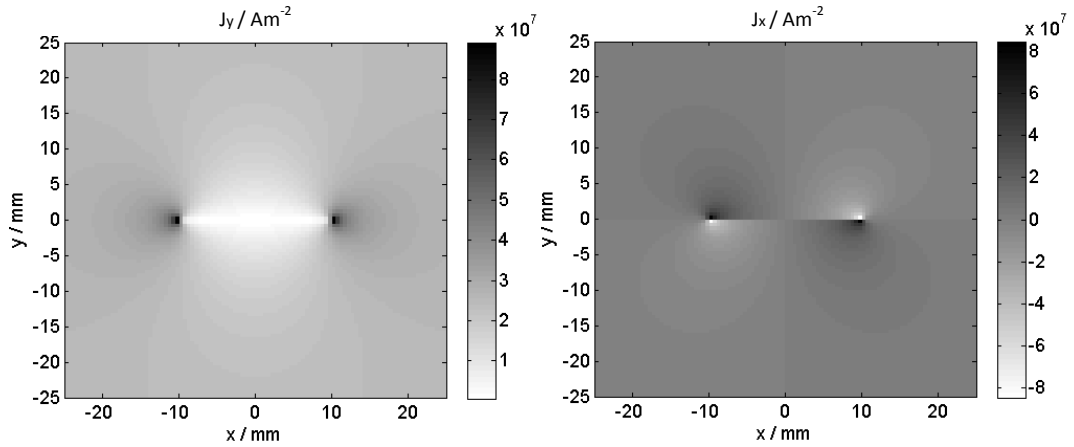

Figure 4.4: Representation of J_y and J_x components of the spatial current density around a linear defect with 20 mm of length by current lines.

The perturbed component can be obtained if we subtract the uniform current density from the current density depicted in Figure 4.3. The resulting current lines is represented in the Figure 4.5.

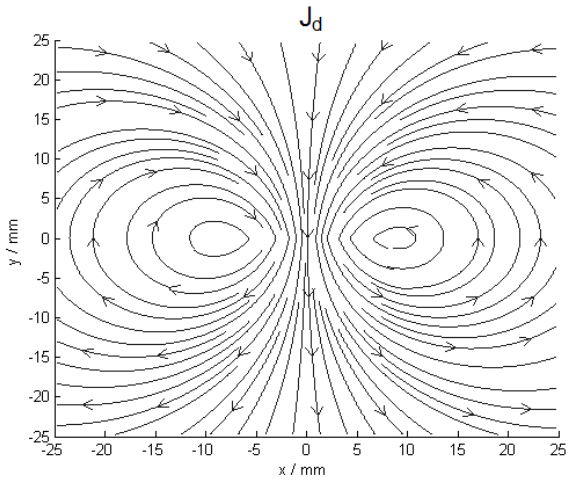

Figure 4.5: Representation of the perturbation component of the current density (J_d) around a linear defect with 20 mm of length.

As expected, it is possible to observe in Figure 4.5 the existence of circulating currents that may be considered as a summation of dipole currents. These dipole currents may be seen in a virtual grid over the plate surface where each square edge is a current dipole element, as depicted in Figure 4.6.

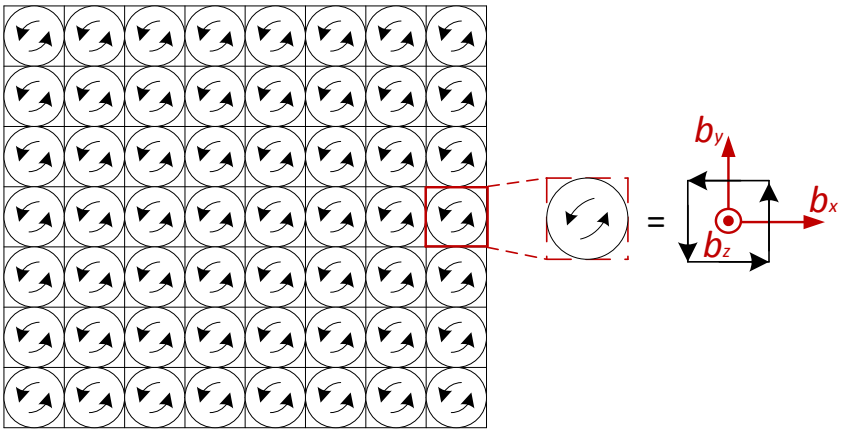

Figure 4.6: Discretization of the perturbation current component into square loops with edges length equal to the step size of the scanning system.

As previously mentioned in section 4.2 the distance between two square edges is equal to the position step between successive measurement points. Considering this virtual grid and using the Biot-Savart law it is possible to obtain the resulting decomposition of the eddy current perturbation of elemental (unitary) dipole currents for the B_x, B_y and B_z components of the magnetic field. The results for the b_x and b_y components are depicted in Figure 4.7 and the maps can be seen as the kernel maps to solve the direct and inverse problem. The distance between the sensing point and the surface on test have to be considered to computed the kernel map b. In the thesis, this distance will be called by z. Here, the distance chosen to compute the kernel map b was 3.5 mm. The calculated maps of b were considered as the field produced by a single elemental dipole with unitary current of 1 A.

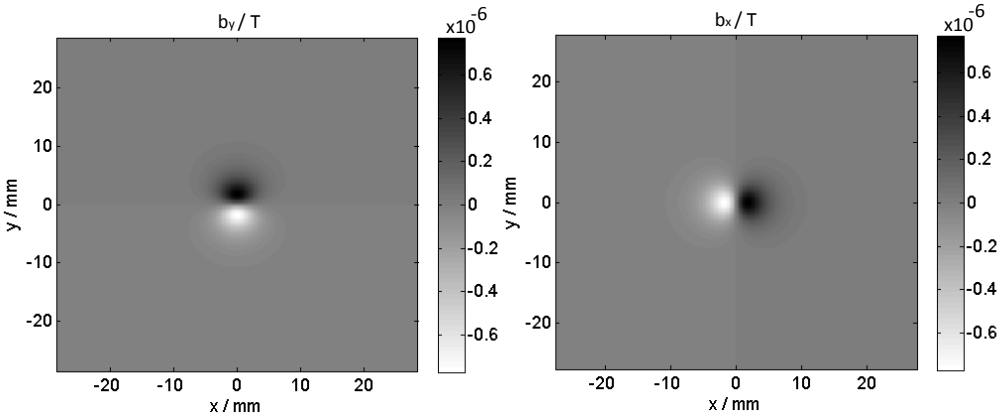

Figure 4.7: Graphic representation of the dipolar current kernel maps b used in transformation **??**.

To clarify the chosen solutions, equation 4.1 can be modified as

$$B_y(m,n) = \sum_{i,j} b_y(m-i, n-j) \times J_d(i,j) \quad , \tag{4.4}$$

and

$$B_x(m,n) = \sum_{i,j} b_x(m-i, n-j) \times J_d(i,j) \quad , \tag{4.5}$$

where B_y and B_x are the matrices with the perturbation of magnetic field component along x and y , b_y and b_x are the kernels and J_d is the map with the dipolar perturbation current induced in the metallic plate.

Knowing the transformation kernel b and the magnetic field map B, the Discrete Fourier Transform (DFT) is applied to equations 4.4 and 4.5 changing the convolution into a simple multiplication. The transformed equation can be presented by

$$\hat{B}_y = \hat{b}_y \times \hat{J}_d \quad , \tag{4.6}$$

and

$$\hat{B}_x = \hat{b}_x \times \hat{J}_d \quad , \tag{4.7}$$

where the symbol $\hat{}$ represents the data in the frequency domain and the multiplication was taken element by element.

In order to verify the direct problem, $\hat{B}_y$ and $\hat{B}_x$ components of the magnetic flux density were calculated for a linear defect with 20 mm of length and compared with simulations. After computing $\hat{B}_y$ and $\hat{B}_x$ from equations 4.6 and 4.7, the inverse DFT was applied to $\hat{B}_y$ and $\hat{B}_x$ and the results of B_y and B_x components are shown in Figure 4.8. The results obtained from simulations using COMSOL Multiphysics [47] are presented in Figure 4.9. The simulations were obtained on a plane for B_y and B_x at a lift-off 3.5 mm of an aluminium plate with a 20 mm linear defect, imposing an uniform eddy current distribution in the metal using a planar coil.

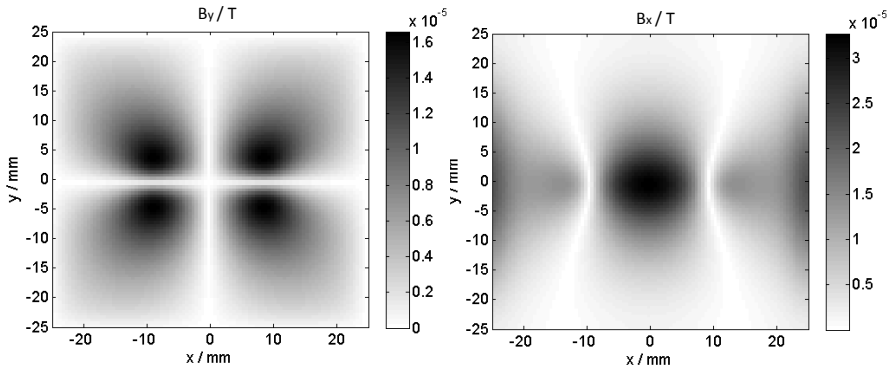

Figure 4.8: Graphic representation of the obtained B_y and B_x components using the equations 4.6 and 4.7.

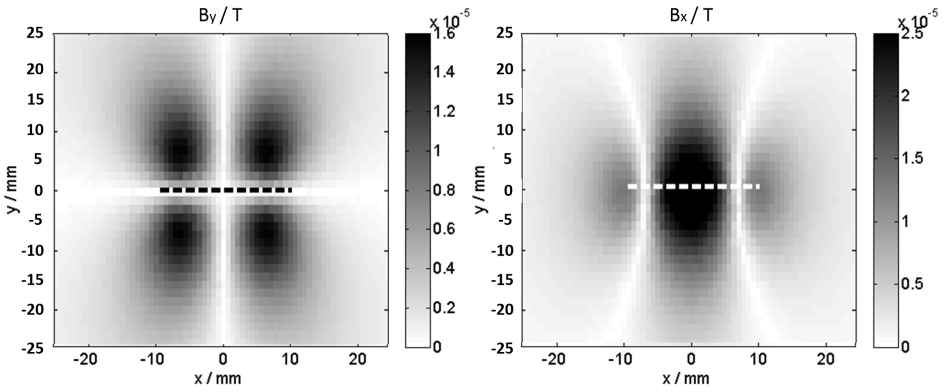

Figure 4.9: Graphic representation of the obtained B_y and B_x components using COMSOL Multiphysics.

The results are similar, showing that the direct problem can be solved using b_y and b_x as kernels. When the direct problem is solved, the results obtained by it may be used to develop a forward model of the magnetic field response for several defects with shape and size known and to compare them with experimental results in an iterative process to estimate the characteristics of a real defect.

4.4 The Inverse Problem

In the previous section it was stated that a way to characterise a defect may be obtained by an iterative solution of the direct problem. However, in our case, we follow a different approach. Having calculated the kernel maps $\hat{b}$ that represent the decomposition of the eddy current perturbation in elemental dipoles of current for the $\hat{B}_y$ and $\hat{B}_x$ component of the perturbed magnetic field, it is possible to study the inverse problem, where the estimation of $\hat{J}_d$ can be obtained from

$$\hat{J}_d = \frac{\hat{B}_y}{\hat{b}_y} \quad , \tag{4.8}$$

or

$$\hat{J}_d = \frac{\hat{B}_x}{\hat{b}_x} \quad , \tag{4.9}$$

where the $\hat{}$ represents the data in the frequency domain.

Observing the two equations, it is possible to say that a small perturbation present in the measurement data can produce a large perturbation in the restored image when the kernel $\hat{b}$ is associated to an ill-conditioned problem. However, the inverse problem was applied to the calculated magnetic field B_x presented in Figure 4.8 to verify if the data can be inverted. Figure 4.10 presents the obtained results for the dipolar perturbation currents J_d . Figure 4.11 presents the total eddy current density J . Note that an uniform current was added to the dipolar perturbation currents to obtain the total eddy current density .

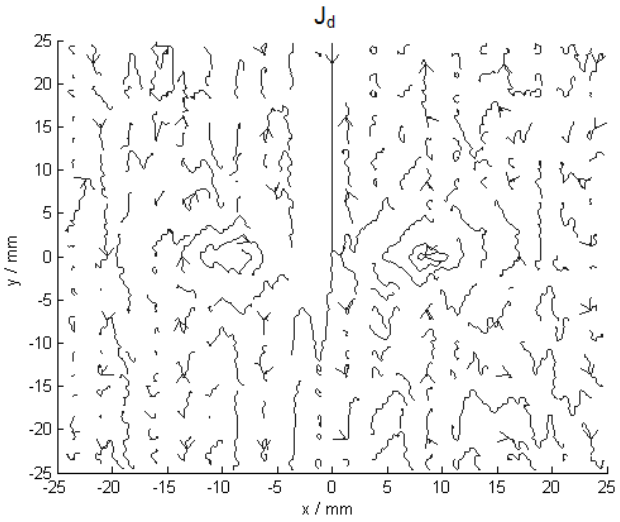

Figure 4.10: Representation of J_d around a linear defect with 20 mm of length applying inverse algorithm without regularization of B_x and b_x.

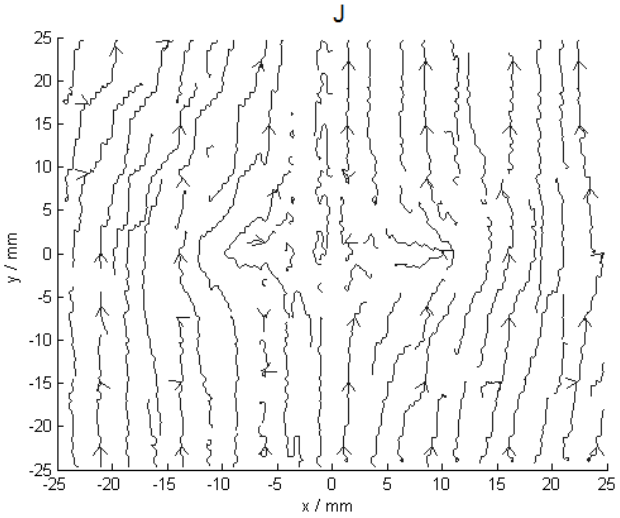

Figure 4.11: Representation of J around a linear defect with 20 mm of length applying inverse algorithm without regularization of B_x and b_x.

It is possible to observe noise in the data. Thus, the problem is very ill-conditioned and regularizations are required to suppress the effect of the noise.

4.4.1 Regularization Methods

The regularization methods are used in digital image processing when noise is present in the data image. The regularization is based on finding approximate solutions depending on a positive regularization parameter. In the case of data without noise, the regularization parameter tends to zero and the regularization functions converge to the solution of the problem. In the case of data with noise, the regularization parameter changes and the optimal approximation solution is given by a non-zero value of the regularization parameter. In the next subsections two regularization methods are presented and used to find approximate solutions of the eddy current density on the plate. The

first method is a regularization equivalent to a filtering of the solution, called Tikhonov regularization. The second method is an iterative regularization called Total Variation regularization that preserve the discontinuities in the restored solution.

4.4.1.A Tikhonov Regularization

Applying the Tikhonov regularization [40, 53, 54] to overcome the inversion difficulty, the kernels are changed to

$$\hat{b}^{\mu} = \frac{\hat{b} \,.\, \hat{b}^{*} + \mu}{\hat{b}^{*}} \quad , \hat{b} = \lim_{\mu \to 0} \hat{b}^{\mu} \quad , \tag{4.10}$$

where $\mu > 0$ is the regularization parameter that controls the roll-off frequencies of the low-pass filter and * represents the complex conjugate. The optimal parameter μ has to be chosen to minimize the effect of the noise present in the measurement data. The dipole current density $\hat{J}_d$ can be expressed as a function of μ by

$$\hat{J}_d^{\mu} = \frac{\hat{b}^{*}}{\hat{b} \,.\, \hat{b}^{*} + \mu} \hat{B} \quad , \tag{4.11}$$

where $\hat{b}$ and $\hat{B}$ can be represented in function of the magnetic field component along x or y.

4.4.1.B Total Variation Regularization

Total Variation Regularization is an optimization method that minimizes a loss function that consists of an energy function and a regularization term (Total Variation regularizer). This kind of loss function can be applied to our problem and the equation of the loss function is given by

$$f(\hat{J}_d) = \frac{1}{2} \times ||\hat{B} - \hat{b} \times \hat{J}_d||_2^2 + \alpha \times TV(\hat{J}_d) \quad , \tag{4.12}$$

where $\hat{B}$ and $\hat{b}$ can be represented as a function of the magnetic field component on x or y, $\hat{J}_d$ is the dipolar perturbation current, $TV(\hat{J}_d)$ is the discrete total variation norm and α is the regularization parameter. The energy function is the absolute difference between the original $\hat{B}$ and estimated $\hat{B}$ $(\hat{b} \times \hat{J}_d)$. The Total variation regularization gives emphasis to differential points of the reconstructed maps.

In our case, as the total eddy current J contains discontinuities for any defect, the use of this solution may help to obtain better results. In this work, an iterative algorithm called Two-step Iterative Shrinkage (TwIST) with TV norm is used to estimate the dipolar perturbation current $\hat{J}_d$ [55].

4.4.1.C Results and Comparison of Tikhonov/Total Variation Regularizations

Applying Tikhonov and TV Regularizations with $\hat{B}_x$ and $\hat{b}_x$, the dipolar eddy current perturbation components $\hat{J}_d$ were obtained. Figure 4.12 depicts J_d (the inverse DFT of $\hat{J}_d$) for both the regularization methods. These perturbations are caused by the presence of the 20 mm linear defect in the material.

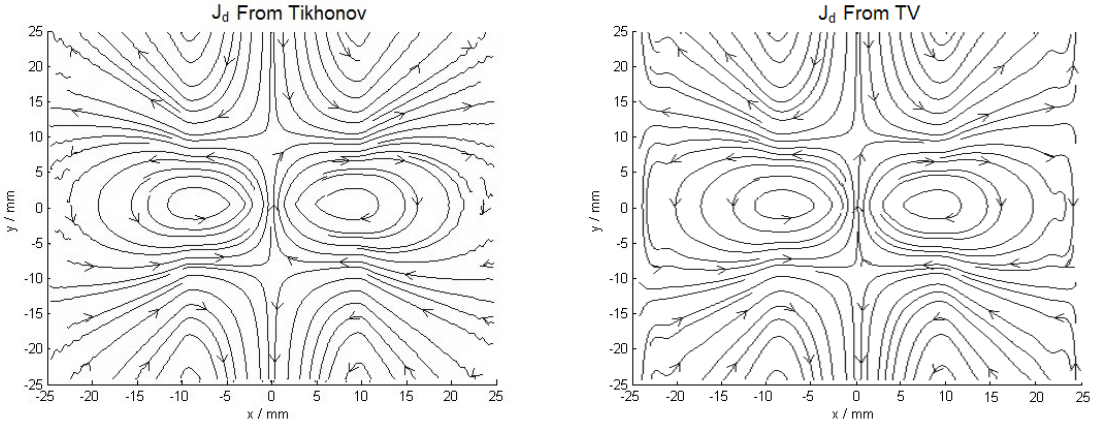

(a) **(b)**

Figure 4.12: Representation of J_d around a linear defect with 20 mm of length applying inverse algorithm from $\hat{B}_x$ and $\hat{b}_x$ with two different regularizations: (a) With Tikhonov regularization; (b) With TV regularization.

To characterize the defects, it is useful to depict the total eddy current density J from the two regularization methods. Figure 4.13 depicts the total eddy current lines J for both cases, while Figure 4.14 depicts the normalized magnitude of eddy current density. Note that the regularization parameter was adjusted manually in the inverse problem algorithms with human observation to obtain the best results.

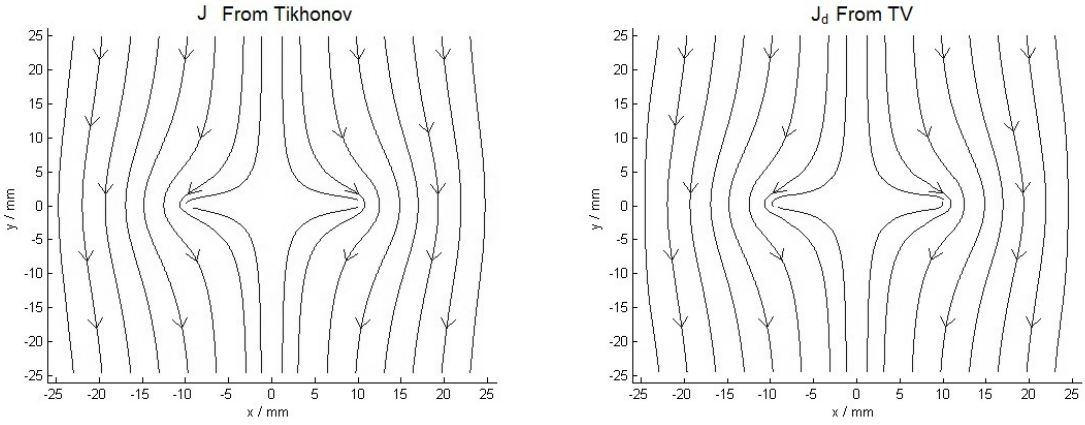

(a) **(b)**

Figure 4.13: Representation of J around a linear defect with 20 mm of length applying inverse algorithm from $\hat{B}_x$ and $\hat{b}_x$ with two different regularizations: (a) With Tikhonov regularization; (b) With TV regularization.

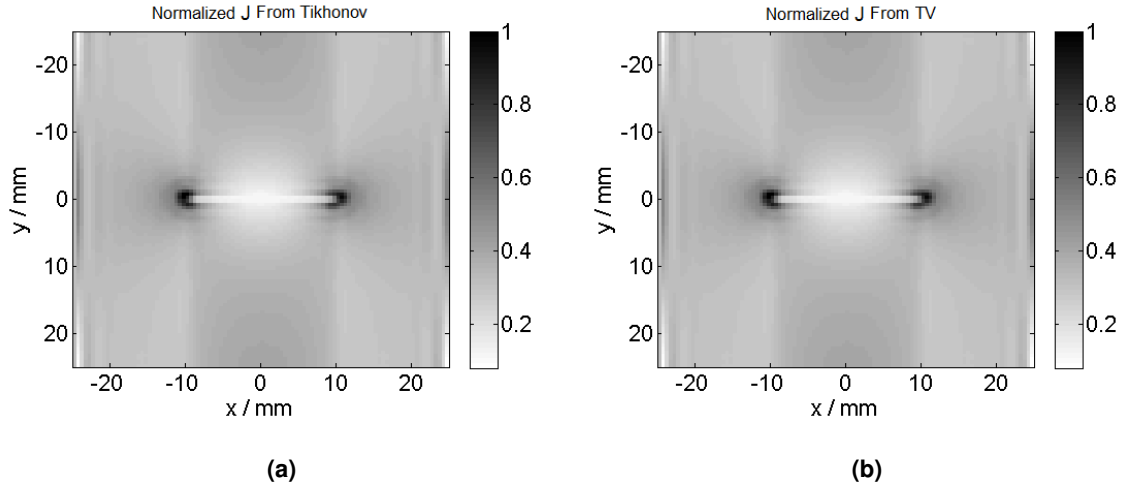

Figure 4.14: Normalized eddy current densities J obtained from estimated magnetic field $\hat{B}_x$ and $\hat{b}_x$ using: (a) Tikhonov regularization; (b) TV regularization.

Observing the results it is possible to obtain the geometry of the defect. The spatial eddy current lines presented in Figure 4.13 clearly show a region where the eddy current density is zero. The perturbation was caused by the presence of a 20 mm linear defect in that zone. Observing Figure 4.14, The white zone is a current-free zone, giving evidence to the defect presence. The black zone shows a high density of current in the limit of the linear defect.

The results show that the application of the Total Variation as a regularization method presents similar results to the Tikhonov method. Table 4.1 presents the comparison between regularization methods about their time performance applying experimental data for a 10 mm linear defect [56].

Table 4.1: Comparison between Tikhonov and TV regularization methods.

Inverse Problem algorithm	Eddy Current Density (J)	Time to process algorithm
With Tikhonov Regularization	Results are Equivalent	< 1 sec.
With TV Regularization		~ 15 sec.

Comparing the two algorithms, the Tikhonov regularization method is faster. As the Total Variation regularization is an iterative algorithm which takes longer time to process, the best choice is to apply the Tikhonov algorithm because it is possible to solve repeatedly the inverse problem and represent graphically the results for parameter values posterior choice within a time period that is previously determined for a known class of problems. The two algorithms were tested for different cracks and the results were similar in all the cases.

4.4.1.D Choice of the Regularization Parameter

In any inversion method that include regularization, the choice of an adequate regularization parameter value is a crucial and a difficult issue in order to obtain a stable solution in the reconstructed

data. Figure 4.15 illustrates the effect of the choice of the regularization parameter μ in the reconstructed image obtained by the inverse problem algorithm using Tikhonov regularization.

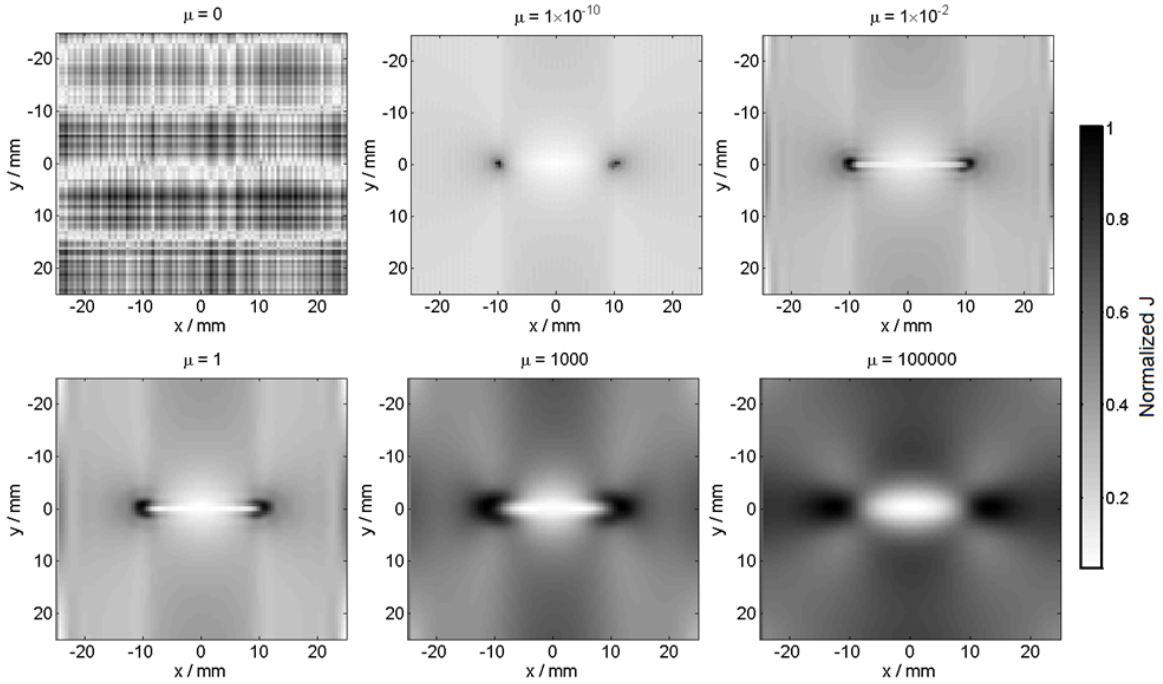

Figure 4.15: Normalized eddy current densities J obtained by the inverse problem algorithm with Tikhonov regularization for a set of regularization parameters μ

It is possible to observe in Figure 4.15 that the choice of the regularization parameter μ influence significantly the reconstructed image. For a parameter value μ close to zero, it is possible to observe that the effect of noise in the reconstructed image is dominant. For larger values of μ, there is an increase of discrepancy between the estimated data and original data.

In practical situations, the optimal regularization parameter value μ is usually unknown, but this parameter value μ may be estimated. In the first stage of tests, the regularization parameters were chosen by visualization of the reconstructed image. In that case, by careful observation of the current density maps obtained from the inversion of analytical data, the chosen regularization parameter value μ was 1×10^{-2}. In the second stage of tests, the optimal regularization parameter value μ was automatically estimated. In this work, two methods were used to estimate automatically an adequate value for μ. The first method uses the relative variation of the reconstructed image energy to estimate the optimal parameter value μ. The second method is based on the L-curve criterion where the energy of the reconstructed images and the discrepancy between the estimated and the measured results are used to find the best parameter value μ. In the next Chapter, section 5.6.3, the two method are explained in detail. The inversion method using Tikhonov regularization with automatic parameter selection was tested with experimental magnetic field maps for three linear defects with different lengths (5 mm, 8 mm, 12 mm).

4.4.2 Test of Kernel Maps to the Simulated Data

The Finite Element Method (FEM) was used to confirm and validate the inverse problem solution previously presented. The simulations were performed in the COMSOL Multiphysics Software. An Al1050 (aluminium alloy) plate with 1 mm of thickness was analysed. The eddy current density at the surface of the plate was obtained when a planar probe inducing an uniform eddy current flow is placed over the plate. A sinusoidal excitation frequency of 5 kHz was used in the simulations. Figure 4.16 (a) depicts the model for which the simulations were performed and Figure 4.16 (b) depicts the simulated eddy current distribution in the aluminium plate.

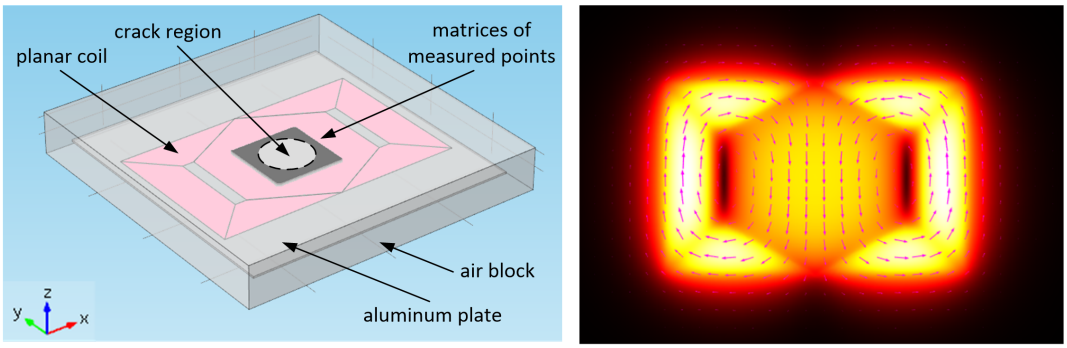

Figure 4.16: Illustration of the simulation model used in this work: (a) 3-D view of the model including the aluminium plate, the planar coil, matrices of points and air block; (b) 2-D view of the simulated eddy current distribution in the aluminium without defect.

The planar coil was designed with seven regions, imposing uniform surface current density at each region. A 0.5 mm lift-off value exists between the coil and the metal plate. A linear crack with 10 mm of length was added to the plate in the center of the uniform region. A matrix of points was added to the surface of the plate in the xy-plane to obtain the eddy current distribution around the crack zone. To measure the magnetic field components at the distance of the sensor, another matrix of points was added at 3 mm above the surface of the plate. A surface current density of 270 A/m was imposed in the y-direction at the center zone of the coil. The surface coil with the returning current has a higher wire surface density, thus a 500 A/m was imposed in the other surfaces (with different directions).

The first simulation was performed to obtain the perturbations of the three magnetic field components B_x, B_y and B_z. Figure 4.17 shows images of the three magnetic field components obtained by simulation. The uniform magnetic field component present in the B_x component was removed in order to extract the magnetic field perturbation part. This uniform magnetic field component is due to orientation of the sensing element be in the same direction of the excitation magnetic field and this uniform part contains the resultant of the sum of the excitation magnetic field and the magnetic field produced by the eddy current.

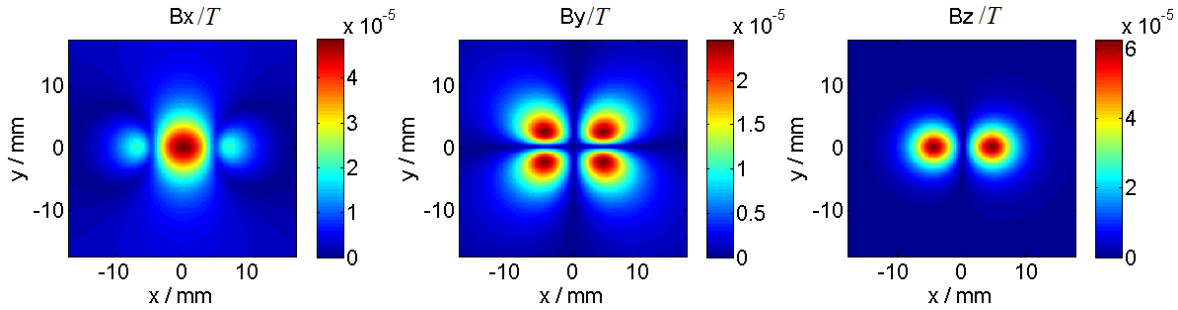

Figure 4.17: 2D Simulation results of the three magnetic field components B_x, B_y and B_z, in the vicinity of a 10 mm long linear defect with 1 mm of depth in a 1050 aluminum alloy plate.

Figure 4.18 shows the images of the three kernel maps b_x, b_y and b_z used in the regularized inversion. These kernel maps are the field produced by a unit current dipole in the x, y and z directions.

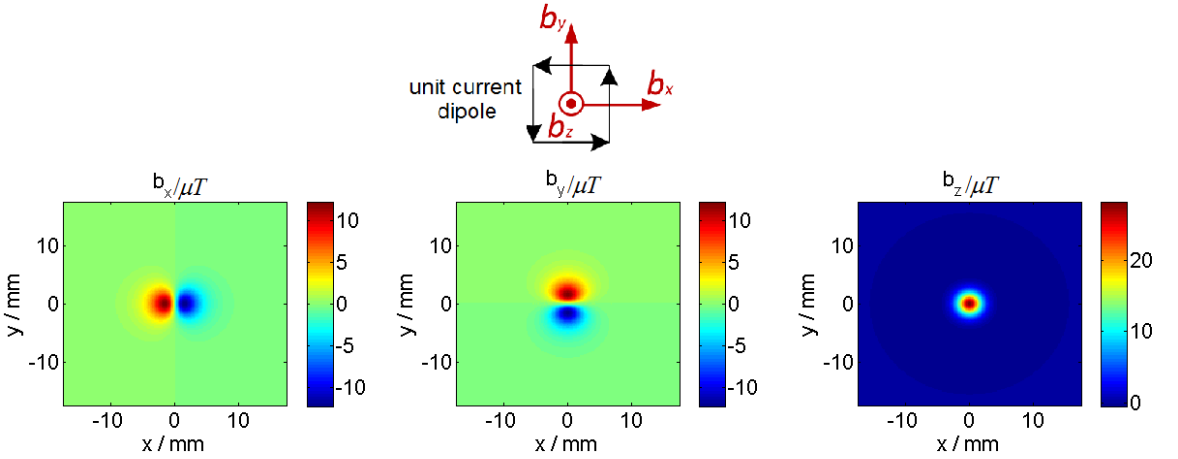

Figure 4.18: 2D images of the calculated kernel maps (b_x, b_y and b_z).

Figure 4.19 shows the resulting images of the inversion process for the total reconstructed eddy current density (J) on the plate with their maps normalized to [0,1]. The data were inverted using Tikhonov regularization.

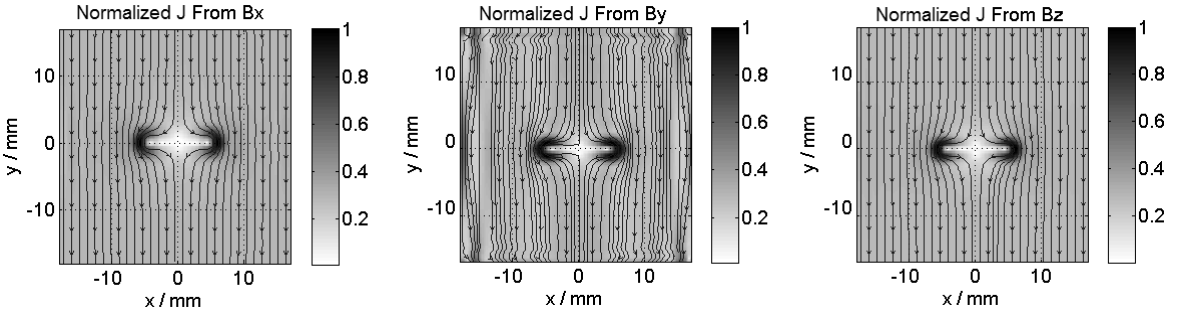

Figure 4.19: 2D normalized eddy current density images obtained in the vicinity of a 10 mm long linear defect by the inversion algorithm, starting with the simulated magnetic field component B_x, B_y and B_z.

From Figure 4.19, it is possible to observe that the normalized distribution of the eddy currents for the three reconstructed images is equivalent and the geometry profile of the defect is evident. The crack geometry is defined by the set of null currents (i.e white zone) between the maximum

density current values (i.e darker zones). The crack length is correlated to the distance between the maximum points of current density. Thus, one of these reconstructed images may be sufficient to give the indication of the length, orientation and geometry profile of the crack.

To verify the results obtained by the inversion of the simulated magnetic field components (B_x, B_y and B_z), a comparison can be made with the normalized eddy current density obtained by the FEM simulation of the direct problem. The eddy current distribution around the crack was obtained by the matrix of points added to the surface of the plate in the simulated model and the result is depicted in Figure 4.20

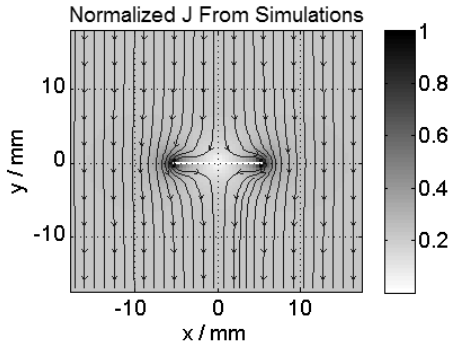

Figure 4.20: 2D normalized eddy current density image obtained by the FEM simulation in the vicinity of a 10 mm long linear defect with 1 mm of depth.

The images show good agreement between the simulated image and the calculated images. Comparing Figure 4.19 and Figure 4.20 it is possible to observe that the distribution of eddy currents from Figure 4.19 are less concentrated than in Figure 4.20.

Part of this effect may be due to the fact that Tikhonov regularization acts as a low-pass filter in the frequency domain in the inversion process. Furthermore, in the inversion process, the reconstructed images contain the information of perturbed currents that occur along the depth of the material concentrating in an image plane, while the obtained image from the FEM only gives the information of perturbed eddy currents in a plane in the metal surface.

The reconstructed eddy current distributions obtained by the simulated magnetic field components B_x, B_y and B_y allow to conclude that the kernels b_x , b_y and b_z are adequate to solve the inverse problem when uniform current distribution is applied. However, regularization methods are required because we are dealing with a severely ill-conditioned problem.

5

Plate Inspection

Contents

5.1 Chapter Summary

In this chapter, simulation and experimental work are presented in order to characterize defects in metallic structures. This chapter is divided in five sections. Section 5.2 presents the designed experimental probe and the built current generator module developed to make an experimental eddy current inspection. Section 5.3 presents the experimental system used to evaluate the location, characterization and dimensions of the defect. Section 5.4 presents the signal processing used to minimize unwanted noise that can be superimposed to the signal with defect information. Finally, section 5.5, section 5.6 and section 5.7 relate the experimental and simulation work made to characterize the defects according to its depth and geometry.

5.2 Initial Probe Design

For plate inspection, the probes were especially designed to induce currents in the plate using a spatially invariant excitation field with sinusoidal excitation. In a initial stage, two probes similar to the one that is depicted in Figure 5.1 were designed and built to make the inspection of aluminium plates. These probes were implemented at our laboratory with an excitation coil with 51 turns and Giant Magnetoresistorss (GMRs) as magnetic sensors. The probes were manufactured on a printed board with parallel lines in the central region. The geometry of the excitation planar coil produces a spatially invariant excitation field on an area around the GMR sensor, resulting in an uniform distribution of the eddy currents in the metallic surface.

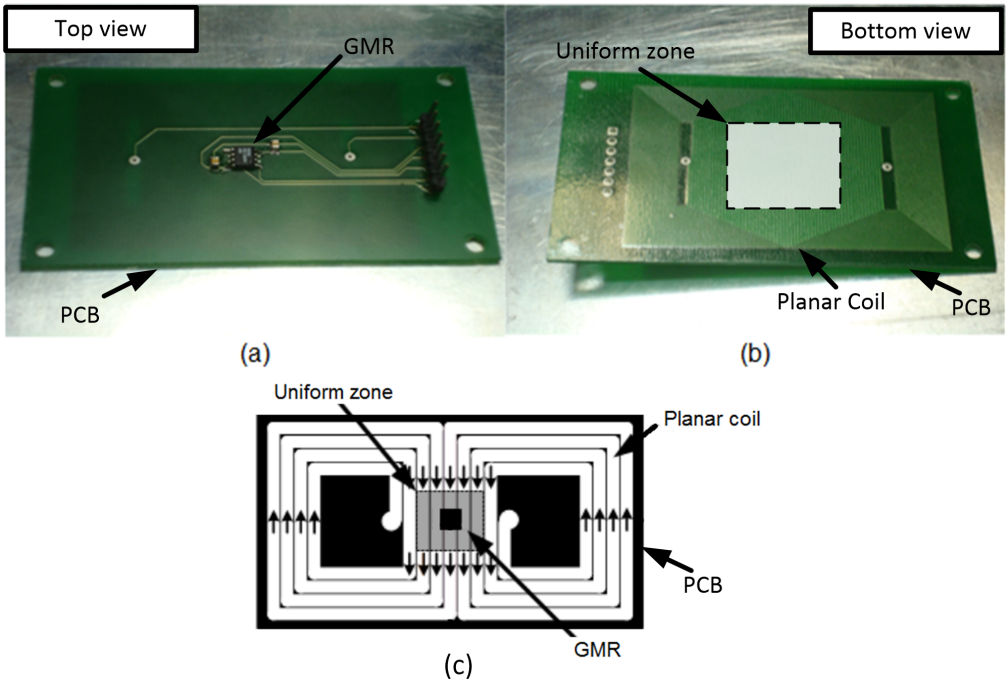

Figure 5.1: Illustration of one of the built probes: (a) Top view of the printed board; (b) Bottom view of the printed board; (c) Representation of the probe.

For each probe, the sensor is mounted with its sensing axis either parallel or perpendicular to the excitation current as it is represented in Figure 5.2. Along chapter 5, the magnetic field measured by this sensor will be represented by B_y or B_x, respectively. The term Probe 1 (with GMR sensing axis to measure B_y) and Probe 2 (with GMR sensing axis to measure B_x) will be also used to represent the two different probes.

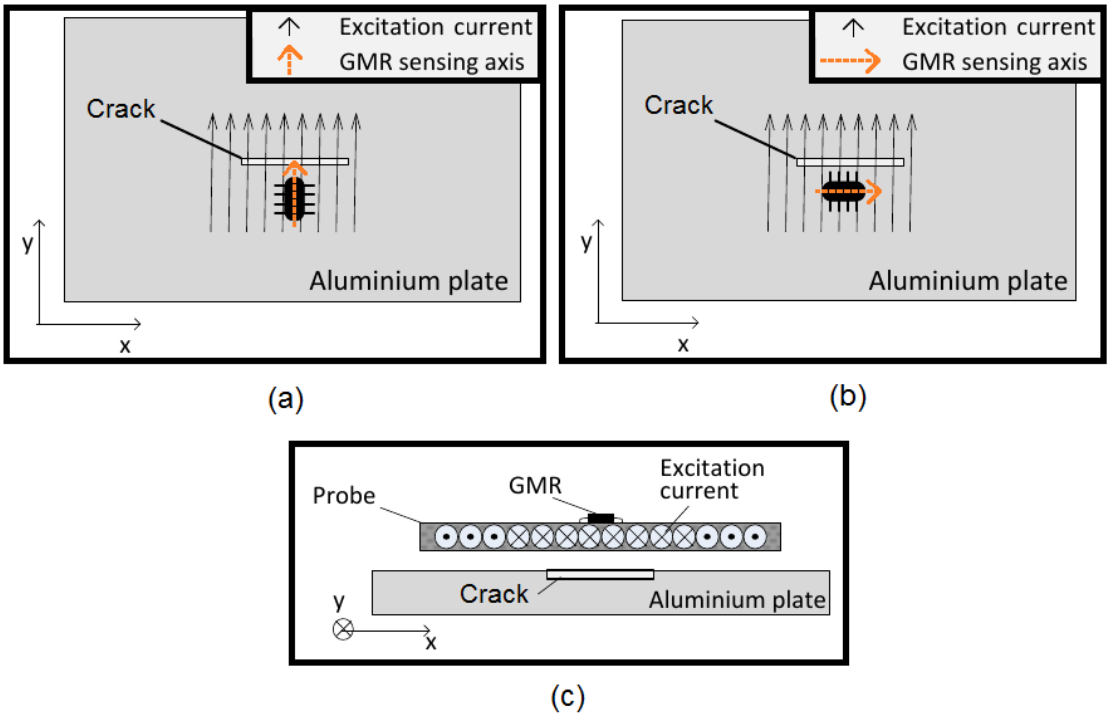

Figure 5.2: Illustration of the position of the GMR sensor for each probe: (a) GMR sensing axis parallel to the excitation current (Probe 1); (b) GMR sensing axis perpendicular to the excitation current (Probe 2); (c) Profile view of the probes.

The size of the uniform area has to be larger than the defect, so that the defect is surrounded by the uniform current distribution. As the defects on test are between 5 mm and 20 mm of length, the chosen uniform area was (25×20) mm^2.

The planar coil was chosen to keep a constant contact with the metallic surface in order to reduce the lift-off effect that is one of the problems that affects the results measured with the most eddy current testing probes. GMR sensors were chosen due to their high sensitivity along their wide frequency bandwidth, helping to examine sub-surface defect characteristics in a low frequency operation. The choice of the frequency is related to the skin effect already explained in chapter 2, section 2.3.2.

A LCR meter (HIOKI 3532) was used to characterize the impedance (Z) of the planar coil for different test frequencies (f). The magnitude of the impedance ($|Z|$) and the phase (θ) difference between voltage and current that flows in the coil were obtained. Table 5.1 presents the results measured by the LCR meter for $|Z|$ and θ at different test frequencies (f).

Table 5.1: Magnitude and phase characteristics of the planar probe as a function of test frequency.

f(Hz)	$\|Z(\Omega)\|$	θ (degrees)
10	14.396	$\approx$0
100	14.479	0.08
1000	14.479	1.21
10000	14.640	11.90
20000	15.501	22.83
30000	16.628	32.26
50000	20.248	46.40

The results show that the impedance of the planar coil can be considered as resistive when test frequency (f) is lower than 1000 Hz. For higher value of f, the impedance begins to be inductive and a tuning circuit can be necessary to remove unwanted oscillation in the voltage signal. In the next sub-subsection, the built current generator circuit with tuning is presented.

5.2.1 Current Generator Circuit

A current generator circuit was implemented using a power operational amplifier LM675 (from Texas Instruments) in a transadmittance setup. This kind of setup allows the conversion of a alternating voltage source to a proportional alternating current source. The implemented circuit is depicted in Figure 5.3. The current (I_s) imposed in the planar coil is proportional to the input voltage (V_{in}).

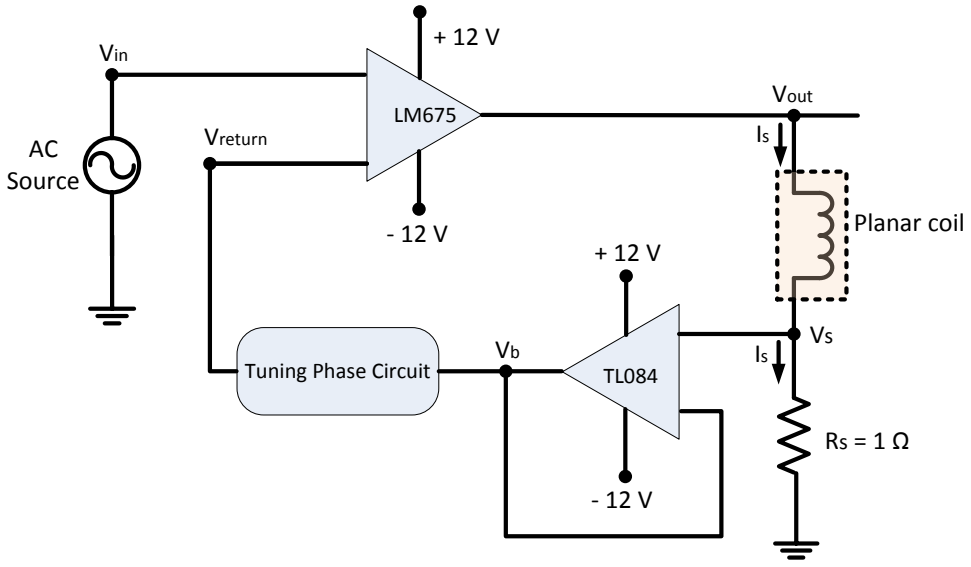

Figure 5.3: Circuit model of the current generator.

The LM675 amplifier was chosen because of its capability to provide 3 A output current. The current output of the amplifier I_s is given by

$$I_s = \frac{V_{in}}{R_s} \quad , \tag{5.1}$$

where the resistance R_s is fixed with value equal to 1 Ω and V_{in} is the voltage source that controls I_s. An operational amplifier TL084 (from Texas Instruments) was used as buffer amplifier with gain equal to one to limit the current in the feedback signal. A tuning phase circuit was added to the feedback circuit to bring back the phase shifted signal (caused by the coil impedance) to its original phase because of the LM675 amplifier works correctly only when both the inputs are in the same phase. This part of the circuit is depicted in Figure 5.4.

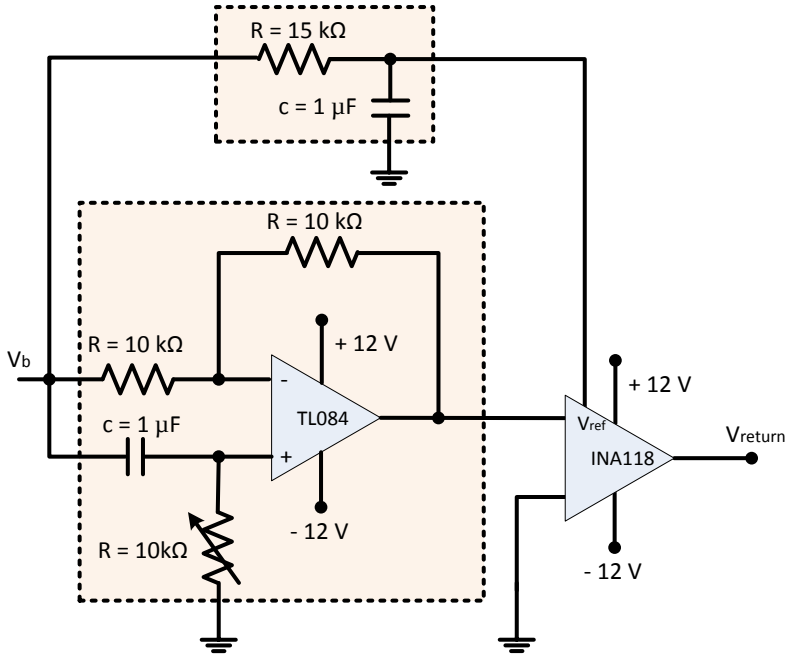

Figure 5.4: Circuit model of the tuning phase.

The phase of the signal was adjusted by an operational amplifier TL084 with gain equal to one that acts as an active phase shift filter. The output of this op-amp is controlled by a potentiometer. Since there is a capacitor in the input of the TL084 amplifier, the DC component is blocked. So a low pass filter is used to filter the AC component getting only the DC component of the signal. The DC value is added to the phase shifted signal using a INA118 instrumentation amplifier to obtain the corrected signal which is in phase with the original excitation AC source.

5.3 Initial Experimental Setup

To evaluate experimentally the location, characterization and dimensions of a defect, a experimental system was used to this purpose and is depicted in Figure 5.5. One planar excitation coil is represented over an aluminium plate. The probe includes the excitation coil and a GMR magnetic sensor already presented in section 5.2. In a initial stage, an alternating current with fixed amplitude and frequency was imposed on the planar coil by a FLUXE 5700A calibrator controlled by GPIB interface. The maximum amplitude current achieved to imposed on the planar coil using this calibrator was 210 mA. In a second stage, the current generator circuit presented in subsection 5.3 was used to excite the coil with higher currents. The probe is attached at a XY positioning system controlled by a RS232 interface inserted in a PXI-1036 chassis from National Instruments. The support that attaches the probe to the positioning system allows the rotation of the probe with 1 degree of resolution. The positioning system can be moved with steps of 0.05 mm to 0.05 mm to evaluate the sample plate. Thus, for every 0.05 mm, it is possible to acquired the magnetic field from the GMR sensor by a multifunction DAQ board (NI-PXI-6251) inserted in the PXI Chassis. The board has 16 analog inputs with 16-bit of resolution, a maximum sampling rate of 1.25 MS/s per channel and 7 input ranges from $\pm$ 0.1 V to $\pm$ 10 V. The DAQ also monitors the excitation current in the planar coil through a 1 Ω sampling resistor (R_s). When the FLUXE 5700A calibrator was used, the resistor R_s was directly connected in series with the coil. When the current generator circuit was applied, the resistor R_s is the used resistor depicted in equation 5.1. The complete system works under control of a MATLAB program running in a desktop personal computer.

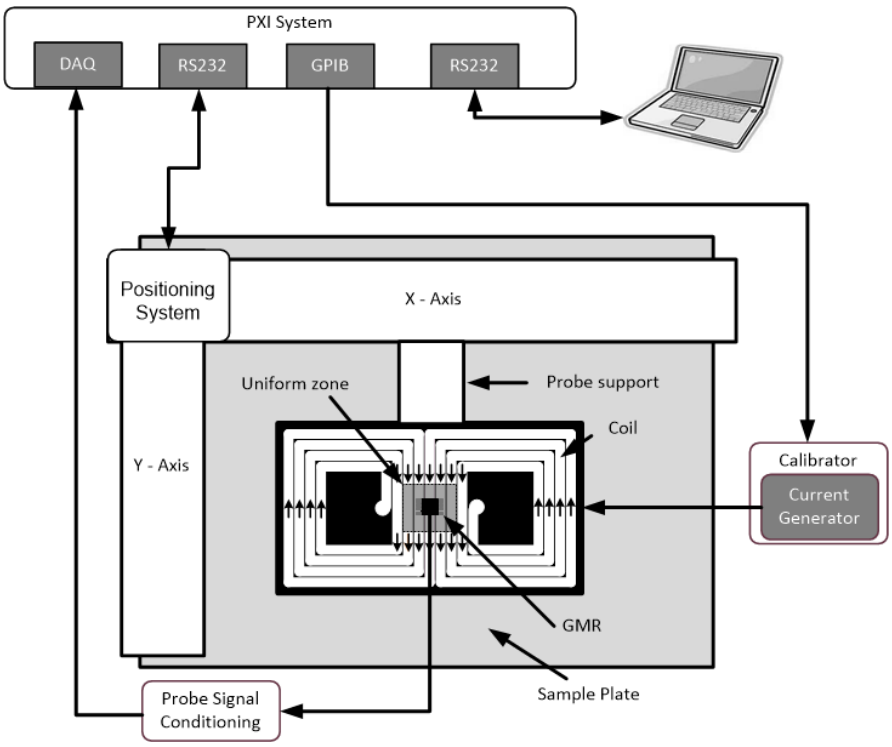

Figure 5.5: Experimental setup with the excitation coil over an aluminium plate.

Figure 5.6 depicts the probe conditioning circuit used at the output of the GMR sensor that includes an instrumentation amplifier with G=46 dB and a band-pass filter (from 150 Hz to 20 kHz) to remove the DC component from the output of the GMR sensor, to attenuate the 50 Hz noise and to remove the noise signal originated by the step-motors of the positioning system. The magnetic sensor and the conditioning circuit were powered by a power supply Calex BPS4000 with symmetric voltages of +/-12 V.

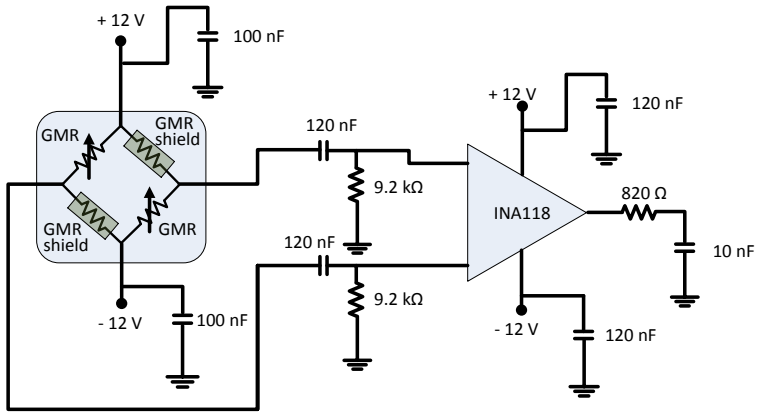

Figure 5.6: Conditioning circuit to GMR output sensor.

The data acquired by the DAQ Board are performed by a three-parameter sine-fitting algorithm implemented in the MATLAB program. Figure 5.7 depicts the interface developed in MATLAB software in order to control the take field measurements of the magnetic field perturbations around defects. Experimental results obtained by the program will be presented in the next subsection.

Figure 5.7: Interface developed in MATLAB software to make a scan area around the defect zone.

The general block diagram of the inspection system applied to analyse an aluminium plate is shown in Figure 5.8.

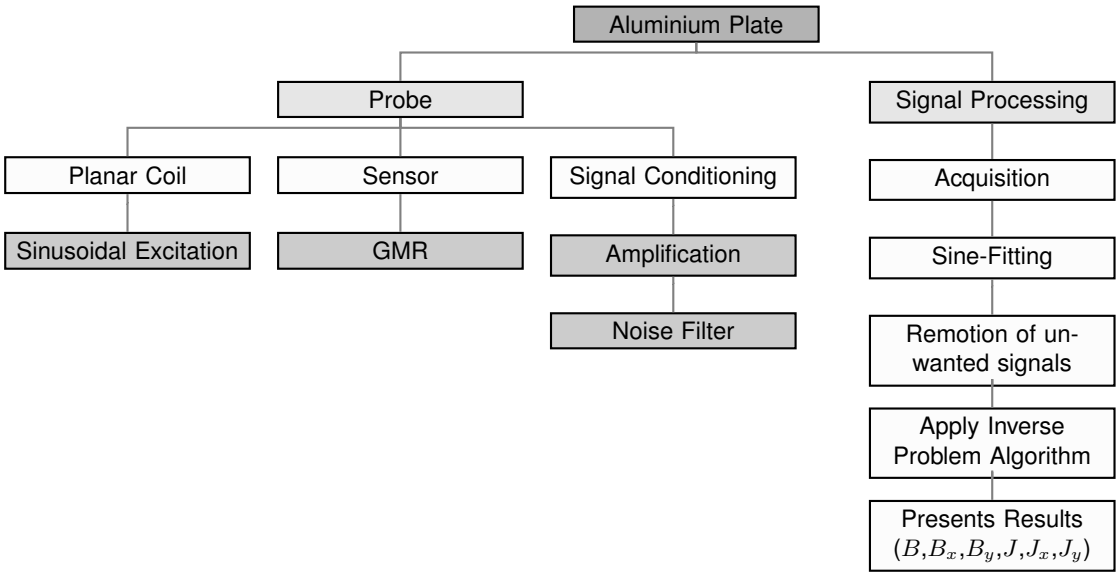

Figure 5.8: General inspection system applied in the aluminium plate.

5.3.1 2D Images of the Magnetic Field Around Cracks

The magnetic field response measured by the sensing axis of a magnetic sensor does not directly measure the physical property of interest, however, it contains the information about defect perturbations in the magnetic field. Two magnetic fields exist when the magnetic field is measured in eddy current testing. The first is the magnetic field generated by the excitation probe and the second is the magnetic field associated to the induced eddy currents in the material on test. The eddy currents are perturbed in a region with defect, and the secondary magnetic field contains the information about the perturbations. In this section, two scans were performed over a machined defect with 20 mm of length. The first scan is performed with the GMR sensing axis parallel to the current lines measuring B_y and the second scan is performed with the GMR sensing axis perpendicular to the current lines measuring B_x. Figure 5.9 presents the magnetic field components (B_x and B_y) obtained with numerical model and experimentally. In experimental results, the positioning system moved the probe with steps of 1 mm in a area of (50$\times$50) mm^2 in order to measure the amplitude of the GMR output voltage for each point. The variation of the amplitude values are proportional to the variation of the magnetic field values along the fixed direction of the GMR sensing axis. The amplitude values were converted to tesla using the sensitivity of the GMR sensor equal to 3.6V/mT per V of the power supply. The mean value of the magnetic field measured in zones free from any perturbation was subtracted from the measured data to remove the influence of any fields not originated from the current perturbations.

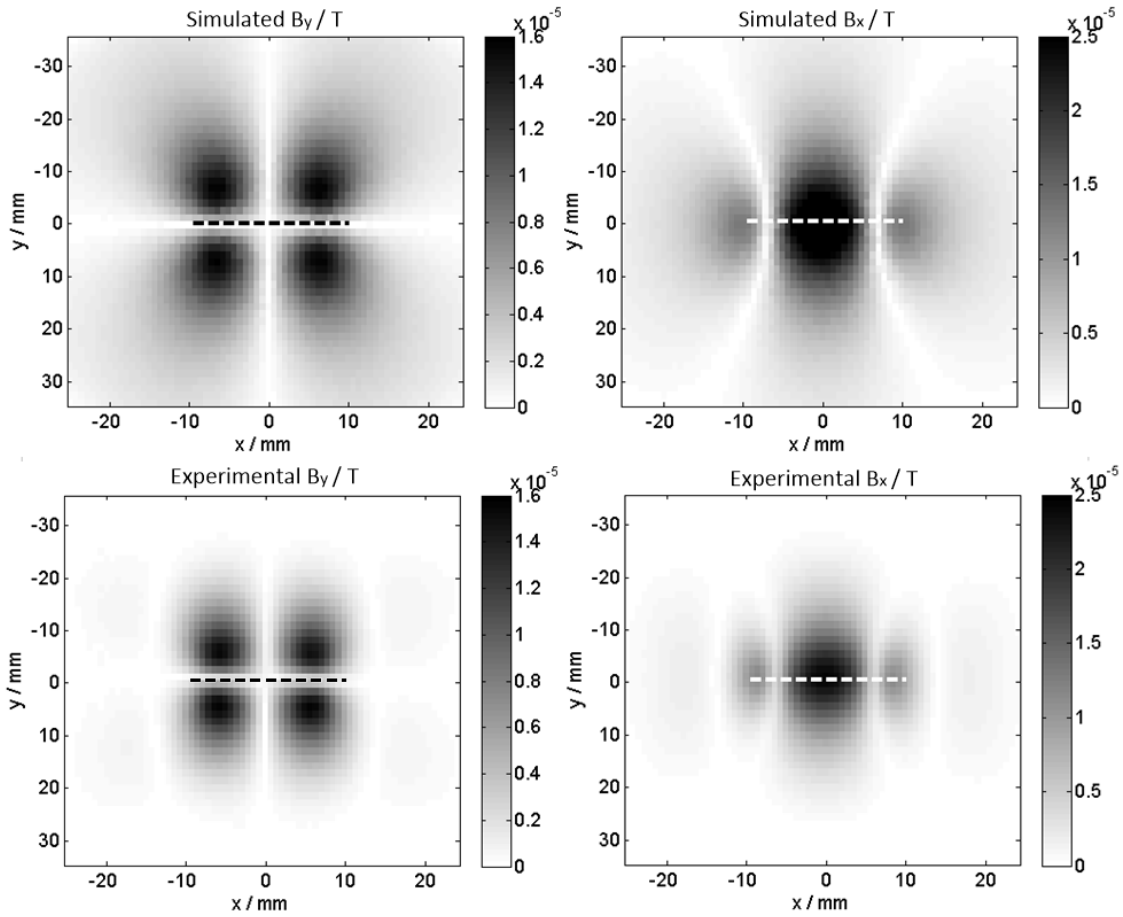

Figure 5.9: Simulated and experimental magnetic field B_x and B_y for a 20 mm linear defect.

Observing the results, it's possible to say that the information regarding the length of the defect can be estimated from either magnetic fields components B_x or B_y. However, the estimation of the defect depth and the geometry of the defect from the measured magnetic fields is harder than the estimation of the defect length.

5.4 Signal Processing

To interpret correctly the value of the signal in eddy current testing it is essential to minimize the noise which is superimposed to the signal with information. In our case, the noise that affects the measurement data set can emerge from several sources, such as, external electrical sources, unwanted excitation field presence and lift-off effect presence. For these purposes, digital signal processing techniques were developed in this work to improve the available measurement data.

5.4.1 Three-Parameter Sine-Fitting

At each position of a scanning area, data is acquired during some periods of the excitation current at the maximum sampling frequency of the board. The high sensitivity of the GMR sensor in a large frequency range (DC to 1 MHz) allows us to obtain significant signal information about the magnetic field perturbation around defects. However, this high sensitivity of the sensor to magnetic field varia-

tions also results in a high sensitivity to unwanted noise (from external magnetic field sources) close to it, such as the stepper motors used in the xy positioning system. To solve this problem, a sine-fitting algorithm is used to extract the parameters of a sinus from a set of noisy observations and compress the information for each measured point. Those parameters include: amplitude, offset, initial phase and frequency [10]. On a three-parameter sine-fitting algorithm, as the one used in this work, the operation frequency is known while amplitude and phase are the parameters to be estimated.

The acquired sine signals can be presented by the expression:

$$y(t) = A\cos(2\pi ft + \phi) + C \quad , \tag{5.2}$$

or

$$y(t) = A_l\cos(2\pi ft) + A_Q\sin(2\pi ft) + C \quad , \tag{5.3}$$

Where A is the amplitude, ϕ is the phase, C is the DC component and f is the signal frequency of the sinusoidal signal. The estimates of the sine wave that best fits, in a least square error sense, to M data points, are obtained with:

$$\begin{bmatrix} A_l \\ A_Q \\ C \end{bmatrix} = (M^T M)^{-1} M^T \begin{bmatrix} y_{t_1} \\ \vdots \\ y_{t_N} \end{bmatrix} \quad , \tag{5.4}$$

where:

$$\mathbf{M} = \begin{bmatrix} \cos(2\pi ft_1) & \sin(2\pi ft_1) & 1 \\ \cos(2\pi ft_2) & \sin(2\pi ft_2) & 1 \\ \vdots & \vdots & \vdots \\ \cos(2\pi ft_N) & \sin(2\pi ft_N) & 1 \end{bmatrix} \quad , \tag{5.5}$$

and M^T is the M transpose matrix.

The amplitude can be computed from the in-phase amplitude, and in-quadrature amplitude, using:

$$A = \sqrt{A_l^2 + A_Q^2} \quad , \tag{5.6}$$

and the estimated phase of the sine wave can be obtained with:

$$\phi = -arctan\left(\frac{A_Q}{A_l}\right) \quad , \tag{5.7}$$

The three-parameter sine-fitting estimation is used in both sensor output and excitation current to minimize the effect of sensor nonlinearity, quantization error and random noise. The estimation phase difference between both sensor output and excitation current contains the information of phase variation when a defect is present. Amplitude of the sensor output (A_{sensor}) and the phase difference between sensor output and excitation current $(\phi_{(sensor)} - \phi_{(coil)})$ are the data used to obtain eddy current distribution in the inverse problem algorithm.

The next section presents a study made to quantify the noise present in the acquired data and a study made to quantify the sine-fitting estimation error due to the acquired data noise. The signal-to-noise ratio (SNR) was quantified in both cases for one example of an experimental map.

5.4.2 Quantification of the SNR

Noise can be a problem when a high sensitivity magnetic sensor is used in eddy current testing, specially when the amplitude of the sine wave signal is in the same order of amplitude of the noise affecting the results for the three-parameter sine-fitting estimation. The quantification of the signal-to-noise ratio (SNR) is important to provide measures with the information of the quality of the image for image defect characterization.

5.4.2.A Quantification of the SNR in the Acquired Data

In this subsection, the attentions are focused on the sine-wave amplitude estimation in the presence of additive noise. The noise present in the output magnetic sensor after amplification and band-pass filter plus the estimated amplitude of the sensor output (A_{sensor}) obtained by sine-fitting algorithm is used to quantify the SNR present in the acquired data. Note that the filter applied to the sensor output signal already improves the SNR value. For each acquired output signal, the SNR can be estimated in order to give information about the quality of the acquired signals. As an example, the SNR for each point of the probe movement was calculated covering an area with defect. The scan was performed over an aluminium plate with 2 mm of thickness with a surface defect of 10 mm length and 1 mm of thickness. The probe with GMR sensing axis parallel to the current lines was used to map the perturbation of the amplitude of the output magnetic sensor signal in an area of (60$\times$60) mm^2 with steps of 1 mm. The test was made for excitation current of 200 mA and excitation frequency of 1 kHz. The experimental scan details are presented in Table 5.2.

Table 5.2: Experimental scan details to investigate the data noise present in the acquired signal.

Aluminium Plate	
Sample Size (mm)	$400 \times 300 \times 2$
Conductivity (S/m)	3.559×10^7
Defect Size (mm)	$10 \times 1 \times 1$
Probe	
Excitation Current (A)	0.2
Operating Frequency (kHz)	1
Scan	
Scan Step Size (mm)	1
Scan Map Size (mm)	60×60

At each step of the probe movement, the sensor sinusoidal signal was acquired with 80 points per period during 100 periods of the excitation current frequency. For each position of step, the three parameter sine-fitting algorithm was used to extract amplitude, phase and DC value of the sinusoidal sensor output to construct a sinusoidal signal without noise with the same number of points and periods acquired from the output of the magnetic sensor. This signal was used to separate the noise present on the output signal in order to quantify the SNR for each step of the probe movement.

The root mean square (RMS) value of the reconstructed sinusoidal signal without noise A_{rms} and the noise component of the signal N_{rms} were computed in the time domain by

$$A_{RMS} = \sqrt{\frac{1}{N} \times \sum_{i=1}^{N} (v_i - \mu)^2} \quad , \tag{5.8}$$

and

$$N_{RMS} = \sqrt{\frac{1}{N} \times \sum_{i=1}^{N} (n_i - \mu)^2} \quad , \tag{5.9}$$

where v is the reconstructed sinusoidal signal without noise in the time domain, n is the noise component of the signal in the time domain, μ is the mean of the signal and N is the total number of points of the acquired signal at each point of measurement. Figure 5.10 depicts the two RMS maps obtained for the complete scanned area.

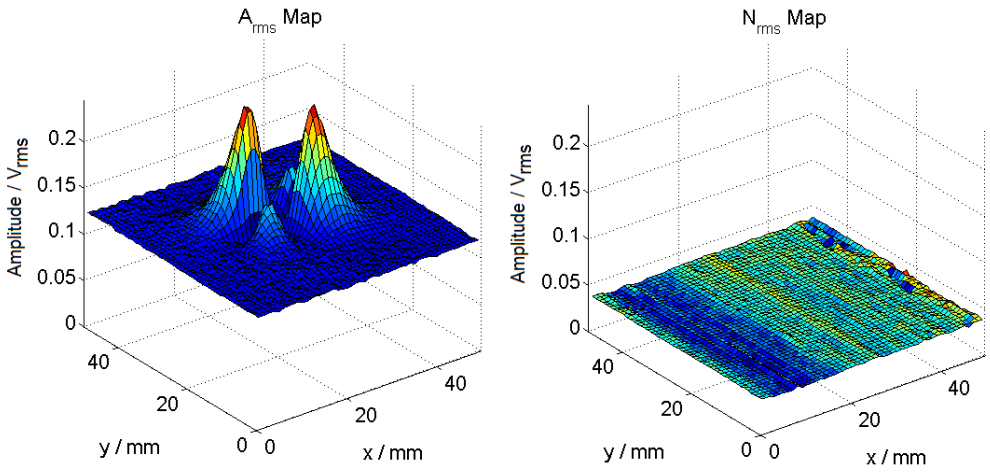

Figure 5.10: Representation of the A_{rms} and N_{rms} maps obtained from equations 5.8 and 5.9.

The SNR of each probe point can be estimated by

$$SNR = 20 \log \left(\frac{A_{rms}}{N_{rms}} \right) \quad (dB) \quad , \tag{5.10}$$

Figure 5.11 depicts the SNR map obtained (in dB) for the scanned area made.

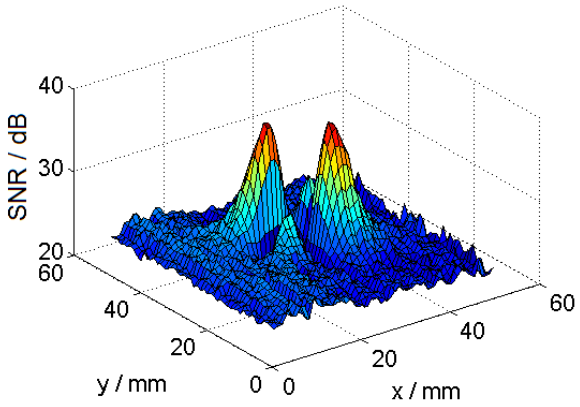

Figure 5.11: Representation of the SNR map obtained (in dB unit) from equation 5.10.

The results show that the SNR is around 25 dB in the uniform zone, while the SNR value is 38 dB in the peak of the amplitude perturbation. As expected, the uniform zone without defect perturbation presents a worse SNR than in the region with defect perturbation. This is due to the position of the GMR sensing axis parallel to the current lines, measuring a small amplitude of the sinusoidal signal in the free-defect zone. Ideally, this amplitude should be zero when there is no defect.

5.4.2.B Quantification of the SNR in the Image after Applying the Sine-fitting Algorithm

The presence of noise in the signal acquisition is reduced when the sine-fitting algorithm, using least squares method, is applied. However, the noise causes errors in the estimated parameters from the sine-fitting algorithm. The next study is focused on the errors in the estimated parameters, in order to understand its significance. In this thesis, it is considered that the quality of the image is good when the SNR value of the image in the defect region is greater than 40 dB.

A scan was performed over the aluminium plate in a region without defect in the same excitation probe condition presented in the previous section. The probe moved in an area of (40$\times$40) mm^2 with steps of 1 mm. Figure 5.12 depicts the estimated amplitude map obtained from the sine-fitting algorithm. Ideally, this map should present a constant value along all map.

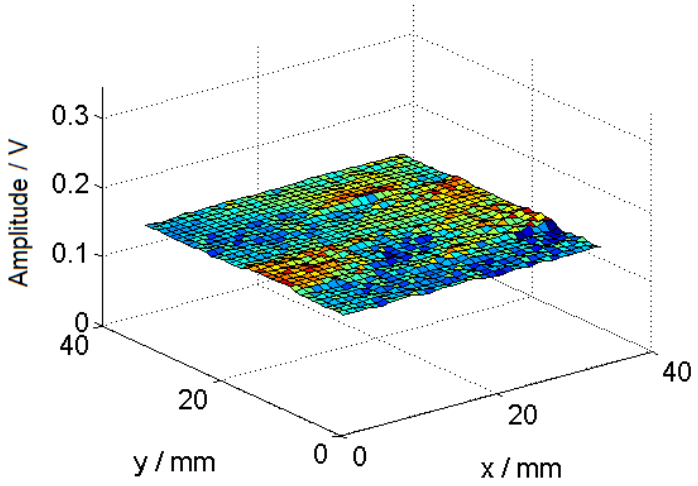

Figure 5.12: Representation of the amplitude map obtained by the output sensor (in voltage units) only considering the uniform zone.

The mean of the amplitude map, depicted in Figure 5.12, was removed from the map and the RMS value was calculated to quantify the variation of the amplitude map error. The RMS value of this amplitude map is equal to 3.4 mV_{rms}. To qualify the images obtained after applying the sine-fitting algorithm, the SNR value in the area of defect is calculated. For the example presented previously in subsection 5.4.2.A, the maximum RMS value in the defect area removing the mean is equal to 0.125 V_{rms}. From equation 5.10, the corresponding SNR value in this point is equal to 72 dB. This SNR value shows that we are dealing with a good image quality in the defect zone allowing the use of this map in our defect characterization application. Note that this evaluation of the quality of the image have to be done before analysis of the image information.

5.4.3 Unwanted Effects Subtraction

Other than the noise illustrated in the previous section, the images can contain other unwanted signals, such as lift-off effect, presence of the excitation field and edge effect. The signal processing explained in this section removes the three unwanted signals with the same algorithm.

The lift-off effect is one of the problems that affects all kinds of probes. This effect is originated by the non-constant gap between the probe and the metallic surface on test. Despite the designed planar coil was made to minimize the lift-off effect on plate inspection, this effect can appear if the probe contact with the metallic plate is not uniform along the scan test. The edge effect only occurs when the probe scans an area at the end of the metallic plate. In these instances, the eddy current flow in the sample on test is distorted from the original uniform current distribution. To remove the lift-off effect and edge effect, a fit of the amplitude surface that contains this effect information has to be removed from the measured data. The amplitude sensor output and the phase difference between the sensor output and the excitation current is used to process the data in the complex domain. In the case when the magnetic field B_x is measured, the presence of the excitation field is expected and the border effect will be more evident. In that case, the magnetic field measured by the sensor output is the sum of the excitation magnetic field and the secondary magnetic field produced by the induced eddy currents. In a region without defect, the magnetic field measured by the sensor output is constant. This constant magnetic field, the border effect and the lift-off effect is subtracted from the measured map that contains a crack information. After this correction, the amplitude and phase are used to analyse the crack. Figure 5.13 show an example of B_x map obtained before and after the data correction for the analysis of a linear defect with 8 mm of length. The experimental scan details are presented in Table 5.3.

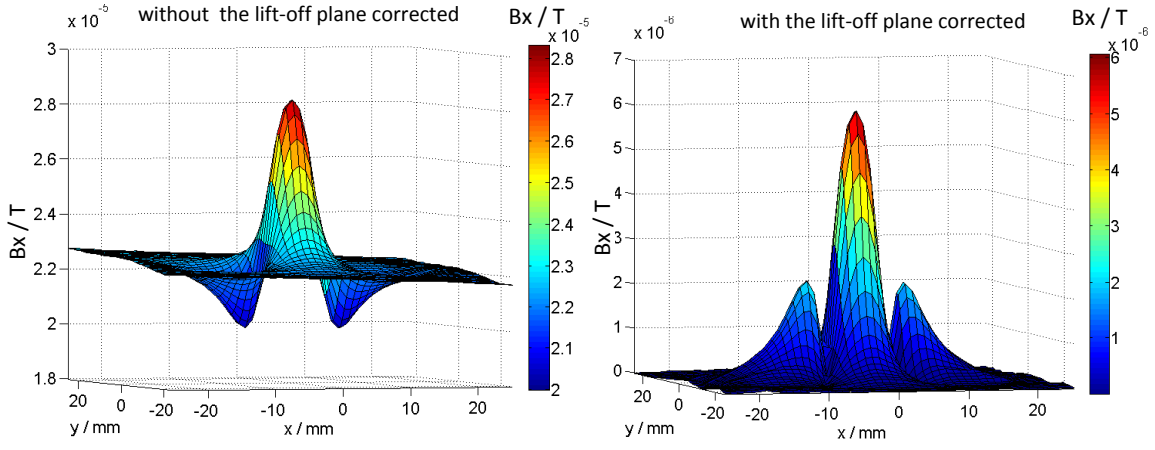

Figure 5.13: Experimental magnetic field B_x for 8 mm linear defect.

Table 5.3: Experimental scan details to illustrate the unwanted signal presented in the images.

Aluminium Plate	
Sample Size (mm)	$350 \times 250 \times 4$
Conductivity (S/m)	3.559×10^7
Defect Size (mm)	$8 \times 1 \times 1.5$
Probe	
Excitation Current (A)	0.2
Operating Frequency (kHz)	5
Scan	
Scan Step Size (mm)	1
Scan Map Size (mm)	50×50

In the case when the magnetic field B_y is measured, the presence of the excitation field is not expected and the measured field values should be zero. However, sometimes it may occur that the measured values along the boundary tend towards a value different from zero. This means that there is a misalignment of the field detector in relation to the imposed excitation currents, and some small fraction of the excitation field is detected. In this case, the measured data must be also corrected.

5.5 Defect Depth Study

In this subsection, a study concerning the perturbations in the magnetic field components (B_x and B_y) due to a linear defect having different depths was made in order to extract relevant information that allows the determination of the surface and sub-surface defect depth.

5.5.1 Characterisation of Surface Defect Depth

Surface linear defects are studied in this subsection. The magnetic field perturbation amplitude, phase and the signatures of B_y and B_x in the complex plane are analysed. Figure 5.14 depicts the plate under test. The sample presents seven artificial linear defects. Their only difference is the depth, equal to 3.5 mm for the deepest and 0.5 mm for the shallowest. The experimental tests were made in an aluminium alloy plate 1050 largely used in the metallic industries. Simulations were also performed in the COMSOL software to help to detect relevant features about defect depth.

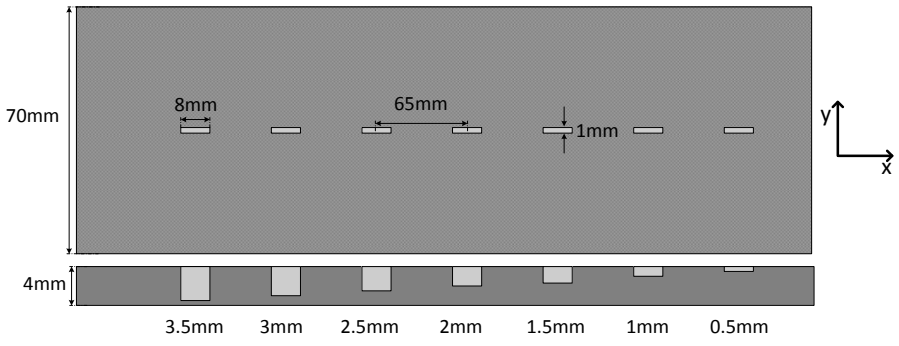

Figure 5.14: Seven rectangular surface cracks machined on an aluminum plate with 4 mm of thickness. The crack depth decreases from left (3.5 mm) to right.(0.5 mm).

5.5.1.A Simulation Work

Simulations were performed with a sine wave excitation frequency of 420 Hz that corresponds to a standard depth of penetration (δ) equal to 4 mm for this kind of aluminium alloy. The parameter d was used in the simulation to compute the different defect depths. The details of the simulations are shown in Table 5.4.

Table 5.4: Simulation model details to investigate the defect depth.

Aluminium Plate	
Sample Size (mm)	$190 \times 190 \times 4$
Conductivity (S/m)	3.559×10^7
Defect Size (mm)	$8 \times 1 \times d$
Planar Coil	
Surface current density in the invariant excitation field zone (A/m)	1250
Excitation frequency (Hz)	420
Scan	
Scan Map Size (mm)	$50 \times 50 \times 1$
Scan Step Size (mm)	0.5

Figure 5.15 depicts the simulated magnetic field perturbation of B_y for the different defect depths (d). Figure 5.16 depicts the simulated complex signatures obtained from B_y measurement for all defect depths (d).

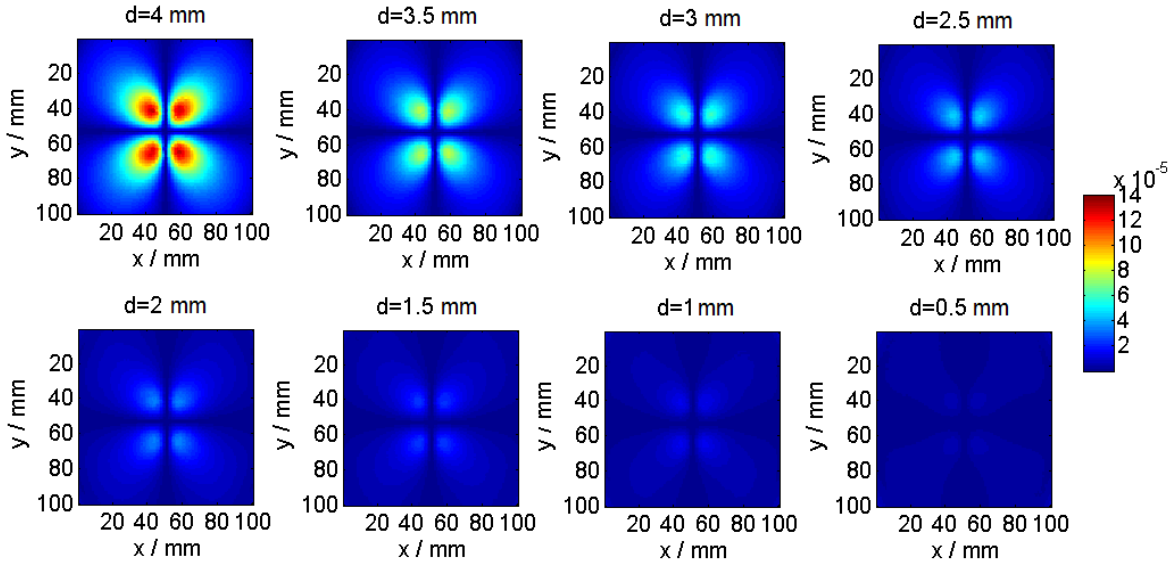

Figure 5.15: Simulated magnetic field amplitude perturbation of B_y (in tesla) for the surface defect with different depth (d).

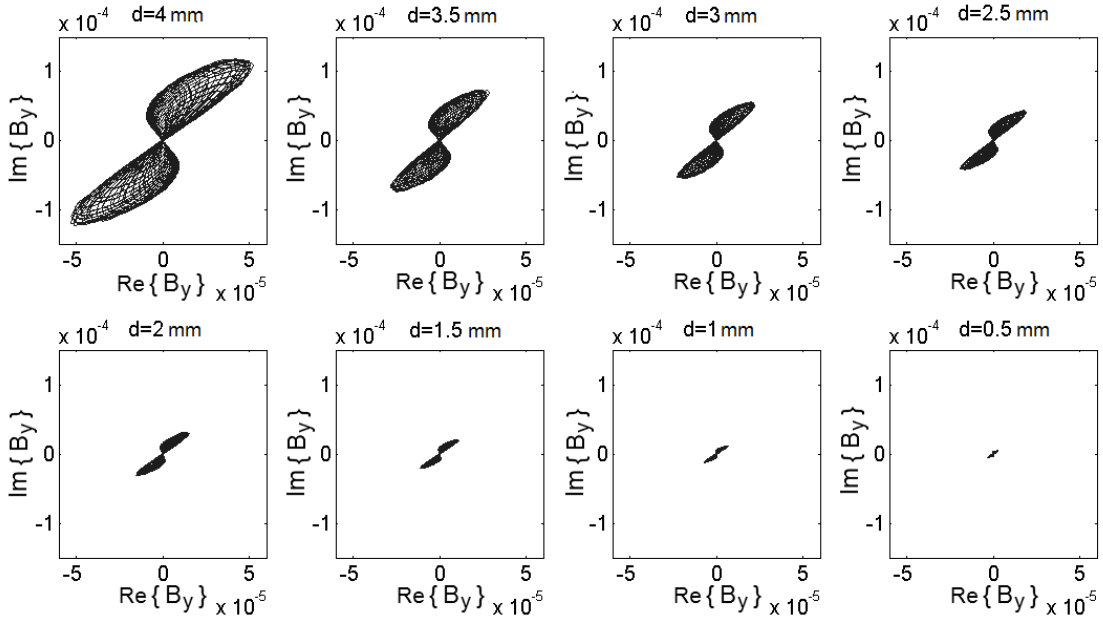

Figure 5.16: Simulated complex signatures for surface defect with different depth (d) using B_y component.

The results presented in Figure 5.15 show that the amplitude of the magnetic field perturbation B_y decreases with decreasing surface defect depth. These effect is due to less eddy current perturbation for defects near the surface plate. In other words, the majority of eddy current keep their original path for smaller surface defects, passing underneath the defect zone. Observing the complex signatures presented in Figure 5.16, it is possible to say that every signature has a similar angle of rotation for the different defect depths. The amplitude of the signatures decrease with decreasing surface defect depth. The same study and observations can be made for the magnetic field perturbation B_x. The results for B_x amplitudes and complex signatures are presented in Figure 5.17 and Figure 5.18, respectively.

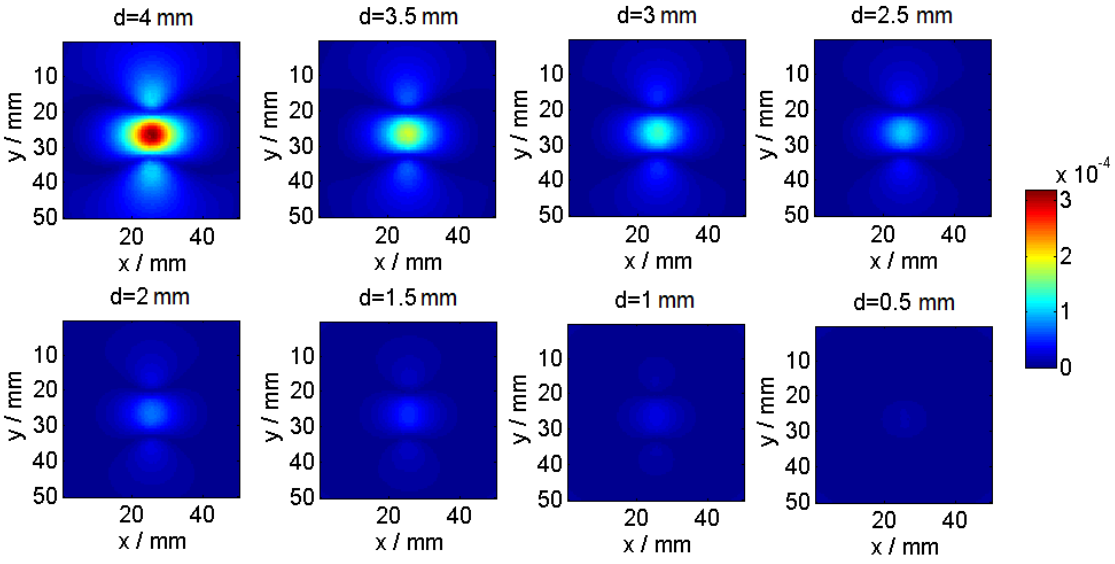

Figure 5.17: Simulated magnetic field amplitude perturbation of B_x (in tesla) for the surface defect with different depth (d).

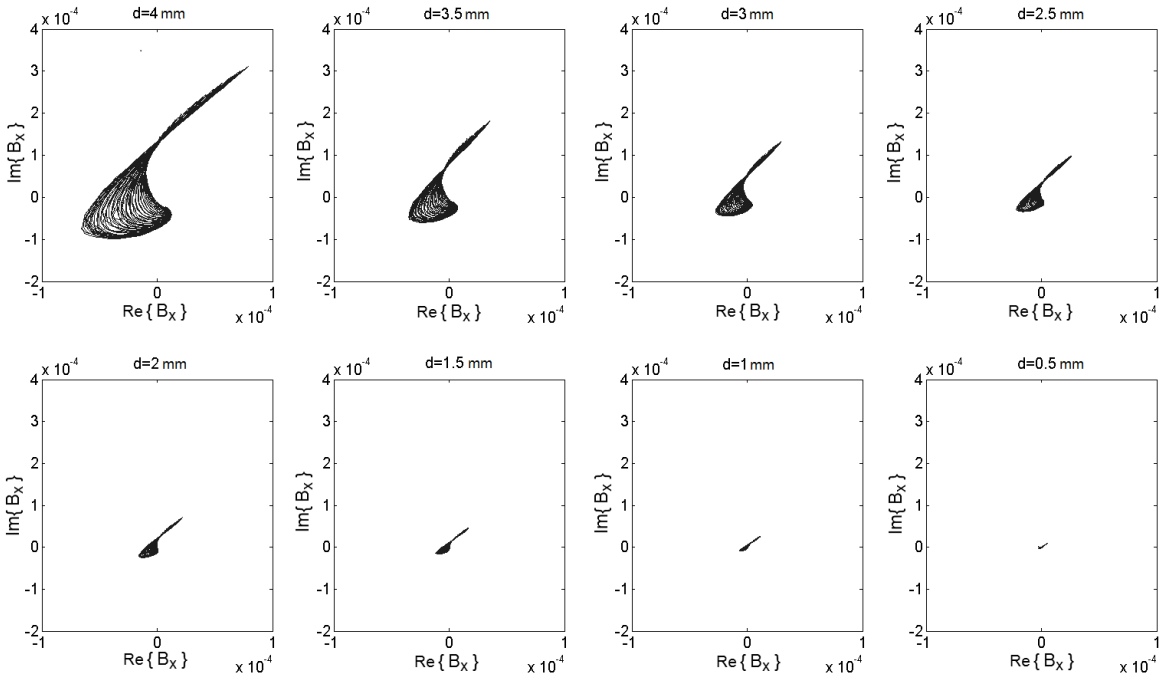

Figure 5.18: Simulated complex signatures for surface defects with different depths (d) using the B_x component.

5.5.1.B Experimental Work

In the experimental work, a rectangular surface containing all the cracks was scanned with the GMR sensing axes parallel and perpendicular to the current of the excitation coil measuring B_y and B_x components of the magnetic field, respectively. The eddy currents were induced perpendicularly to the defect's lines. The experimental work was performed with a excitation current of 200 mA and a excitation frequency of 500 Hz. At this frequency, the standard depth of penetration in the aluminium is $\delta = 3.78$ mm. Figure 5.19 and Figure 5.20 depict the amplitude map of the GMR output voltage obtained measuring the y component of the magnetic field (B_y) along the surface of the aluminium plate. The amplitude voltage decreases from left (3.5 mm defect depth) to right (0.5 mm defect depth). The baseline value of the complex amplitudes were subtracted from the data before presenting the results.

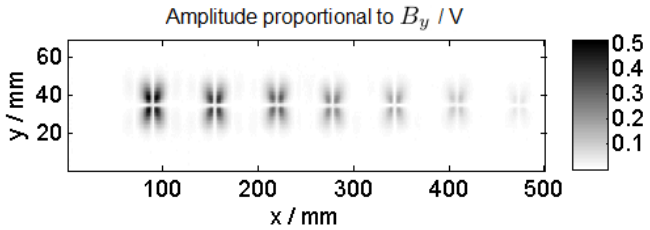

Figure 5.19: Two-dimension representation of the amplitude of the GMR output voltage when the plate was scanned measuring the B_y component of the magnetic field.

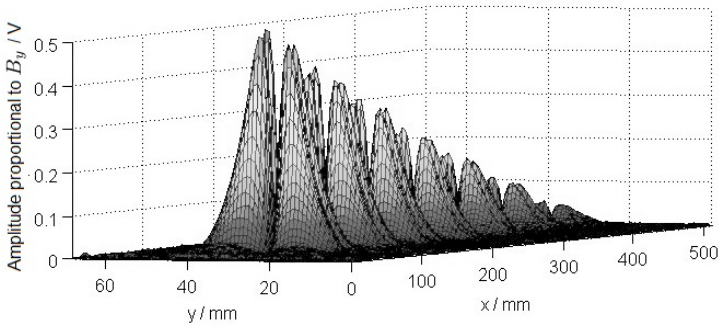

Figure 5.20: Map of amplitudes of the GMR sensor output when the plate was scanned measuring B_y component of the magnetic field.

Observing the results presented in Figure 5.20, the peak voltages are clearly correlated with the defect's depth. As previously observed in the simulation results, it is possible to say that the amplitude of the peaks decrease when the defect's depth also decreases. Hence, the determination of surface defect's depth can be obtained by analyze of this amplitude peak. However, it is important to show the evolution of the signals in the complex domain. Figure 5.21 depicts the measured complex signatures obtained by the GMR sensor over one of the edge of the defect for all defect depth (d).

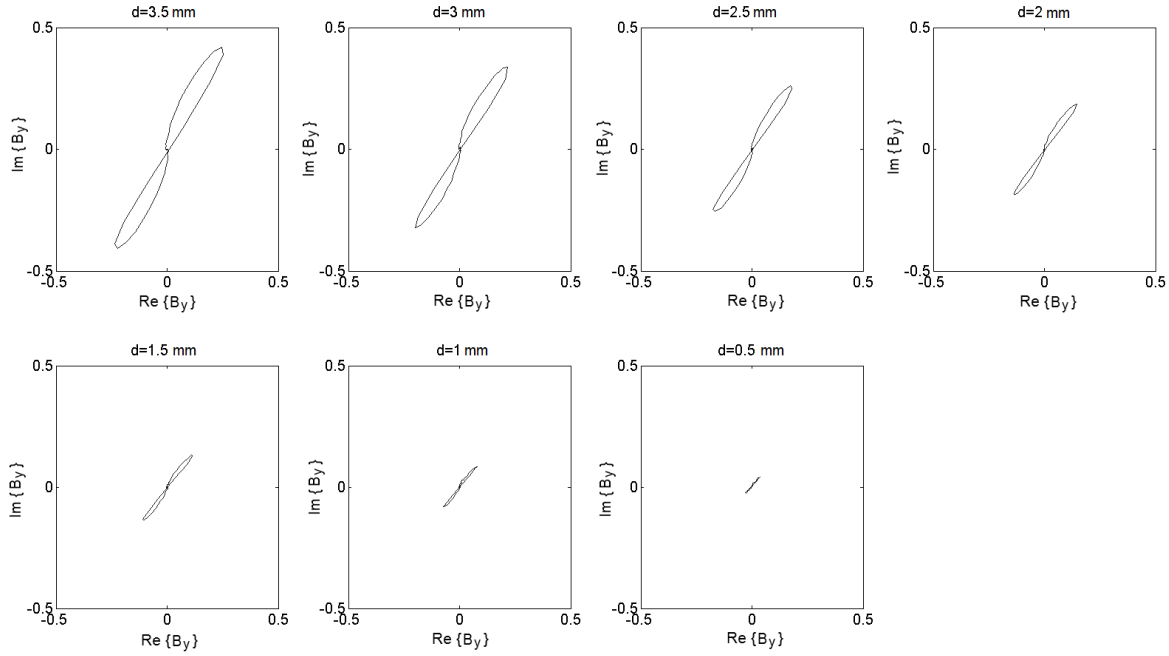

Figure 5.21: Measured complex signatures (from B_y) over one of the edge defect for the surface defect with different depth (d).

The results show that only the amplitude of the complex signature decreases when surface depth crack also decreases. The same experimental tests were made by Probe 2, with the GMR sensing axis measuring the B_x component. Due to the overlapping of the strong primary excitation field, the measurement of this component of the magnetic field is more problematic. It was necessary to subtract the constant magnetic field from the GMR sensor output in order to analyse the results correctly, as already explained in subsection 5.4.3. Figure 5.22 and Figure 5.23 depict the output

voltage B_x taken around the several defect after subtraction of the constant value of the magnetic field. The defect depth decreases from left (3.5 mm) to right (0.5 mm).

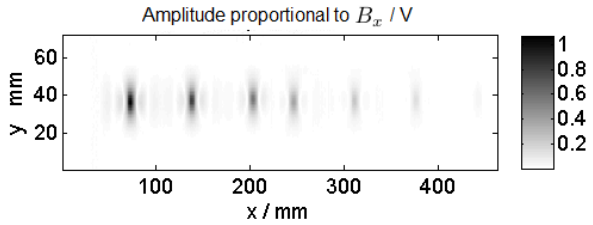

Figure 5.22: Two-dimension representation of the GMR voltage output when the plate was scanned measuring the B_x component of the magnetic field.

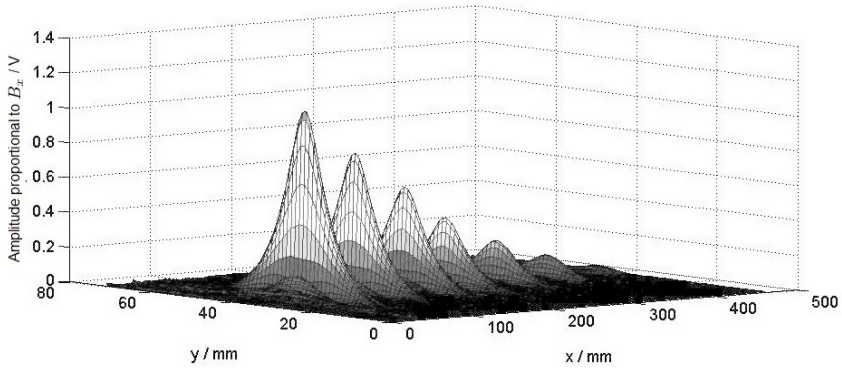

Figure 5.23: Map of amplitude of the GMR sensor output when the plate was scanned measuring the x component of the magnetic field (B_x).

Figure 5.24 depicts the complex signatures measured over cross lines in the defect center for all defect depths (d). The same observation made in B_y, can now be observed in B_x.

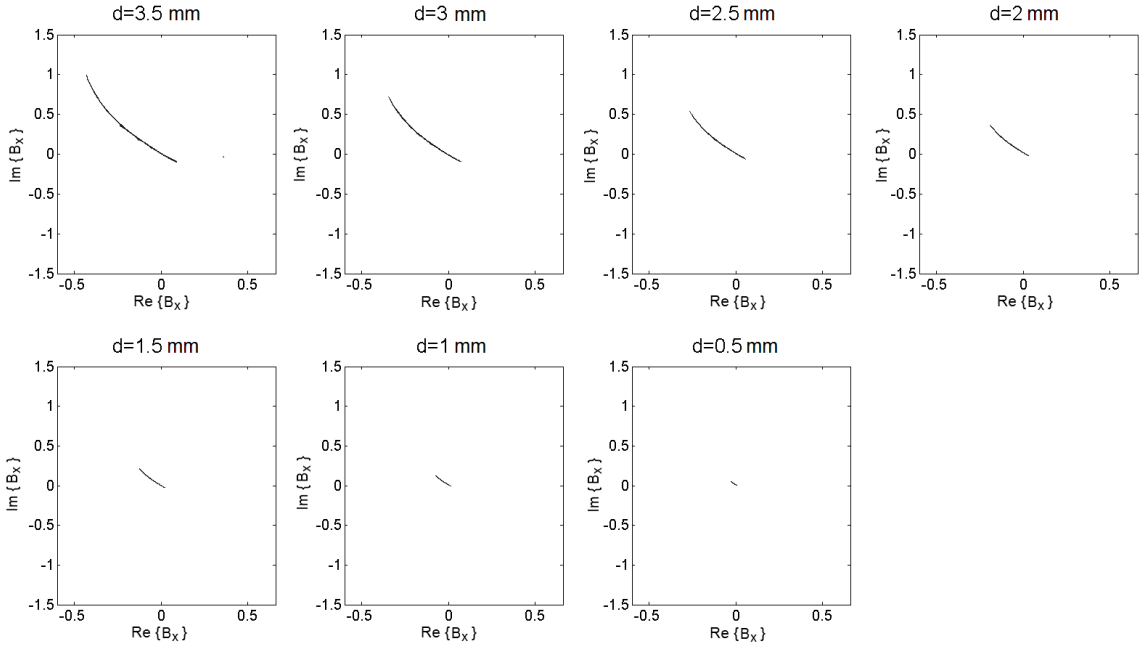

Figure 5.24: Measured complex signatures (from B_x) over one of the edge defect for the surface defect with different depth (d).

Comparing the results presented in Figure 5.20 for B_y and Figure 5.23 for B_x it is possible to observe that the perturbation field component B_x presents just one strong peak on each defect center, while the B_y component presents four peaks, two on each crack end. Taking the peak values of both field for each defect depth, two graphs with peak amplitude values were made and depicted in Figure 5.25. Each point represented in Figure 5.25(a) was obtained by the mean peak values of B_y for each defect depth. In Figure 5.25(b), the point represents the maximum peak value of B_x for each defect depth. It is obvious that the result obtained on the second case is more precise because the data presents one single peak on a smoother curve. Hence, the measured field B_x present a better option for the analysis of the depth of a defect.

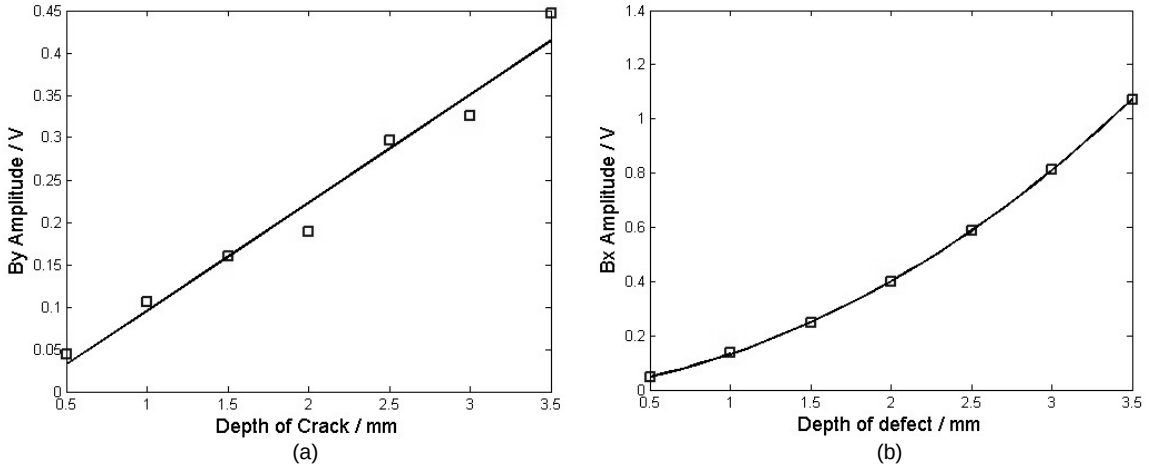

Figure 5.25: Amplitude of GMR output peak voltage for the seven cracks: (a)B_y component of the magnetic field.(b)B_x component of the magnetic field.

To investigate the defect depths on different operating frequency tests, all defects were scanned for a range of frequencies between 500 Hz to 10 kHz with fixed 225 mA excitation current. Analysing the sample for the deepest and the shallowest defect, Figure 5.26 represents the data obtained for one linear scan over the defects edge with 0.5 mm and 3.5 mm of depth using the probe that measures the B_y magnetic field component.

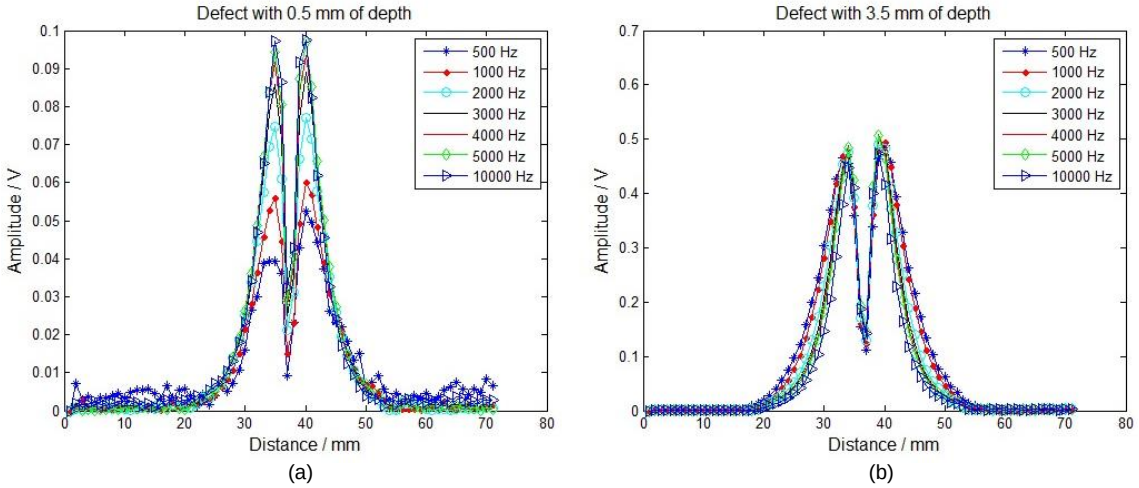

Figure 5.26: Amplitude of the GMR output signal that is proportional to the B_y component for a linear scan over two cracks: (a) Crack with 0.5 mm of depth (b) Crack with 3.5 mm of depth.

Observing Figure 5.26(a) the peaks amplitude increase with the excitation frequency. For small defects, this fact results from currents that circulate under the defect when low frequencies are used, but are constrained to circulate around the defect when the frequency increases. However, when the defect is deep, as presented in Figure 5.26(b), the peaks amplitude were almost independent from frequency because most of the currents near the edges of the defect are constrained to circulate only around the defect.

Figure 5.27 represents the data obtained with one linear scan over the defects center with 0.5 mm and 3.5 mm of depth using the probe that measure the B_x magnetic field component. In both cases, it is possible to observe that the peaks amplitude increases with the excitation frequency. Hence, in both cases, there are always currents that pass under the defect center. Hence, it's easy to say that to analyse the depth of a defect, the B_x component of the magnetic field is the better option.

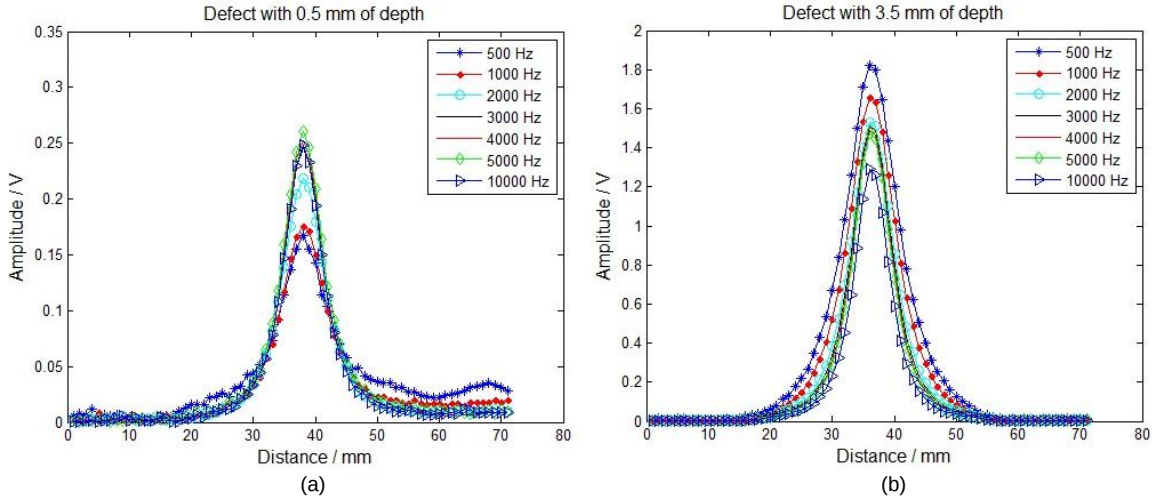

Figure 5.27: Amplitude of the GMR output signal that is proportional to the B_x component for a linear scan over two cracks: (a) Crack with 0.5 mm of depth (b) Crack with 3.5 mm of depth.

The next result was made only with the probe measuring the parallel magnetic field to the defect's lines because it is the best way to analyse the defect's depth. Figure 5.28 represents the curves of the peaks amplitudes of the B_x component at different frequencies for the seven defects.

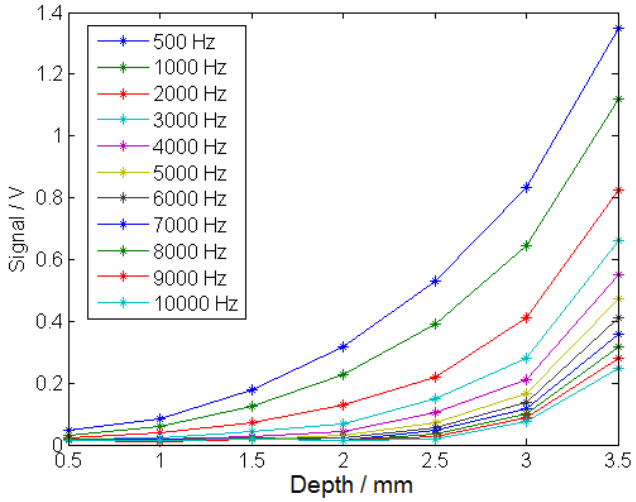

Figure 5.28: B_x Amplitude of GMR output peak voltage at several frequencies for the seven cracks.

The results clearly show that the peak voltages are correlated with the defect's depth and the operating frequency chosen. It is also possible to see that the defect depth curve increases exponentially with increasing surface defect depth. This effect is correlated with the currents that circulate under the defect center at different depths that also have an exponential decay (as already explained in Chapter 2, subsection 2.3.2).

5.5.1.C Conclusion on the Depth of Surface Defects

The results show that the amplitude of the magnetic field perturbation due to surface defects contains the main defect depth information for a fixed excitation current and frequency appropriate to induced eddy current along the plate depth. Comparing the results obtained from B_y and B_x amplitudes, it is possible to say that B_x amplitudes give a better defect depth estimation than B_y because this field perturbation presents one single peak at the defect center, while B_y presents four peaks at the edge defect. For surface defect depth analysis, the complex signatures don't add significant information about defect depth and only the amplitude of the signature changes with the defect depth. On the other hand, a range of operating frequencies can be useful for defect depth classification.

5.5.2 Characterisation of Sub-surface Defect Depth

Sub-surface defect depths are studied in this subsection. The magnetic field perturbation amplitude, phase and the signatures of B_y and B_x in the complex form are analysed. The experimental tests were made in the aluminium 1050 alloy plate already used to characterize surface defect depths. To remember, the sample plate has several linear defects with depths between 0.5 mm (d) and 3.5 mm and 8 mm of length. In that case, the sample was studied inside out as illustrated in Figure 5.29. Simu-

lations were performed with the COMSOL software on the same condition studied for surface defects.

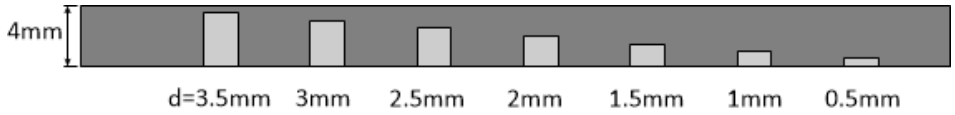

Figure 5.29: Plate with the cracks on the bottom. The inspection is performed on the top surface.

5.5.2.A Simulation Work

To investigate sub-surface defects in a 4 mm of thickness aluminium plate, simulations were performed with a sine wave excitation frequency of 420 Hz that corresponds to a standard depth of penetration equal to $\delta = 4$ mm. The simulated maps of magnetic field B_y and B_x of sub-surface defect depth were similar to the maps obtained for surface defect depth. The peak amplitudes of both magnetic field components decrease with decreasing sub-surface depth. However, significant changes on the complex signatures angle were obtained. Figure 5.30 depicts the complex signatures (from B_y) obtained crossing the edge of all sub-surface defect depth, while Figure 5.31 depicts the complex signatures (from B_x) obtained crossing the center of all sub-surface defect depth. In both cases, the results show that the phase of the signature changes when defect depth also changes. This feature can be easily used to classify sub-surface defect depth in a range of known geometry defect.

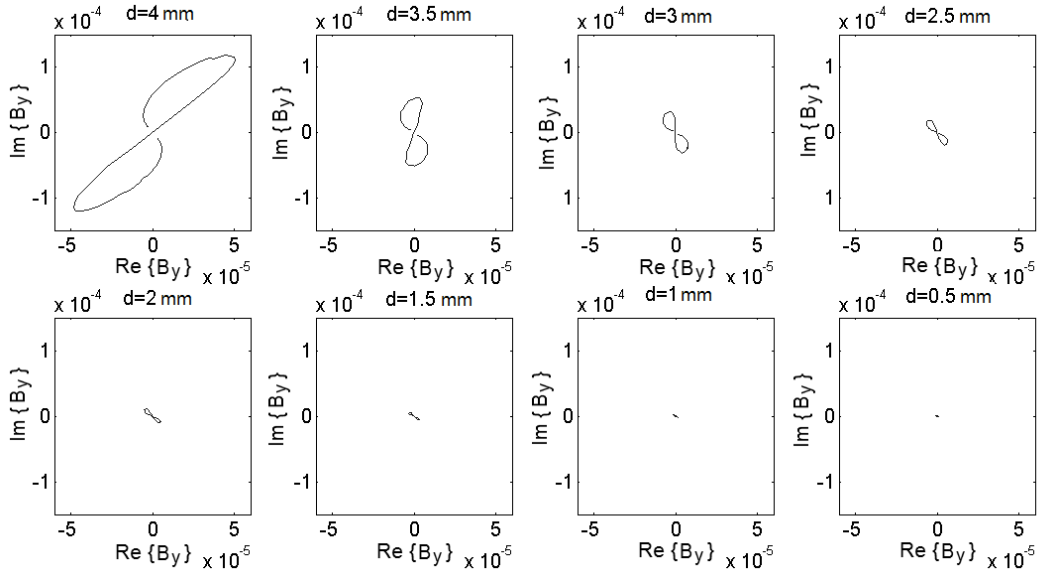

Figure 5.30: Simulated complex signatures for sub-surface defect with different depth (d) using B_y component.

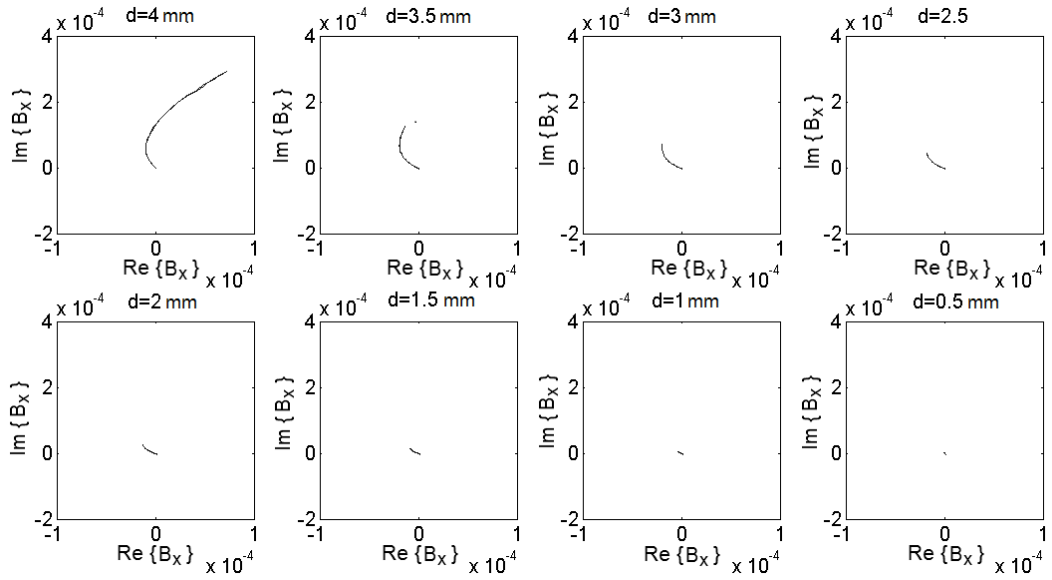

Figure 5.31: Simulated complex signatures for sub-surface defect with different depth (d) using B_x component.

5.5.2.B Experimental Work

To investigate the changes of the complex phase signatures due to defect depth in real samples, a rectangular surface containing the seven linear defects with different depths were scanned with GMR sensing axis parallel to the current of the excitation coil measuring B_y. Figure 5.32 depicts the complex signatures obtained when the GMR sensor is crossing over the defect edge for all defect depths (d).

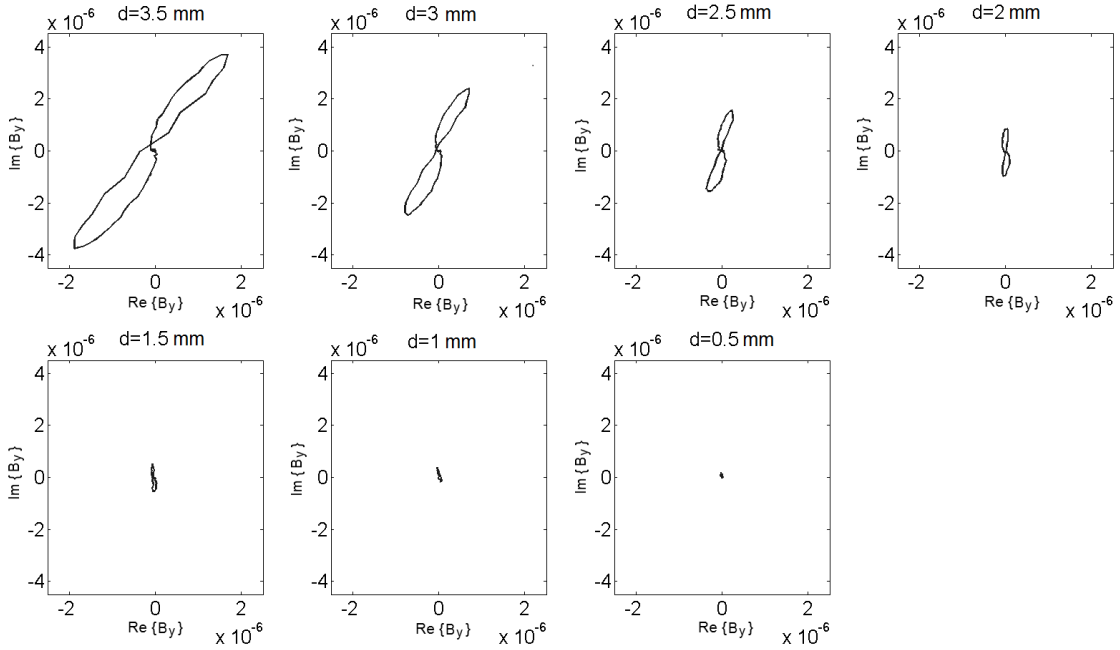

Figure 5.32: Experimental complex signatures for sub-surface defects with different depths (d) using B_y component.

5.5.2.C Conclusion on the Depth of Sub-surface Defects

The results show that the complex signatures of the magnetic field perturbation to defects contain important information about defect depth when sub-surface defect are analysed. For a fixed excitation frequency, the changes of the rotation angle of the complex signatures for the different defect depth can be a useful tool to identify defect characteristics of sub-surface defects.

5.6 Defect Profile Reconstruction

In this section, the inverse problem presented in the previous chapter will be used to obtain geometrical characteristics of the defects. Knowing the position of the defect, the scanning area should be such that all the magnetic field perturbations are included in this area. Subsection 5.6.1 presents a test of the inverse problem algorithm with experimental data for a linear defect. Subsection 5.6.2 presents the same linear defect test from multiple angle measurements. Three linear defects with different lengths (5, 8 and 12 mm) are analysed in subsection 5.6.3, using an automatic parameter selection for Tikhonov regularization. Several geometric defects machined on an aluminium plate are presented and analysed in subsection 5.6.4. For all experimental results, the complex mean values of the data measured around the defects was subtracted to the measured data to remove the primary magnetic field sensed by the GMR sensor, centring the map at the origin of the complex plane.

5.6.1 Experimental Data Test Using Tikhonov Regularization Algorithm

In this subsection, two scans were performed over an aluminium plate with 300 mm $\times$ 300 mm of size and a 20 mm long linear defect machined in the center of the metal. The scanned defect is depicted in Figure 5.33.

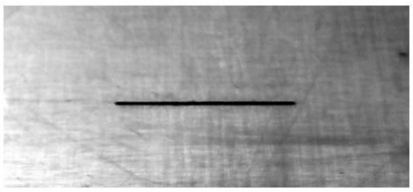

Figure 5.33: Photography of the machined linear defect with 20 mm of length.

The first scan was made measuring B_y with probe 1 and the second scan was made measuring B_x with probe 2. The details of the two scans are presented in Table 5.5.

Table 5.5: Experimental scan details.

Aluminium Plate	
Sample Size (mm)	$300 \times 300 \times 2$
Standard Conductivity (S/m)	3.7668×10^7
Defect Size (mm)	$20 \times 1 \times 2$
Probe	
Excitation current (A)	0.1
Excitation frequency (kHz)	5
Scan	
Scan Map Size (mm)	50×50
Scan Step Size (mm)	0.5

Figure 5.34 and Figure 5.35 present the amplitude and the phase obtained by the experimental setup with Probe 1 and Probe 2, respectively.

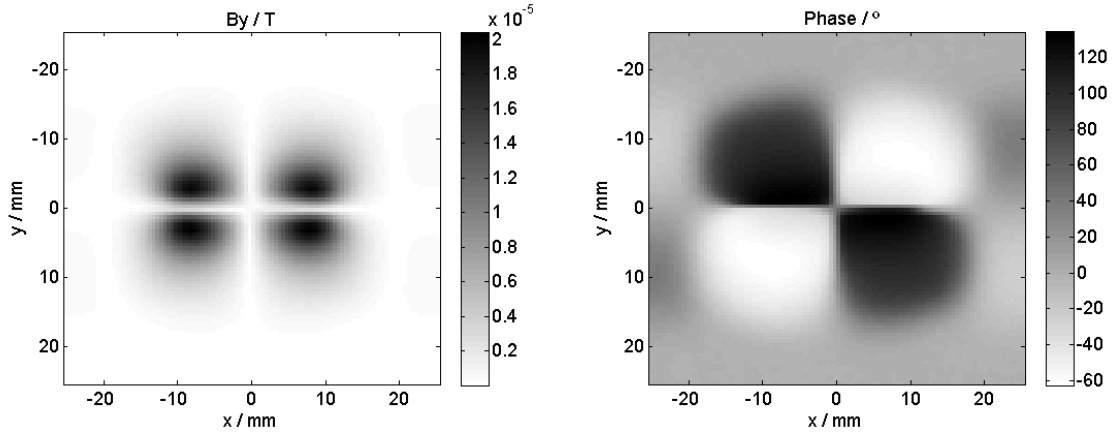

Figure 5.34: Representation of the scanned map from Probe 1. (a) Amplitude output of the GMR sensor converted in tesla; (b) Phase shift between the excitation signal and the GMR sensor signal in degrees.

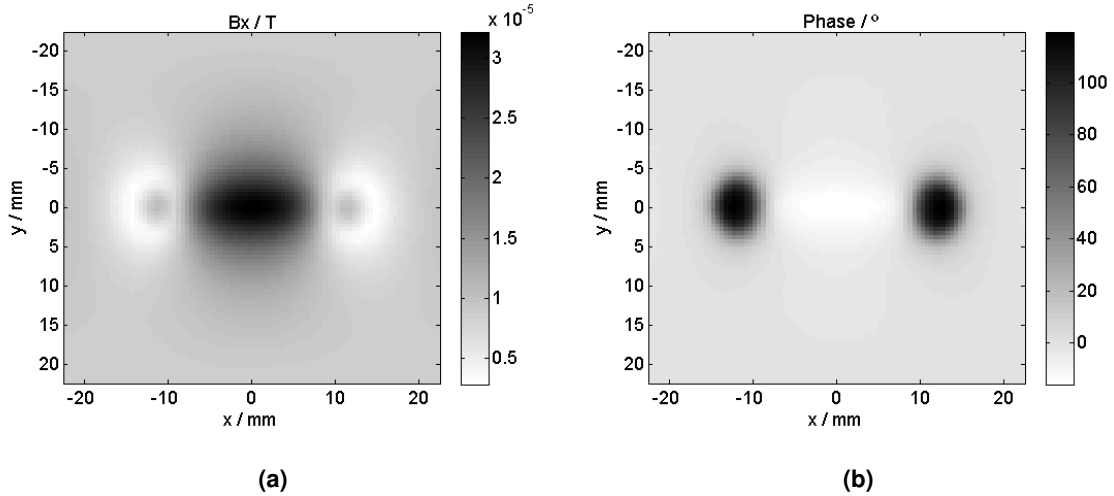

Figure 5.35: Representation of the scanned maps from Probe 2. (a) Amplitude output of the GMR sensor converted to tesla; (b) Phase shift between the excitation signal and the GMR sensor signal in degrees.

As already explained in section 5.4, the complex maps are obtained from amplitude and phase shift maps for each measured field component B_y and B_x. The complex surface including unwanted edge effects, lift-off effect and constant excitation field is removed in the complex maps. The real part of the obtained complex maps (B_y and B_x) are shown in Figure 5.36 and Figure 5.37. These two maps are the data used in the inverse problem algorithm to obtain the eddy current perturbation from B_y and B_x.

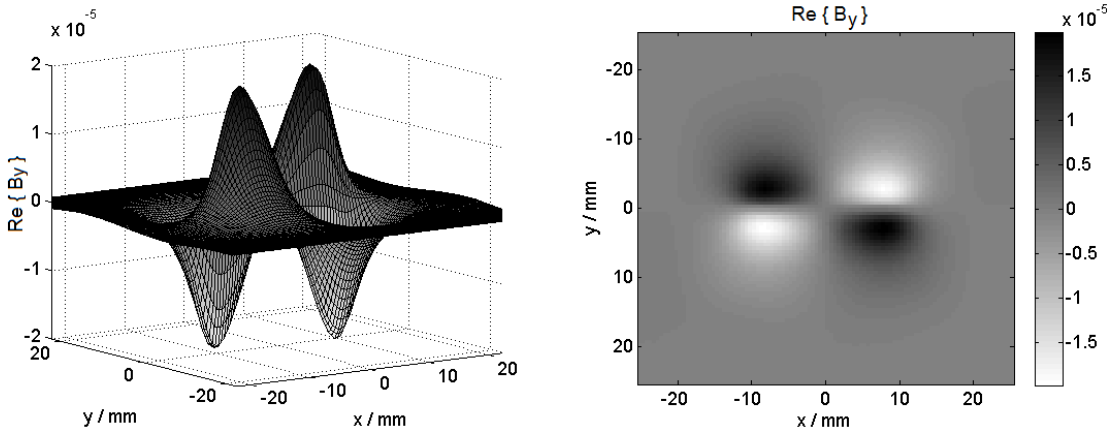

(a) **(b)**

Figure 5.36: Representation of the real part of the complex map from B_y. (a) Two-dimension view; (b) Top view.

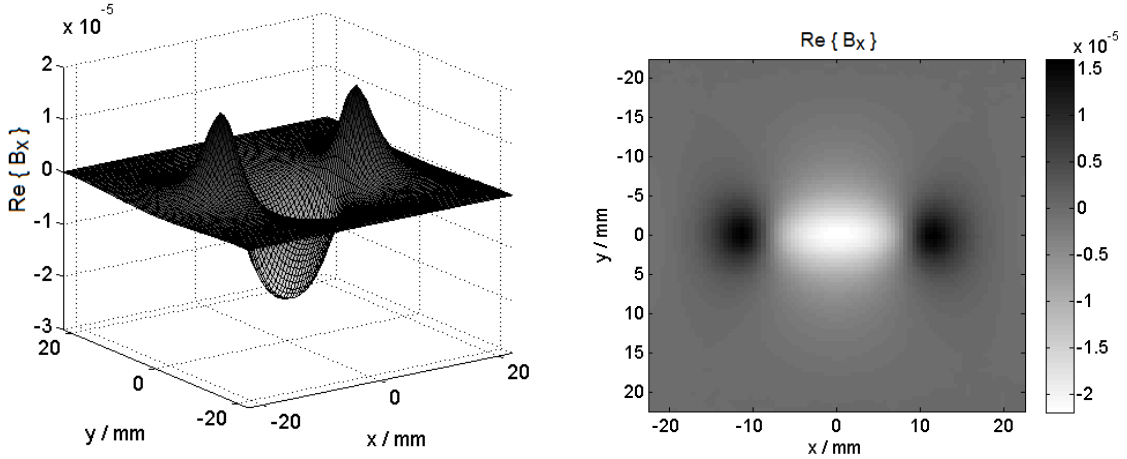

(a) **(b)**

Figure 5.37: Representation of the real part of the complex map from B_x. (a) Two-dimension view; (b) Top view.

The kernel maps b_y and b_x were calculated using the Biot-Savart law. The distance of 3.5 mm between GMR sensors and the surface on test was considered to compute the maps of b_y and b_y. To remember, these maps are used in the inverse problem algorithm, as solution of B_y and B_x inversions to obtain the dipolar eddy current perturbation J_d. The maps where calculated with 0.5 mm resolution and contained the information of the decomposition of the eddy current perturbation in unitary dipoles

current for B_y and B_x cases. Applying the inverse problem with Tikhonov regularization, Figure 5.38 and Figure 5.39 depict the reconstructed maps of the total eddy current density J for both cases. The maps were normalized to [0,1].

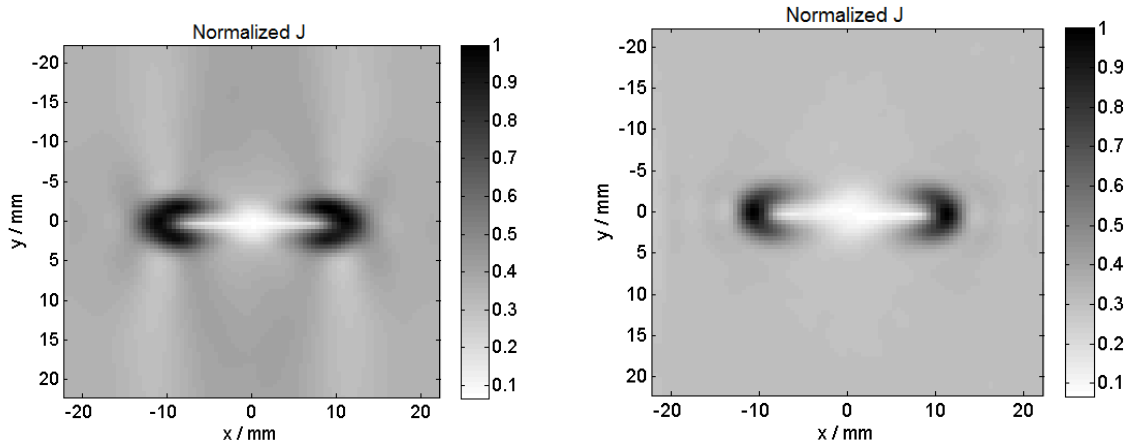

(a) **(b)**

Figure 5.38: Representation of the total eddy current density map obtained by inverse problem with Tikhonov regularization. (a) Normalized J obtained from the B_y component; (b) Normalized J obtained from the B_x component.

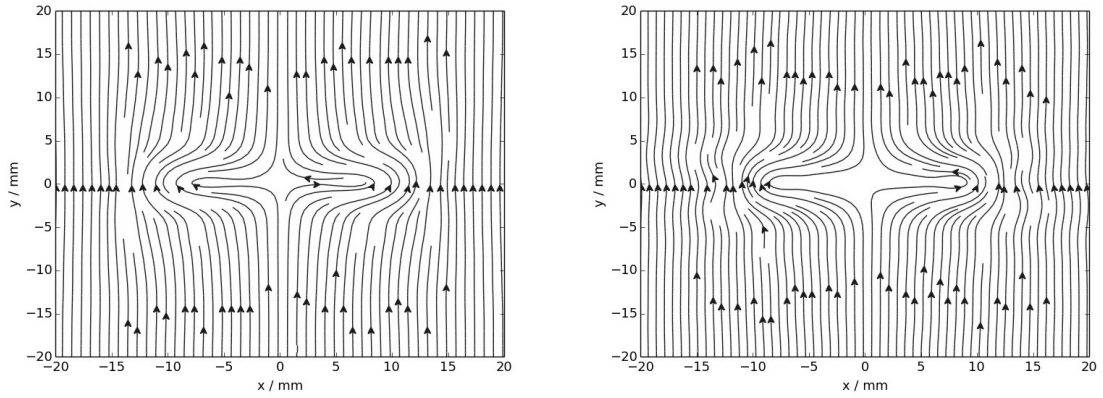

(a) **(b)**

Figure 5.39: Representation of the total eddy current lines obtained by inverse problem with Tikhonov regularization. (a) Currrent lines of J from B_y; (b) Current lines of J from B_x.

As expected, the inversion of experimental maps of B_x or B_y to J presents equivalent results that contain relevant information about the geometric profile of the crack.

5.6.2 Characterization of a Linear Defect From Multiple Angle Measurements Using Total Variation Regularization Algorithm

This experimental test was performed with the GMR sensing axis parallel to the current of the excitation coil (Probe 1). This test allows studying the magnetic field obtained with different angles of the GMR sensing axis in relation to a defect orientation. In this work, the angle between the y direction of a linear defect and the sensing axis of the GMR sensor is the angle α present in the next result, as demonstrated in Figure 5.40. The experimental results were obtained by scanning an aluminum plate with a linear machined defect with 20 mm length at a set of 6 rotation angles α, from 0 to 90 degrees with 18 degrees steps.

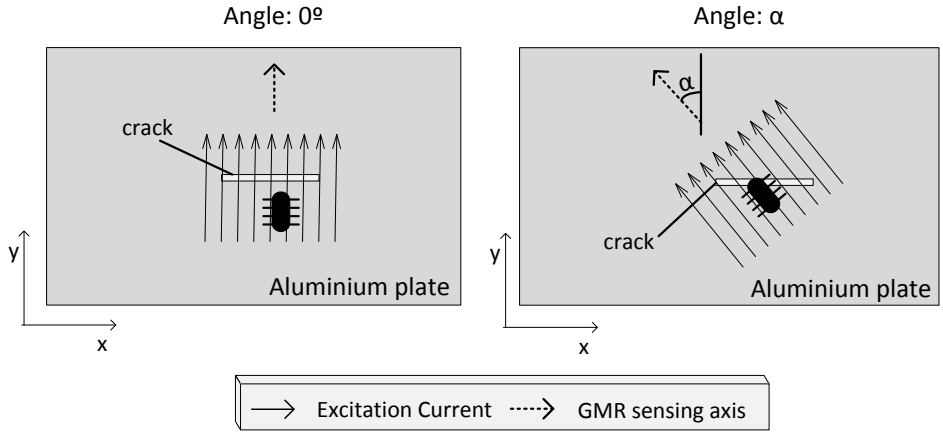

Figure 5.40: Visual representation of the angle α (between GMR sensing axis and y axis).

The details of the experimental test made are presented in Table 5.6.

Table 5.6: Experimental scans details.

Aluminium Plate	
Sample Size (mm)	$300 \times 300 \times 2$
Standard Conductivity (S/m)	3.7668×10^7
Defect Size (mm)	$20 \times 1 \times 2$
Probe	
Excitation current (A)	0.1
Excitation frequency (kHz)	5
Scan	
Scan Map Size (mm)	50×50
Scan Step Size (mm)	1

Figure 5.41 depicts the magnetic field obtained for 0, 18, 36, 54, 72 and 90 degrees. The scanned area was such that it covers all the perturbations of the magnetic field present in the proximity of the defect. Figure 5.42 depicts the maps of the phase shift between the excitation signal and the GMR sensor signal.

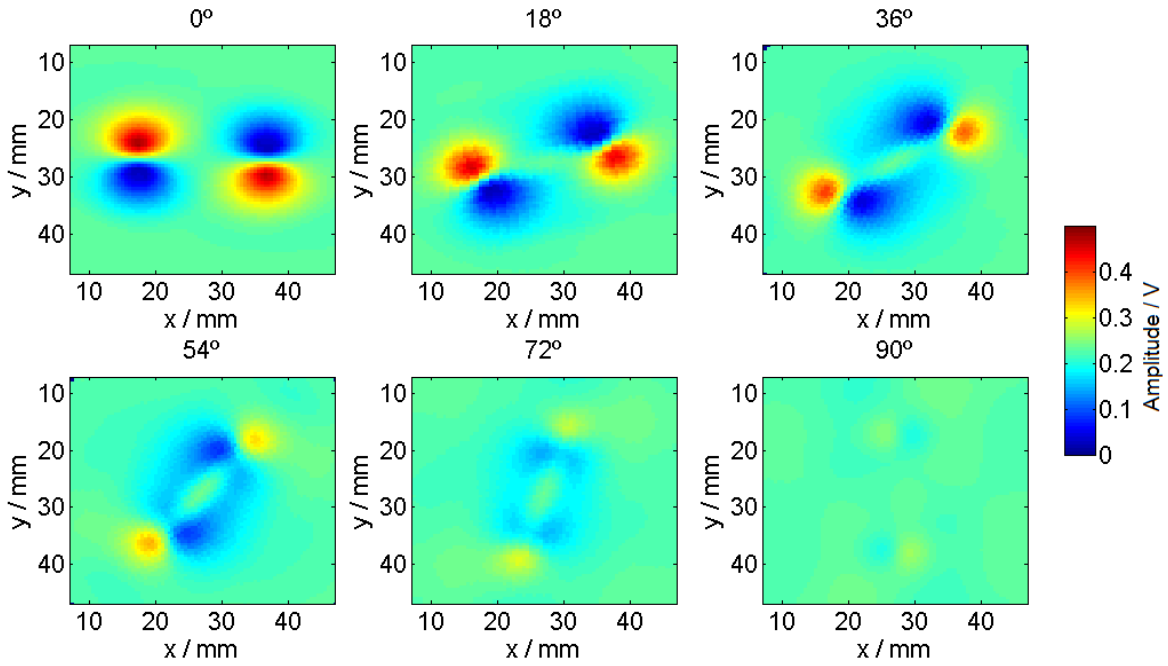

Figure 5.41: Magnetic field amplitude maps obtained by GMR output sensor for several angles.

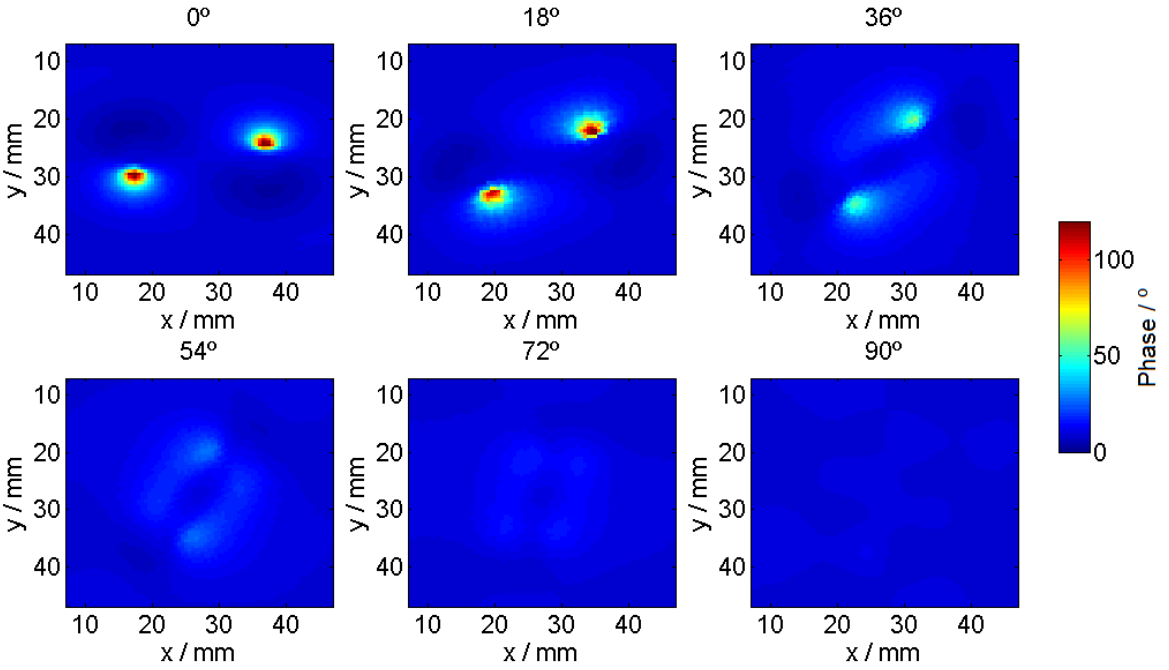

Figure 5.42: Map representation of the phase shift between the excitation signal and the GMR sensor signal (in degrees).

Considering the sensitivity of the GMR sensor equal to 3.6V/mT per V of the power supply, the maps of amplitude were converted to tesla. The complex maps were obtained by combining the amplitude and the phase shift maps for each case.

Figure 5.43 depicts the normalized eddy current densities obtained by the inverse problem algorithm with total variation regularization for the 6 rotation angles.

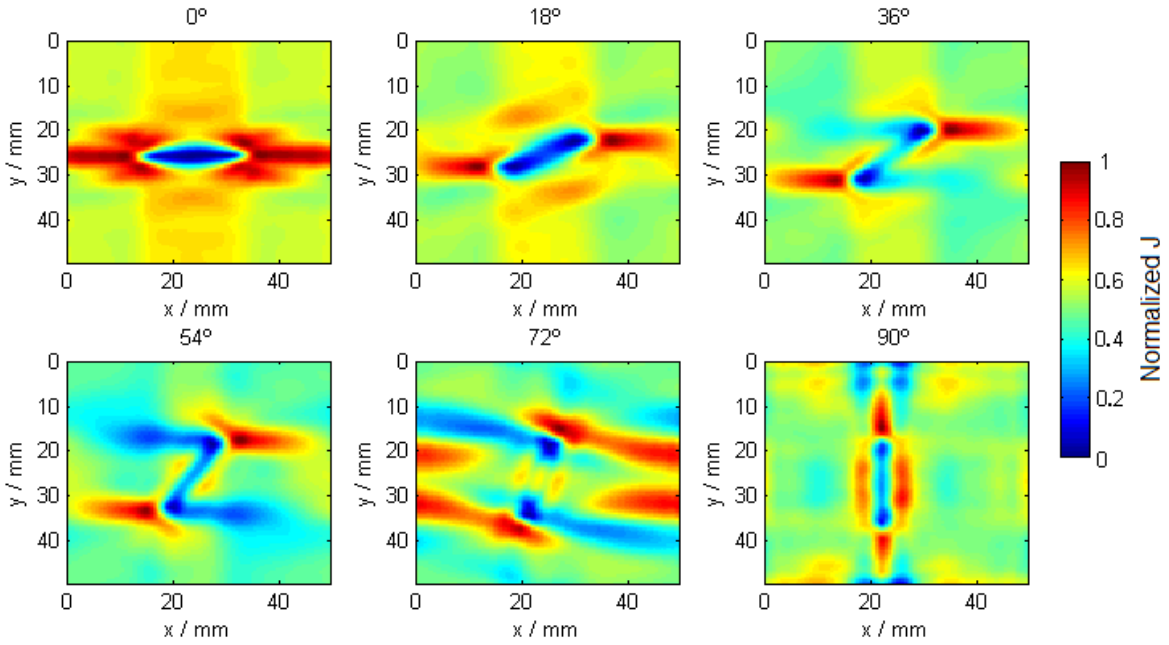

Figure 5.43: Normalized eddy current densities obtained for the 6 rotation angles.

The normalized eddy current density maps presented in Figure 5.43 show relevant information about the geometric profile of the crack. However, it is possible to say that the probe rotation method is slow due to the requirement of several scans. All density maps were joined and Figure 5.44 was obtained by vector summing all the current densities after rotating the current densities to the same angle.

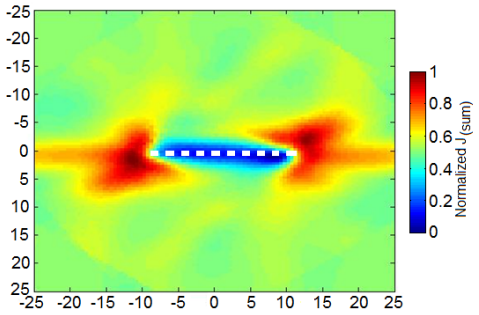

Figure 5.44: Result obtained by the sum of EC densities.

The normalized image of the sum of all eddy current densities shows that it contains more information about the geometric profile of the crack when compared with only one eddy current density map. However, small rotation errors were detected in the image due to the mechanical misalignment of the probe when the probe was measuring the magnetic field. A dashed white line was added to the image to show the real size of the crack.

5.6.3 Tikhonov Regularization with Automatic Parameter Selection

A proper choice of the regularization parameter value μ is essential for the success of the inversion with regularization method. In some cases, the optimal regularization parameter value is estimated from a prescribed energy or discrepancy that corresponds to the true image. In our case, no information regarding the true image of the eddy current distribution in the plate is known because it depends on the characteristics of the cracks. For our case, alternative methods are required to find automatically an adequate regularization parameter value μ to keep automatically a stable solution in the inversion process. In this study, the parameter μ was obtained automatically from two different methods. The advantages and disadvantages of the two methods are discussed.

The first method is called logarithmic energy derivative and is performed by the determined signal energy E of the regularized solutions in the frequency domain. The choice of the regularization parameter value μ is based on the variation of the relative energy of the estimated image as a function of a set of the regularization parameter μ. The mean signal energy E of the regularized solutions in the frequency domain can be obtained by:

$$E(\mu) = ||\hat{J}_d^{\mu}||^2 = \frac{1}{N_x N_y} \sum_{i=1}^{N_y} \sum_{j=1}^{N_x} |\hat{J}_d^{\mu}(i,j)|^2 \quad , \tag{5.11}$$

where the $\hat{}$ represents the data in the frequency domain, $\hat{J}_d$ is the dipolar perturbation current, μ is the regularization parameter, N_x and N_y are the number of rows and columns in the spatial matrix of the image.

The second method uses the L-curve criterion and this method is based on the energy of the estimated image from the inverse process as a function of the discrepancy between the estimated and the measured results.

The mean discrepancy is defines as

$$\varepsilon(\mu) = ||\hat{b^{\mu}} \hat{J}_d^{\mu} - \hat{B}||^2 = \frac{1}{N_x N_y} \sum_{i=1}^{N_y} \sum_{j=1}^{N_x} |\hat{b^{\mu}}(i,j) \hat{J}_d^{\mu}(i,j) - \hat{B}(i,j)|^2 \quad , \tag{5.12}$$

where the $\hat{}$ represents the data in the frequency domain, $\hat{B}$ and $\hat{b}$ can be represented as function of x, y or z, $\hat{J}_d$ is the dipolar perturbation current, μ is the regularization parameter, N_x and N_y are the number of rows and columns in the spatial matrix of the image.

When the energy $E(\mu)$ is represented graphically against the discrepancy $\varepsilon(\mu)$ for a set of regularization parameters μ, the resulting curve presents a characteristic L-shape and the best parameter value corresponds to the knee point of the curve. L-curves can be computed and the minimum radius of curvature of the L-curve can be selected automatically as the optimal regularization parameter μ.

In order to test the automatic regularization parameter selection using the two method on experimental data, measurements of the magnetic field component B_x were obtained over a 4 mm thick aluminium plate containing three linear surface defects with different lengths (l = 12 mm, 8 mm and 5 mm). Figure 5.45 depicts the representation of the sample plate under inspection. The three defects have the same width (w) equal to 1 mm and the same depth (d) equal to 3.0 mm.

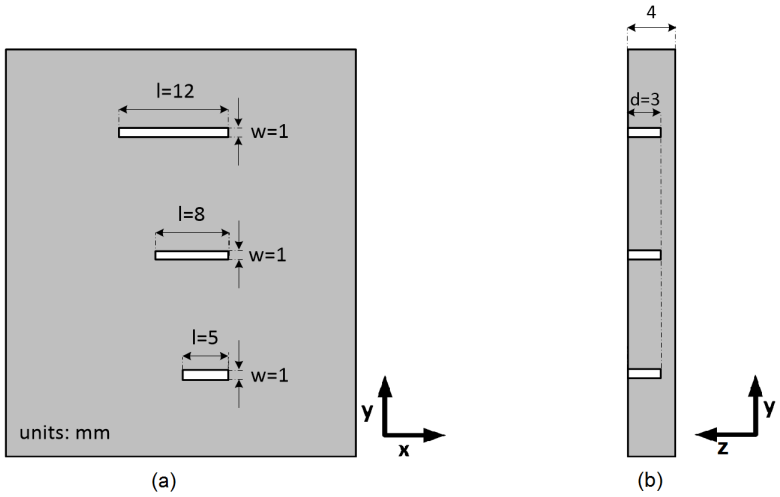

Figure 5.45: Representation of the inspected plate that contains three linear defects with different lengths (l = 12.0 mm, 8.0 mm and 5.0 mm): (a) Top view; (b) Profile view

The positioning system moved the probe with spatial resolution of 0.2 mm on the surface of the test specimen in a region of 50×50 mm around each defect. Figure 5.46 and Figure 5.47 depict the obtained maps of the output amplitudes and phase differences between the excitation current and the sensor output voltage for each scanned defect. Each one of these maps was kept in a matrix form with size ($N_x \times N_y$) = (250×250).

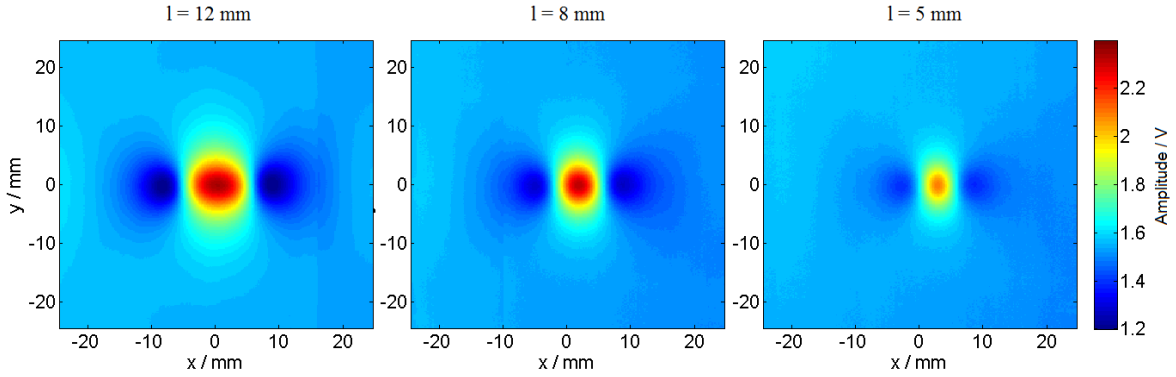

Figure 5.46: Representation of the sensor output amplitude maps (in V) for the three linear defects.

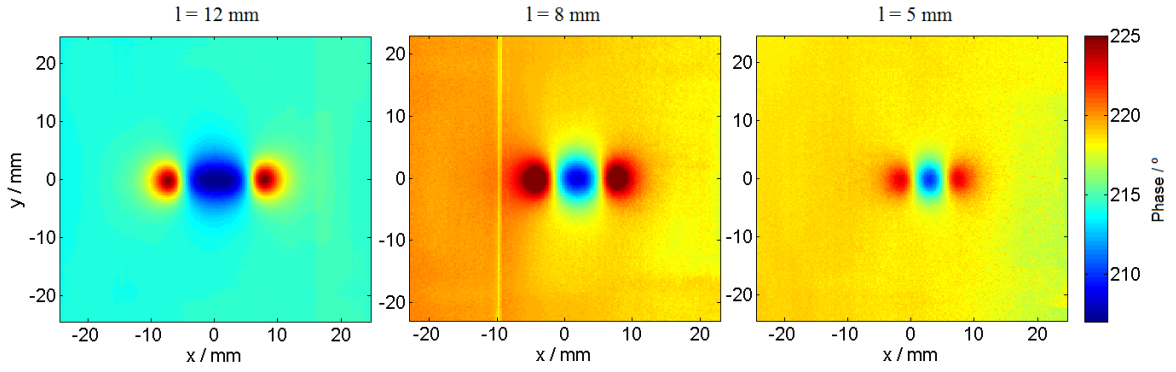

Figure 5.47: Representation of the phase shift maps (in degrees) between the excitation signal and the sensor signal for the three linear defect cases.

The output amplitude maps were converted to tesla considering the sensitivity of the GMR sensor equal to 3.6 V/mT per V of the power supply. The complex map was obtained by combining the amplitude and the phase shift maps. The first method to find the best regularization parameter was applied, that is, the data were inverted using Tikhonov regularization with logarithmic energy derivative criterion. The energy functions for the dipolar current densities of the three defects are depicted in Figure 5.48 (a) and the logarithmic derivatives curves of the energy are depicted in Figure 5.48 (b).

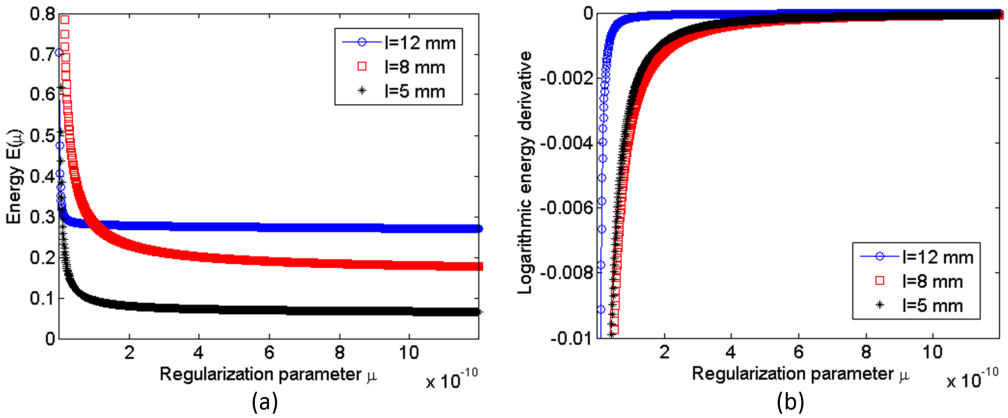

Figure 5.48: Energy curves of the regularized solution obtained for the three defects, as a function of the parameter μ; (a) Signal energy; (b) Logarithmic energy derivative.

We noticed that we had an acceptable solution when the relative energy change for a variation of μ was equal to 0.0001. Hence,the first method uses a threshold value of 0.0001 of the relative energy of determine the regularization parameter μ. This criterion of energy stabilization was applied and the values of $\mu_1 = 1.41 \times 10^{-10}$, $\mu_2 = 9.45 \times 10^{-10}$ and $\mu_3 = 7.98 \times 10^{-10}$ respectively to the cracks with lengths equal to 12, 8 and 5 mm were obtained. Figure 5.49 depicts the reconstructed maps of the total eddy current density (J) for the three cracks with different lengths (l). The maps were normalized to [0,1]. The spatial eddy current lines marked in blue were added in the image to help the visualization of the current paths. The true position of the linear cracks was added in the images with a red colour dashed line for better visualization. It is possible to observe in Figure 5.49 that the distance between the maximum points of the current density approximately matches the length of the cracks.

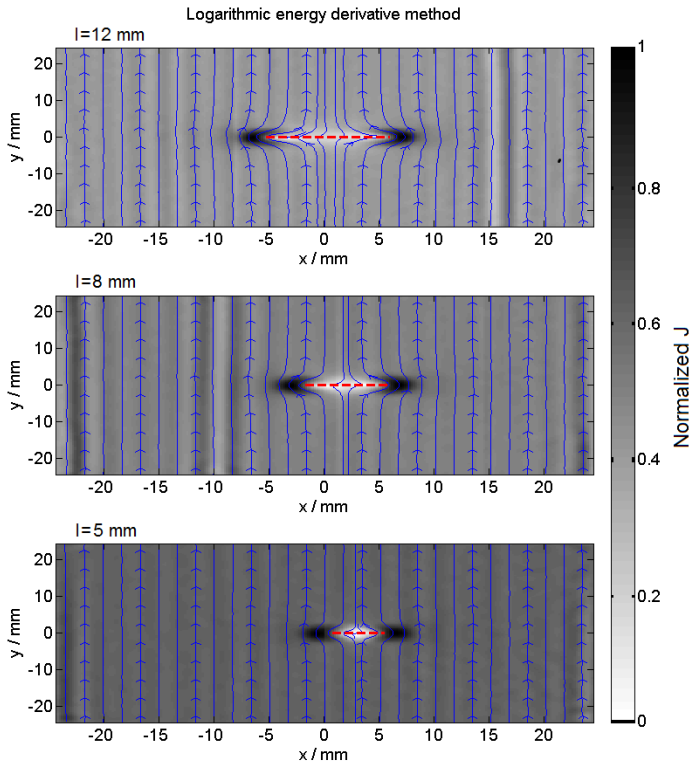

Figure 5.49: Reconstructed maps of the eddy current density (J) obtained using the logarithmic energy derivative method for the three defects with lengths of 5, 8, and 12 mm.

From the second method, the L-curves for the three defects were obtained and are representedin Figure 5.50. When the parameter value increases, the energy always decreases. The points in the L-curve corners are very close to each other. The regularization parameters were obtained automatically by finding the minimum radius of the circle through 3 points consecutive along the L-curve. The optimal parameter values μ for the cracks lengths of 5, 8 and 12 mm (obtained by the L-curve plot) are $\mu_1 = 2.06 \times 10^{-9}$, $\mu_2 = 6.1 \times 10^{-9}$ and $\mu_3 = 5.12 \times 10^{-9}$, respectively.

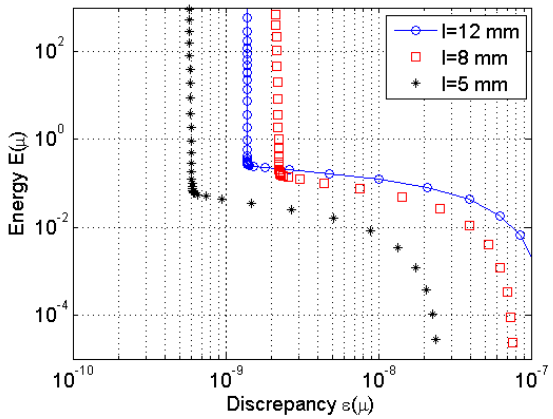

Figure 5.50: L-curves obtained for the three defects with lengths of 5, 8 and 12 mm.

Figure 5.51 depicts the reconstructed map of the eddy current density (J) using the L-curve criterion for the three cracks.

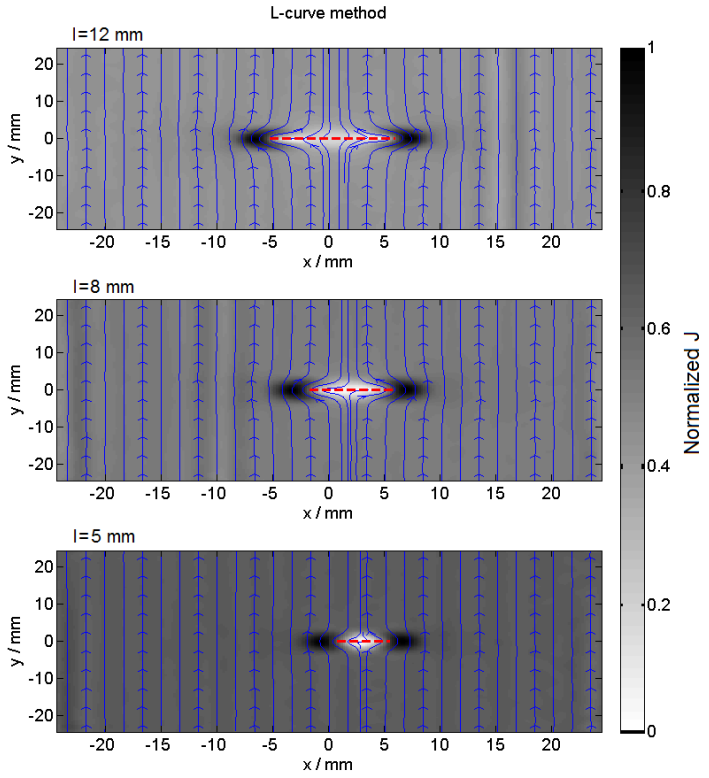

Figure 5.51: Reconstructed maps of the eddy current density (J) obtained using the L-curve method for the three defects with lengths of 12, 8 and 5 mm.

In the second method, it is also possible to observe in Figure 5.51 that the distance between the maximum points of current density approximately matches the length of the cracks. Hence, it is possible to say that both methods are able to find an adequate regularization parameter value μ to return automatically a stable solution in the inversion process. Despite the chosen regularization parameters μ being different from both methods, the 2D images of the obtained eddy current density show similar pattern. This can be explained by considering the L-curves shown in Figure 5.50, where a set of points in the corner of the curve are very close to each other. In fact there is a range of parameter values that was estimated as $\mu \in [9.3 \times 10^{-11} : 8.9 \times 10^{-9}]$ in the knee region, where the energy of the reconstructed currents is stable. Comparing this range of values with the obtained optimal regularization parameter values by the logarithmic derivative method, it is possible to say that the parameters are included in the same range. Comparing the computation time of both methods, the logarithmic energy derivative method is faster than the L-curve method due to less computations needed to find the optimal regularization parameter. However, this difference in computation time is not significant if they are used in a complete automated ECT scanner using the inversion process.

5.6.4 Characterization of Five Geometrical Defects Using Tikhonov Regularization Algorithm

In this section, five different defects machined on an aluminium plate were scanned from the measurement setup. All defects are presented in Figure 5.52. The experimental tests were performed with GMR sensing axis perpendicular to the current of the excitation coil measuring B_x component of the magnetic field. The inverse problem algorithm with Tikhonov regularization was applied to the data obtained experimentally. The spatial eddy current density and the normalized eddy current density were obtained by this algorithm.

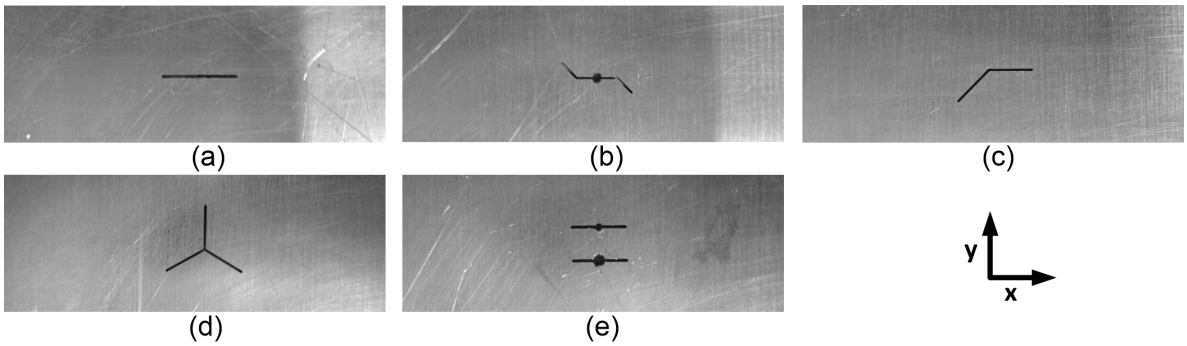

Figure 5.52: Photographs of the five defects on analysis. (a) Linear defect machined with 10 mm of length. (b) Zigzag defect machined with 10 mm of length. (c) Curved defect machined with 10 mm of length. (d) Star defect machined with 5 mm of length per branch.(e) Double linear defect with 5 mm of length.

The experimental results were obtained imposing a sinusoidal current with 200 mA of amplitude and 5 kHz of operating frequency to the planar coil. The uniform current distribution was forced in the y-axis direction. The details of the scan are illustrated in Table 5.7.

Table 5.7: Experimental scans details.

Aluminium Plate	
Sample Size (mm)	$250 \times 250 \times 1$
Conductivity (S/m)	3.559×10^7
Probe	
Excitation current (A)	0.2
Excitation frequency (kHz)	5
Scan	
Scan Map Size (mm)	50×50
Scan Step Size (mm)	0.2

The results obtained for the B_x component of the magnetic field, amplitude and phase shift between excitation signal and output sensor signal, are depicted in Figure 5.53 and Figure 5.54.

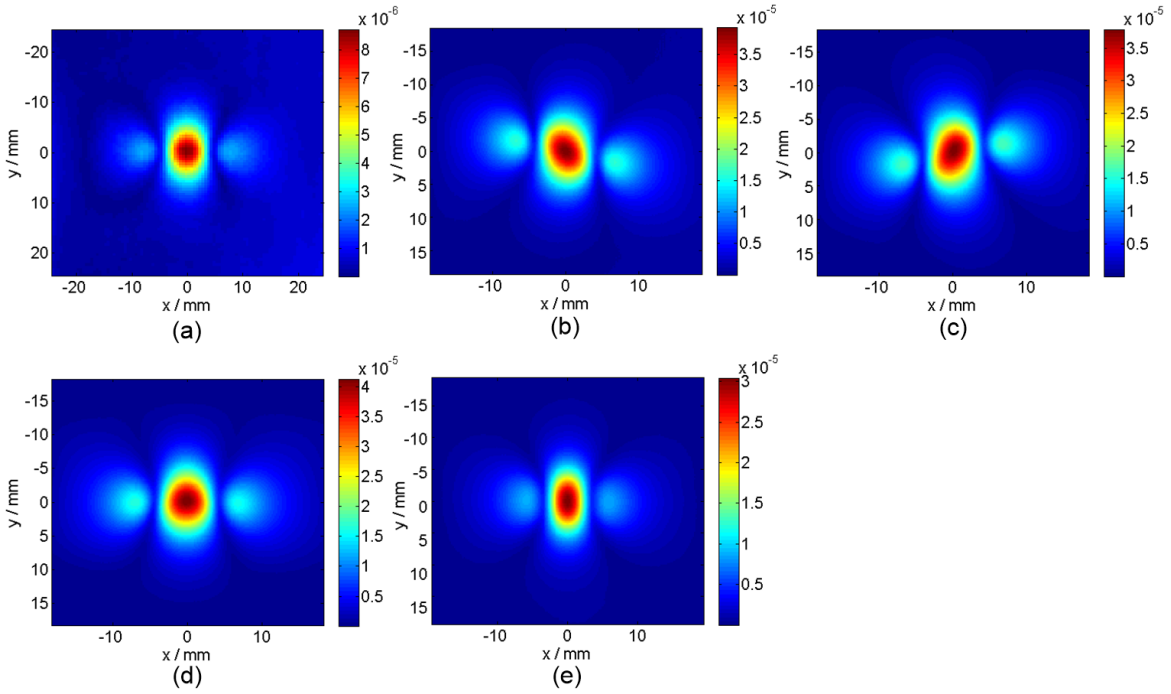

Figure 5.53: 2D maps of the GMR output sensor for each crack (in tesla): (a) Linear defect; (b) Zigzag defect; (c) Curved defect (d) Star defect; (e) Double linear defect.

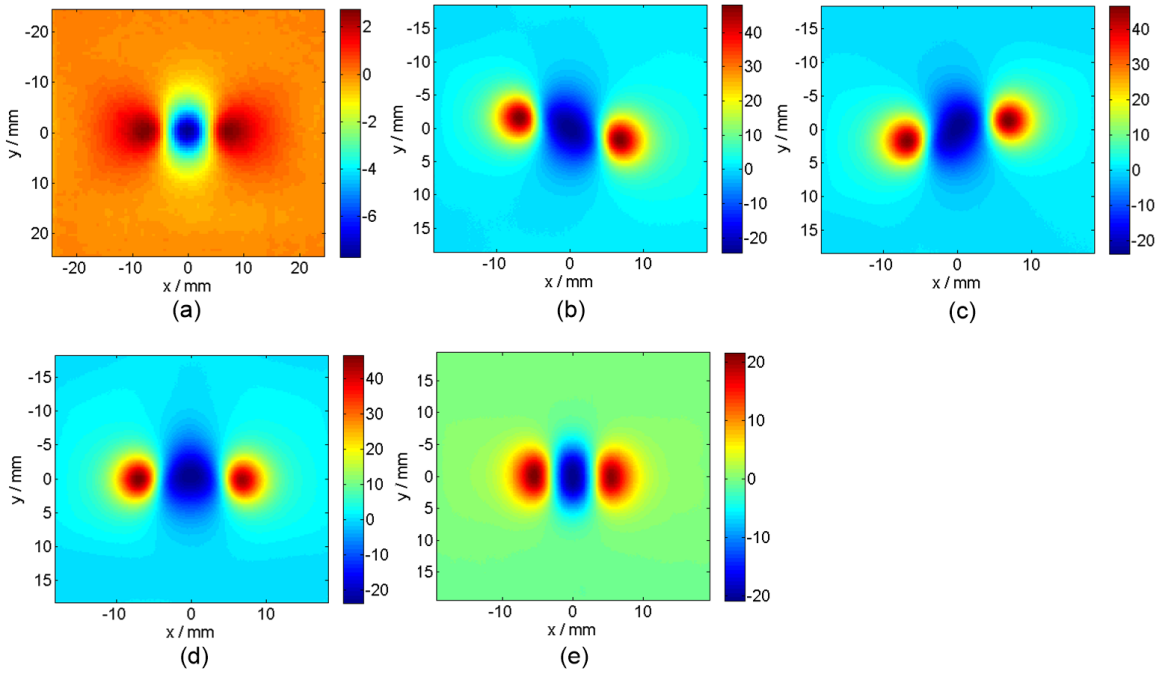

Figure 5.54: 2D maps of phase shift between excitation signal and output sensor signal for each crack (in degrees): (a) Linear defect; (b) Zigzag defect; (c) Curved defect (d) Star defect; (e) Double linear defect.

For all images of the B_x component presented in Figure 5.53 and Figure 5.54, a small indication of the cracks orientation are visible on the results. However, the geometrical characteristic of the cracks are not so evident. The inverse problem algorithm with the kernel map b_x and Tikhonov regularization was applied to the data obtained experimentally. A range of regularization parameter values was

applied to the algorithm and the best restored result (J) for each defect is presented in Figure 5.55. To remember that the kernel map b_x was based on the decomposition of the eddy current perturbation in elemental current dipoles whose elemental field is calculated using the Biot-Savart law, as already explain in subsection 4.3. This kernel map b_x was calculated for a distance of z=3.5 mm between the sample plates and the GMR sensor.

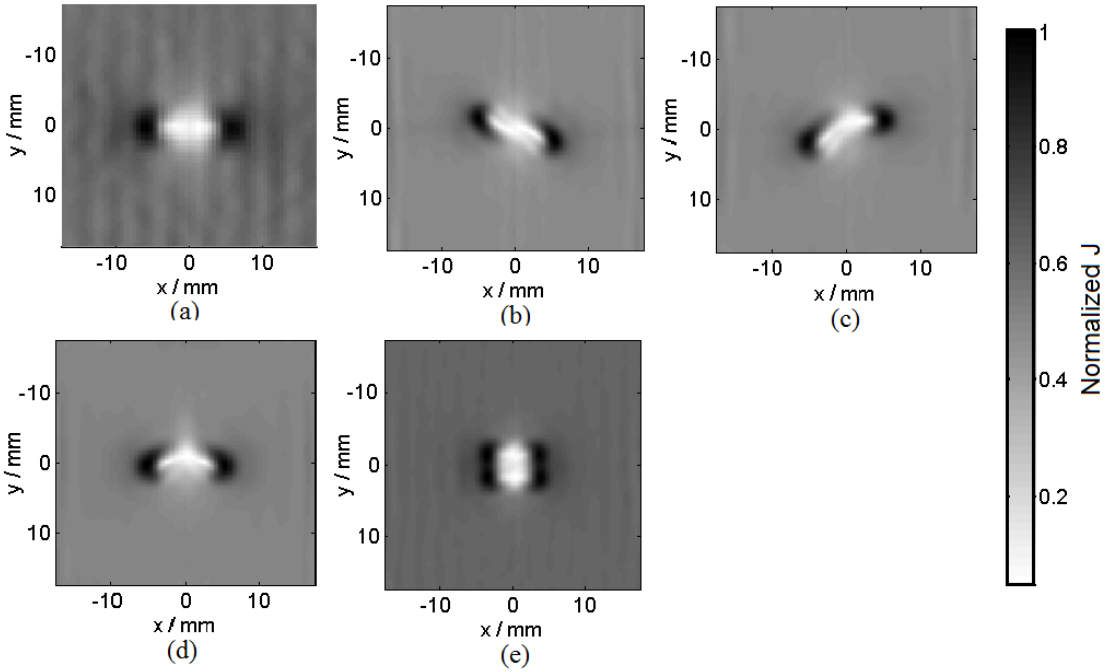

Figure 5.55: 2D normalized maps of the total restored eddy current density on the plate for each crack normalized to [0 1]: (a) Linear defect; (b) Zigzag defect; (c) Curved defect (d) Star defect; (e) Double linear defect.

The results show a white zone that is a current-free zone, giving emphasis to geometrical characteristics of the defects. This zone close to zero represents the current fault due to the defect presence on the plate. The results also show a black zone that represents a high density of current in the limit of the defects. This effect was expected due to the eddy current be forced to deviate to crack position. Analysing the star defect, the results don't show clearly the three limit of the crack. The characterization of the defect can be improved by rotation the probe, forcing the current to flow around the defect in a different way. Figure 5.56 depicts the restored eddy current density obtained for the star defect when probe rotation was changed 90 degrees. In that case, the geometrical characteristic of the defect is clearly visible.

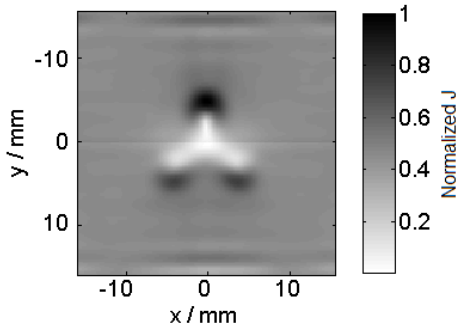

Figure 5.56: 2D map of the total restored eddy current density on the plate for the star defect, when probe was rotated 90°

.

An approximate value of the defects size can be observed by the restored image. For the experimental conditions of this work (excitation frequency and intensity, type and thickness of the material) it was observed that the distance between the crack tips and the current density maximum points was always between 1.1 mm and 1.3 mm. These values are compatible with a maximum error of 0.2 mm in the location of the tips.

These results were also obtained from measuring the magnetic field component parallel to the excitation current B_y. Similar results of restored eddy current density and eddy current lines were obtained.

5.7 Optimized Probe and Final Experimental Setup

In the previous section, the planar probe was used to induce eddy current with an uniform current distribution on the surface of the specimen along one direction in the region of the crack. The algorithm of inversion presented in the previous chapter was applied to evaluate the geometry of the cracks. As expected, the reconstructed eddy current pattern contained relevant information about the geometry of cracks that are not parallel to the current flow. For the case when the eddy current flow parallel to the crack, the rotation of the probe was required to induce currents in a different orientation in order to characterize the total profile of the crack. As in practical situations the real profile of the crack is unknown, the use of this kind of probe requires the evaluation of the crack for a set of different probe angles which makes this method slow. For this purpose, an improvement to the probe was made to induce uniform currents in the specimen in different directions without physical rotation of the probe during the scan.

5.7.1 Optimized Probe

The new probe presented in this subsection allows the induction of eddy currents with different orientation on the metal surface without rotating the probe during the scan. The probe includes two planar excitation coils with 21 conductors in the center of the coil, having an uniform area of (30x30) mm^2 that produces the uniform primary magnetic field around the zone of two sensors. The

coils are depicted in Figure 5.57(a) and they were especially designed to be perpendicular, in order to induce uniform eddy current distribution in the plate at different directions.

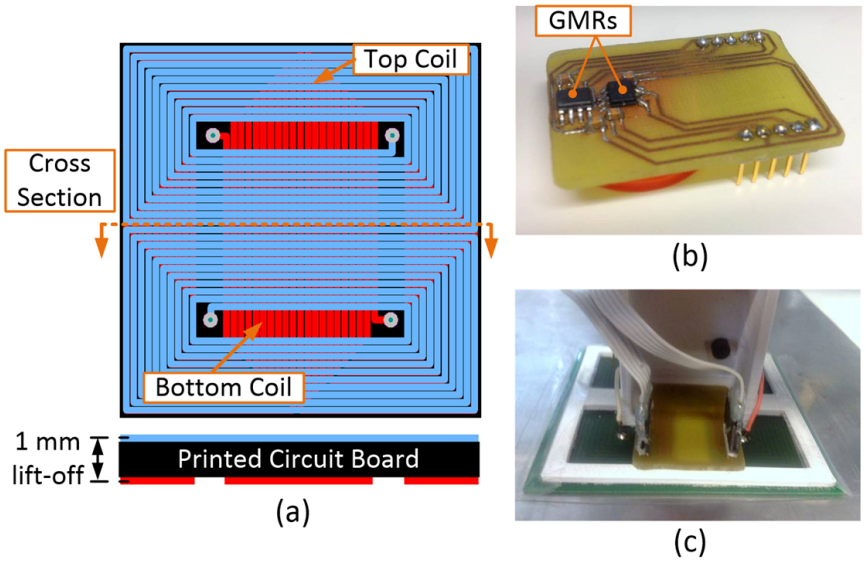

Figure 5.57: Photographs of the probe built for this work: (a) Footprint of the two planar coils; (b) Two GMR sensors; (c) Completed ECT probe.

Since one of the coils is in the top layer of the printed circuit board and the other is in the bottom layer, 1 mm lift-off between the two coils exists. Hence, the excitation current imposed in the two coils were compensated to induce the same eddy current density on the surface of the aluminium plate. Figure 5.57(b) depicts the two GMR sensors included in the probe. The two sensors are perpendicularly oriented and they were used in the calibration of the excitation currents. Only one sensor was used to obtain the magnetic field maps. Figure 5.57(c) depicts the built ECT probe.

5.7.1.A Biasing of the GMR Sensors

The sensors were carefully positioned in the center axis of the uniform field coils, with their sensitivity axis oriented along the direction of the conductors, as depicted in Figure 5.58.

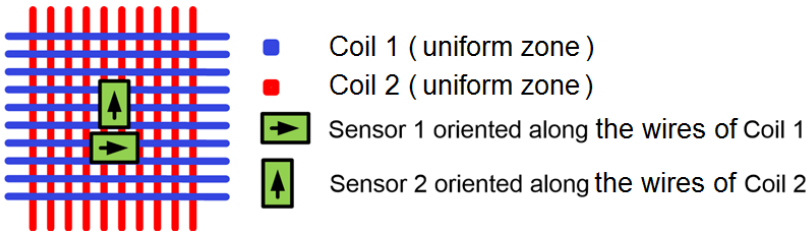

Figure 5.58: Representation of the center of the new probe, with sensors and coils orientations.

The GMR sensors were biased to operate in the linear region of their characteristics by placing a permanent magnet in the vicinity of the sensors. However, it is possible to say that this new probe allows the biasing of the sensors using another method. It can be done adding a DC value to the alternating current source of each coil. The DC value added to the current source 1 polarizes the sensor 2 in the linear zone and the DC value added to the current source 2 polarizes the sensor 1

in the linear zone. For each coil, experimental results show that a DC value of 100 mA is needed to polarize the sensors in their linear zone. When the polarization of the two sensors can not be achieved by placing a permanent magnet in the their vicinity, this method can be an alternative method to polarize the sensors in order to operate in their linear region.

5.7.1.B Amplitude Calibration of the Excitation Currents

Due to the existence of lift-off between the two excitation coils, amplitude compensation of one of the excitation current sources was required in order to produce the same magnetic field at the surface of the conductive plate under test. The information obtained from the two magnetic field amplitudes measured by the GMR sensors is used to calibrate the current sources. If the two coils are excited with sinusoidal currents at a fixed frequency with the same amplitudes and phases, the induced eddy currents in the specimen should be oriented at 45 degrees relative to each sensor and the amplitudes of the output voltage of the sensors should be the same. However, an unwanted difference between the two output voltages of the sensors exists due to the 1 mm distance between the two excitation coils. For this purpose, the comparison between the two voltage amplitudes measured by the sensors is used to obtain the ratio between the current sources. So, an auto-calibration was performed using a MATLAB program running in a personal computer to adjust one of the current sources, until the amplitude error between the two sensors signals is less than 0.01 V.

Figure 5.59 depicts the two GMR output signals in X-Y mode when the two coils are excited with a sinusoidal excitation at a 1 kHz frequency with the same amplitude (0.5 A) and equal phases (uncalibrated case), and when one of the amplitude current sources was calibrated. Note that the calibration procedure was done without any conductor material near the probe.

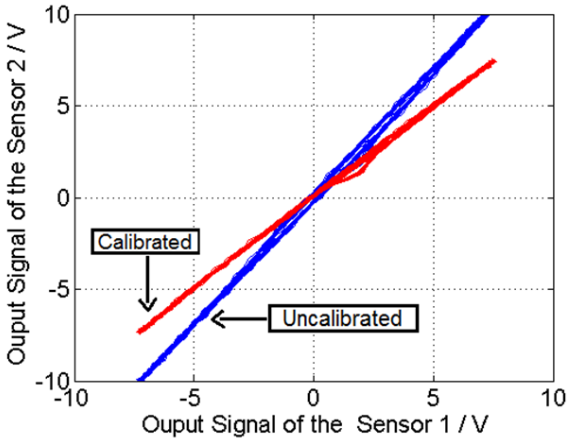

Figure 5.59: Amplitude voltage of the output signals of the GMR sensors in a XY mode when the amplitude current sources on the excitation coils are non-calibrated and calibrated.

The ratio between the two excitation sources was calculated when the amplitudes of the excitation currents were calibrated. For this experimental test, the ratio obtained was 1.36, indicating that the upper coil has to be excited with a sinusoidal current with amplitude 1.36 times higher than the lower coil in order to induce the same eddy current density on the surface of the metallic plate.

5.7.1.C Selection of the Directionality of the Induced Currents

After the auto-calibration of the amplitudes of the current sources, a set of several induced current directions has to be chosen (between 0 degrees to 360 degrees) to evaluate the total geometry of the cracks. The amplitudes of the excitation currents control the directionality of the induced current in the specimen using the parametric equation of an ellipse. Considering the experimental calibration example presented in the previous subsection where the ratio between the two excitation currents was 1.36, Figure 5.60 depicts the relationship between the amplitude of the excitation sources to control the directionality of the induced current in the metal.

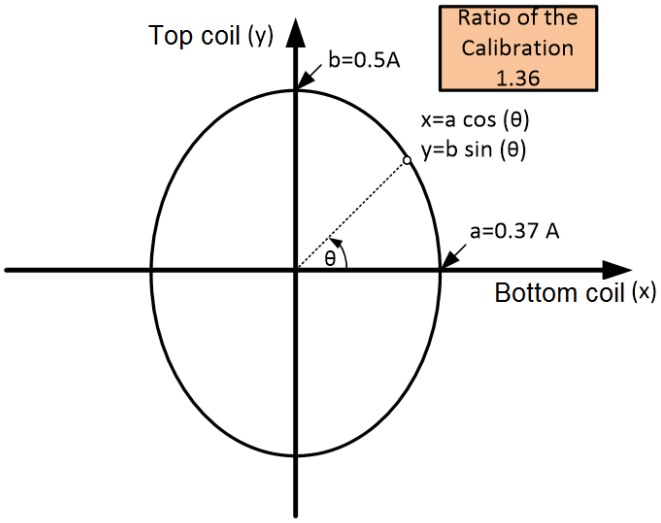

Figure 5.60: Representation of the relationship between the amplitude of the excitation sources that controls the directionality of the induced current in the specimen when the ratio between the two excitation currents was 1.36 (calibrated currents).

The calculated value of y is the amplitude value of the sinusoidal excitation that must be imposed in the top coil, while the calculated value of x is the amplitude value of the sinusoidal excitation that must be imposed in the bottom coil, in order to induce currents in the plate along the direction θ. The values of x and y will have a positive or negative sign corresponding to the quadrant of θ (where a negative value corresponds to a phase shift of 180 degrees in the respective excitation source).

5.7.2 Final Experimental Setup

As the previous experimental setup presented in this thesis, the probe was attached to a two axis positioning system to scan the defect region and the positioning system was controlled by a personal computer using a RS232 interface. Figure 5.61 depicts the measurement system used to acquire experimental data using the new ECT probe. The new probe includes two planar coils used in perpendicular directions to induce currents in different directions in the plate and two sensors to measure the magnetic field along its sensitive axis.

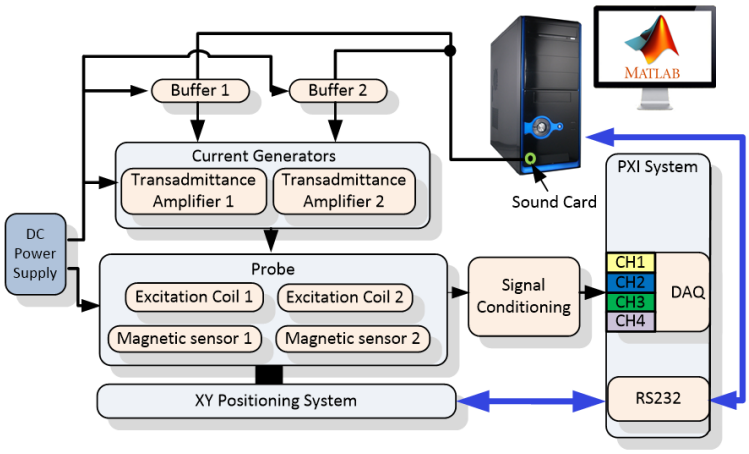

Figure 5.61: Experimental Setup.

The main difference in this new experimental setup is the insertion of two current generator circuits in the system in order to allow the control of the two amplitude value of the excitation source individually, and consequently control the directionality of the induced current in the metallic plate. The generation of the sinusoidal voltage of the excitation sources was done using the sound card of the personal computer that allow the generation of two synchronized analogue signals with frequencies up to 20 kHz. For each output of the sound card, a voltage buffer amplifier was used to protect a possible damage of the sound card. A capacitor was added in series with the output of each buffer amplifier to remove the unwanted DC values existing in the output of the sound card. Each signal is connected to a current generator circuit already presented in subsection 5.2.1 that contains an amplifier mounted on a transadmittance circuit to convert an alternating voltage source to a proportional alternating current source in the output load (coil).The excitation signals were obtained by monitoring the voltages of the 1 Ω resistor located in series with each coil. A signal conditioning module was required to adjust the output voltage from the GMR sensors in the limits of the DAQ ranges. The signal conditioning for the sensors includes an instrumentation amplifier (INA118 from Texas Instruments) with a gain of 101 and a 30 kHz low-pass filter to remove high frequency noise. A DC power supply providing $\pm$12 V was used to power the current generator module, the sensors and the conditioning circuit. After the signal conditioning block, for each position of the probe, the two excitation signals and the two GMR sensor signals are acquired by the data acquisition board (PXI-6251).

5.7.3 Geometrical Characterization of a Star Crack with the Optimized Probe

In this subsection, a crack with a star shape is evaluated using the new probe and the new excitation method. The new experimental setup was used to scan the sample plate in the region of the crack. The resulting images of the magnetic field perturbation component obtained experimentally for the induction of eddy currents with different orientation on the metal surface without rotating the probe during the scan will be presented. The obtained magnetic field maps from the scanning system were inverted to evaluate the geometric profile of the crack included in surface and sub-surface layers.

An aluminum alloy plate (Al1050) containing a surface defect (star shape) with three branches,

each of which has a length of 5 mm and width of 0.4 mm , was scanned. The XY positioning system moved the ECT probe with steps of 0.5 mm over a region of 45×45 mm around the crack. Figure 5.62 shows the representation of the aluminum plate scanned with the surface crack.

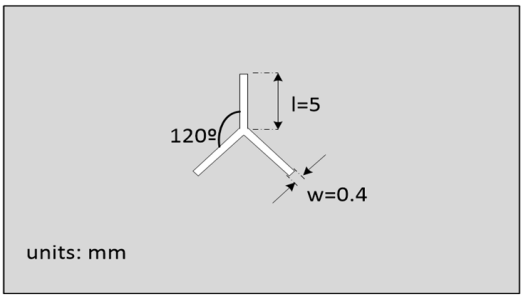

Figure 5.62: Representation of the analyzed aluminum sample and crack.

Two synchronized sinusoidal excitation currents at a frequency of 1 kHz were applied to the planar coils in order to induce eddy currents in the metal. The imposed amplitude and phase of the excitation coils were in charge of the direction of the current field that flow in the sample. At each probe position of the scan, four current directions (from 0 to 135 degrees with 45 degrees steps) are induced to the sample plate. Figure 5.63 depicts the four state of the current direction induced in the center region of the two coils, where 0 degrees corresponds the longitudinal direction of the wire of coil 1.

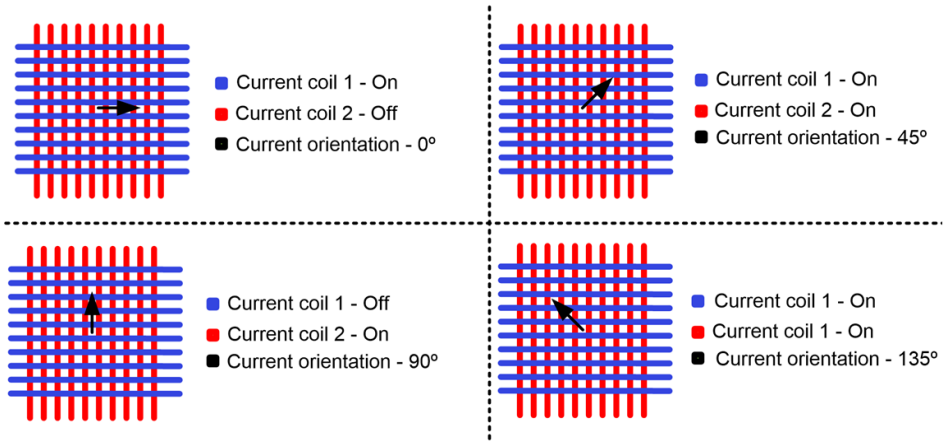

Figure 5.63: Illustration of the four current orientations imposed at each probe position of the scan.

For the induced current directions of 0, 45 and 90 degrees, the two excitation currents are always in phase. For the induced current direction of 135 degrees, the excitation current imposed in coil 2 has a relative shift of 180 degrees with respect to excitation current in coil 1. At each imposed current orientation, 100 periods of the excitation current and the measured output sensor voltages are acquired.

For each probe position and each induced current direction, a three-parameter sine-fitting algorithm is used to extract the parameters of amplitude and phase of the sinusoidal signals. After scanning the defect zone, the obtained amplitude maps from the sensors and the phase difference between the sensors and the excitation signals were saved. In this work, the obtained maps of am-

plitude of sensor 2 and the obtained phase shift maps between this sensor and the excitation current signal of coil 1 were used to reconstruct the eddy current distribution on the plate which contains enough information to determine the shape of the crack.

Figure 5.64 depicts these maps of amplitude and phase shift obtained with only one scan.

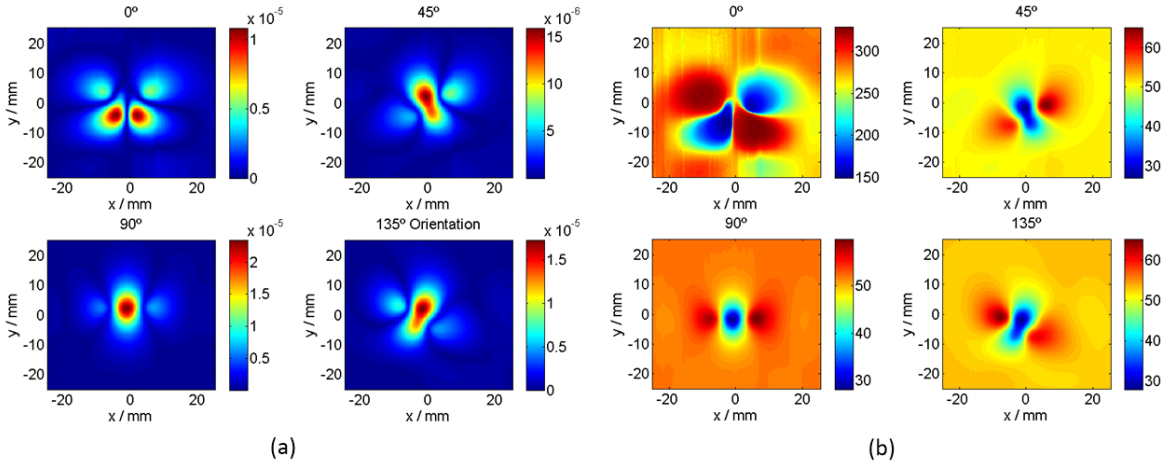

Figure 5.64: Experimental results obtained for the four imposed current flow in the plate (0; 45; 90 and 135°): (a) Amplitude maps of the magnetic field perturbation; (b) Phase shift maps between the magnetic sensor 1 and an excitation current: cases 0°, 45° and 135°, referenced to coil 1 while case 90°, referenced to coil 2.

It is possible to observe the presence of perturbation in the amplitude and phase maps, giving indication of a crack in the metal. However, the crack shape can not be directly observed from these maps. For this reason, these maps were inverted to obtain the eddy current perturbation in the metallic plate, in order to identify the geometry of the crack. At each pair of amplitude and phase maps obtained with one current direction, a complex map was obtained to be processed in the inverse problem algorithm. For each angle of current direction, the eddy current distribution in the sample plate is obtained by inverting the obtained complex map. The obtained eddy current distribution is a complex map, whose magnitudes are depicted in Figure 5.65 for the four induced currents (0; 45; 90 and 135 degrees). The images were normalized and are represented in a gray scale with an arrow representation of the current direction that is induced in the plate.

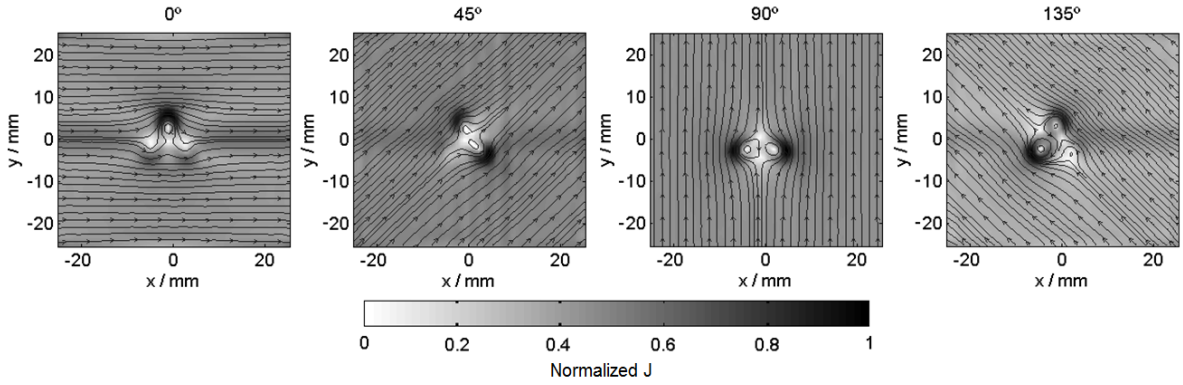

Figure 5.65: Results obtained for the normalized maps of the eddy current distribution for the four induced current cases.

As expected, it is possible to observe that each image contains information about the crack shape in the plate. However, in this particular geometry of crack, all the edges of the crack can not be determined just with one image, because the direction of current flow may be in the same direction of defect edge. To improve the characterization of the crack from these images of eddy current density, a normalized map with the summation of the four eddy current densities was created and is depicted in Figure 5.66.

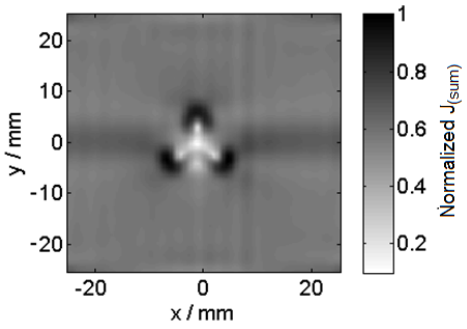

Figure 5.66: Normalized map obtained by the sum of the four eddy current density maps (0; 45; 90 and 135°).

It is visible in Figure 5.66 that the sum of the four eddy current densities shows the complete defect geometry of the star crack. As expected, the new probe allows the characterization of the geometry of cracks from the eddy current density maps with only one scan, without recourse to several scans with different probe orientation to obtain the complete information about the defect geometry.

5.7.3.A Sub-surface Crack Evaluation in a Multilayer Structure

In order to test the method for sub-surface crack location in multilayer aluminum alloy structures, scan maps were made in four multilayer aluminum alloy plates (Al1050), with the thickness of each plate equal to 1 mm. One of the plates contains the star shape defect, as depicted in Figure 5.67(a), while the other three plate samples are flawless, as depicted in Figure 5.67(b).

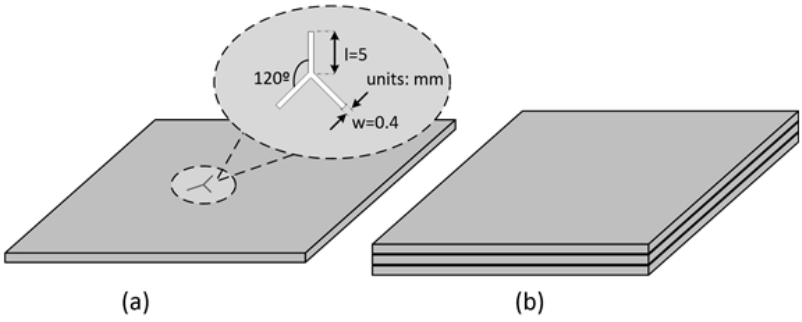

Figure 5.67: Representation of the aluminum samples used in the multilayer test: (a) Sample with the star crack; (b) Three flawless samples.

The aluminum plate that contains the crack was analysed in three sub-layer positions as depicted in Figure 5.68. For each case, the excitation coils were supplied with the same conditions of the previous experimental test.

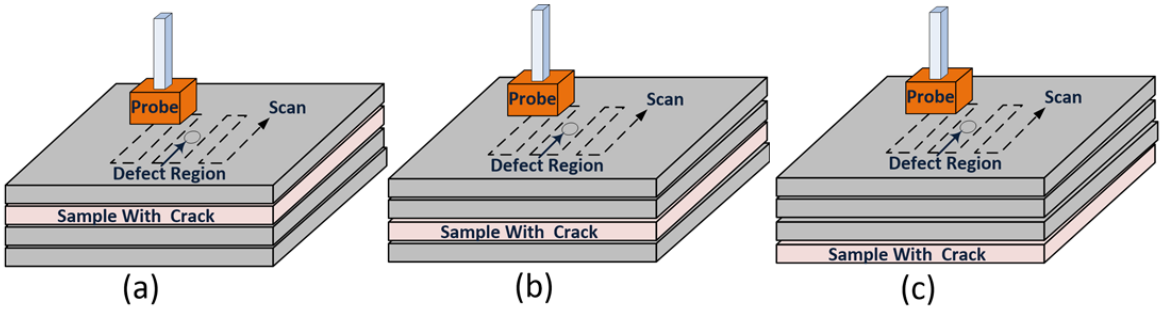

Figure 5.68: Representation of the experimental scans made to analyze the sub-surface crack in multilayer aluminum alloy structures: (a) Crack in the second layer; (b) Crack in the third layer; (c) Crack in the fourth layer.

The amplitude images of the defect in different layers for the 45 degree induced currents were obtained to understand the effect of noise on the experimental data as depicted in Figure 5.69. The data were obtained for all the induced current angles. However, only the 45 degree maps are presented here.

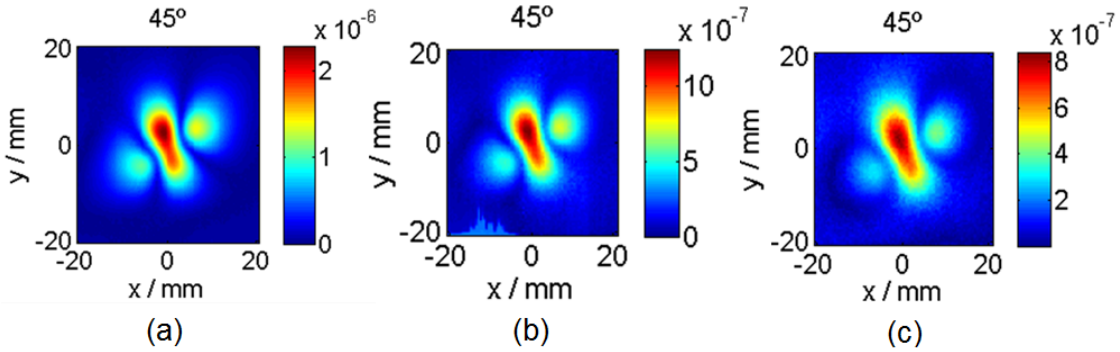

Figure 5.69: Scanning images used to analyze the sub-surface crack in multilayer aluminum alloy structures: (a) Crack in the second layer; (b) Crack in the third layer; (c) Crack in the fourth layer.

In Figure 5.69 (b) and (c), it is visible that the magnetic field images contains a high level of noise, which may reduce the quality of the reconstructed current maps.

For the sub-surface crack analysis, the z distance between the obtained measured field maps and the layer under analysis was adjusted in the calculation of the kernel map (b) used in the inversion. For the case where the crack was located in the second layer during the scan, the obtained amplitude and phase maps were inverted considering three different z distances in the calculation of the kernel. For each z, the normalized resulting map of the sum of the four eddy current density maps is depicted in Figure 5.70.

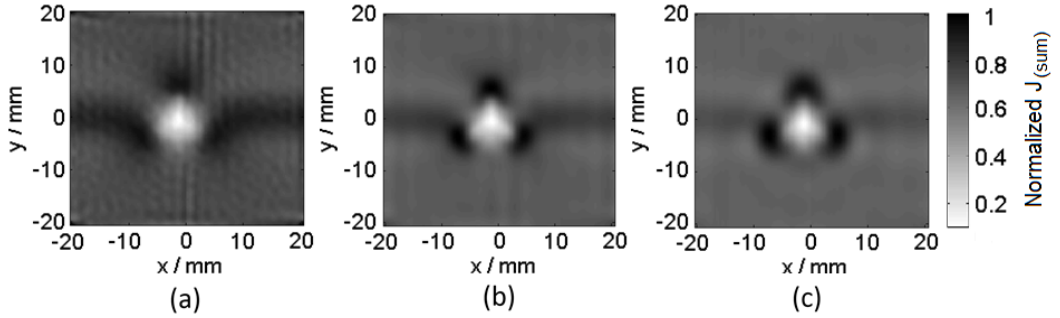

Figure 5.70: Normalized maps obtained by the sum of the four eddy current density maps (0; 45; 90; and 135°) when the crack is in the second layer applying different z distances in the calculation of the kernel: (a) z=2 mm; (b) z=4 mm, (c) z=6 mm.

Observing Figure 5.70, the inverted results show that the crack is clearer when a z value of 4 mm is considered in the inversion. This means that the distance between the sensor and the location of the crack is approximately 4 mm. Thus, for each case, the value of z was adjusted to obtain the best reconstructed images of the eddy current density maps. Figure 5.71 depicts the normalized maps for three situations.

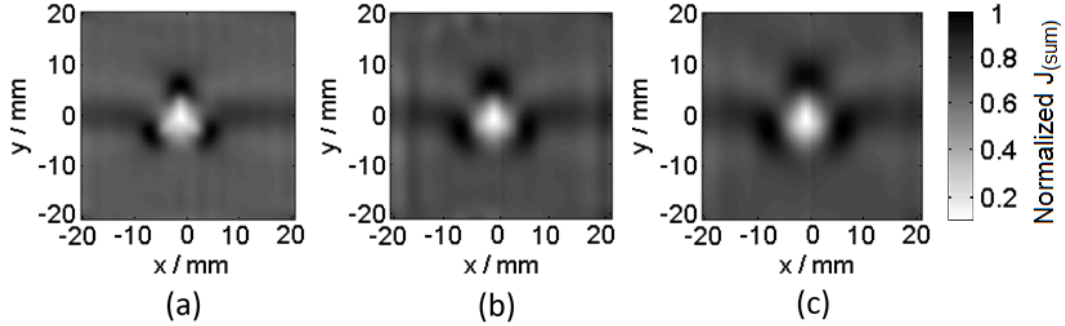

Figure 5.71: Normalized maps obtained by the sum of the four eddy current density maps (0; 45; 90; 135°): (a) Crack in the second layer; (b) Crack in the third layer; (c) Crack in the fourth layer

Observing the results, the defect in different layers has been detected qualitatively. The images extracted at deeper levels are not so clear due to the insufficient signal to the noise ratio of the experimental maps. However, it can be concluded from the study of sub-surface cracks that the shape of a crack should be visible if the experimental data provide a high enough signal to noise ratio to the defect evaluation. This kind of combination of excitation method, probe geometry, and inversion process yields a good solution for evaluating cracks with arbitrary geometric profiles.

6

Tube Inspection

Contents

6.1 Chapter Summary

The remote field eddy current testing (RFECT) is an electromagnetic NDT method, which is used for the wall inspection of metallic tubes. This method allows the detection of internal and external discontinuities with approximately equal sensitivity. In this chapter, it is described an experimental work made in the inspection of metallic tubes using the RFECT method. The high sensitivity of the the giant magneto-resistor GMR sensor and anisotropic magneto-resistor AMR sensor were employed as detector in stainless steel tubes. Two probes were built to compare the detection capabilities in standard defects like longitudinal and transverse defects. To accomplish this task, experimental measurements and numerical simulations using a commercial finite element package were performed. The principle of the RFECT method is presented in section 6.2. Information about the sample tubes that are analysed in this research work can be found in section 6.3. The experimental setup is described in subsection 6.4. In order to understand the magnetic field diffusion along a tube wall, simulation works and experimental validation results were presented in section 6.5. The designed RFECT probes and their construction were explained in subsection 6.6. Experimental results of defect detection with AMR and GMR are included in section 6.7. 2D images of the perturbed magnetic field when a tube contains a longitudinal or a transversal crack were obtained using a GMR probe and presented in section 6.8.

6.2 Principle of the Remote Field Eddy Current Testing Method

The RFECT method is currently applied in non-destructive evaluation of metallic tubes. The remote phenomenon is based on the through-wall indirect coupling energy path existing in the tube when one excitation coil with time-varying current at low frequency is placed inside the tube to produce a magnetic field that penetrates the tube wall. Figure 6.1 shows the principle of the remote field phenomenon.

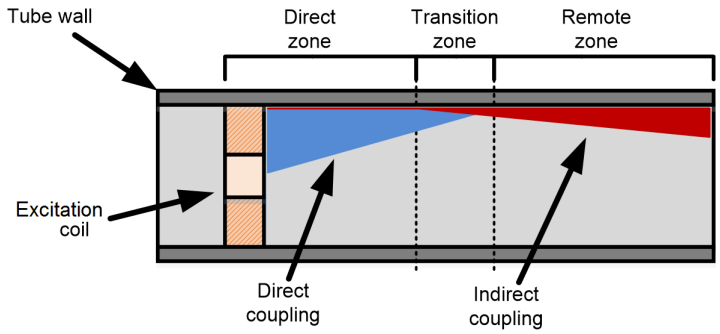

Figure 6.1: Representation of the principle of remote field effect along the tube wall.

In the direct zone, the magnetic field produced by the induced eddy currents in the tube wall are completely dominated by the strong magnetic field produced by the excitation coil. So, this strong magnetic field masks the weak magnetic field from the induced currents that contains information about defects. However, in the remote zone, the field produced by the induced eddy current is domi-

nant and the field diffusion along the tube wall is approximately equal both inside and outside the wall. If a defect is positioned in the tube wall on the indirect coupling path, it can be detected by the change of the remote electromagnetic field. In the actual inspection equipment, a detector coil is placed at a certain distance of the excitation coil in the remote zone to measure the remote magnetic field perturbation originated by the presence of a crack on the tube wall. Figure 6.2 shows a conventional remote field eddy current probe inside the tube wall. The distance between the excitation coil and the detector coil must be carefully chosen to perform a useful inspection of the tube wall. The remote field probes must be designed and built individually for each different tube type and tube dimension.

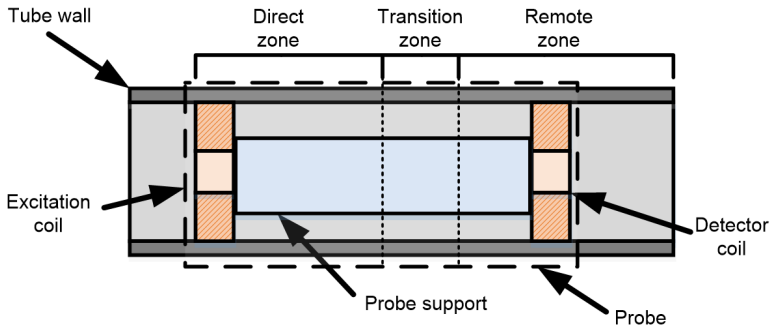

Figure 6.2: Representation of a conventional remote field eddy current probe inside the wall tube.

6.3 Tube Samples Description

The studies were performed in tube samples of austenitic stainless steel (AISI 304) with 26 mm of internal diameter, 28 mm of external diameter and thickness equal to 1 mm. The magnetic permeability of this material is $\mu_o = 4 \times \pi \times 10^{-7}$ H/m and the electric conductivity is $\sigma = 1.4$ MS/m. This type of steel is non-ferromagnetic and it is used in several industries due to its good resistance to corrosion. In order to simulate the real cracks in the tube, two artificial longitudinal and transverse cracks were machined in the tube to test the defect detection with AMR and GMR sensors. Figure 6.3 presents the two types of defects analysed in this Chapter.

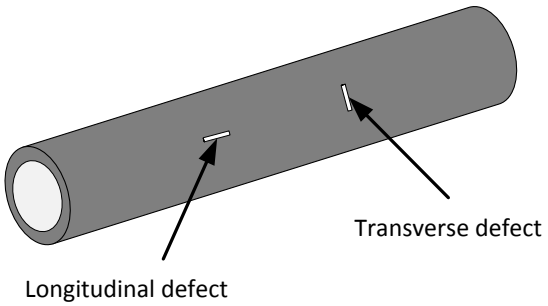

Figure 6.3: Representation of the defects tested in this work.

6.4 Experimental Setup

The system used to realize the experimental measurements is depicted in Figure 6.4. This experimental system is similar to the experimental setup presented previously for aluminium plates in chapter 5, section 5.3. However, some modification was made.

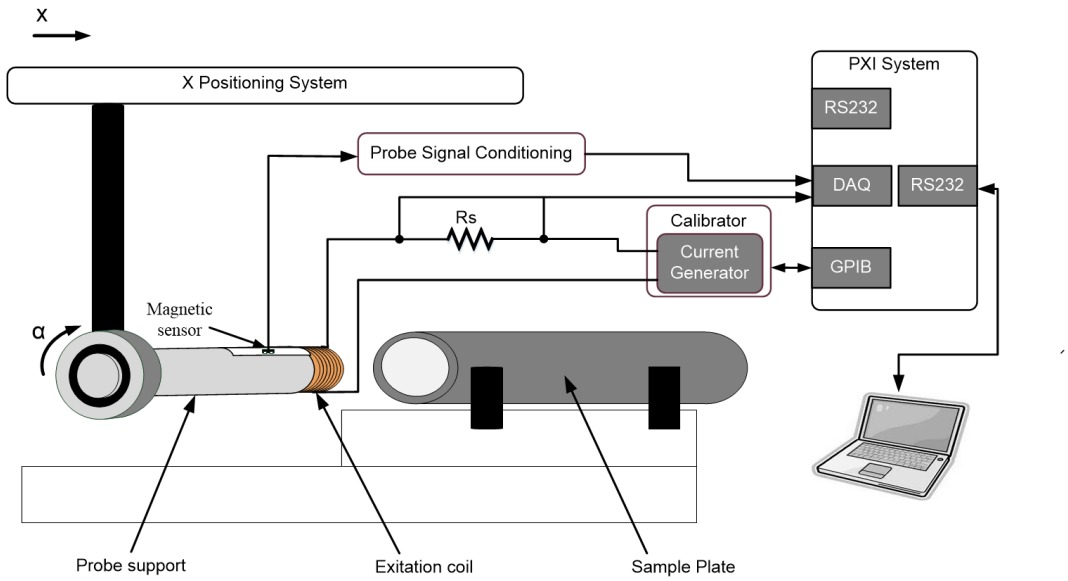

Figure 6.4: Experimental setup for tube inspection.

A MATLAB program was used in a personal computer (PC) to control the measurement system, to acquire the data and to process the results. The PC managed a PXI system that controls the scanning position through RS232 interface and acquires the signals through a multifunction data acquisition (DAQ) board TB-2708 from National Instruments. In that experimental setup, only the x-positioning system is used to move the probe into the tube. The x-positioning system uses one motorized axis that allows a motion range of 350 mm with a resolution of 0.05 mm. The support that attaches the probe to the positioning system allows the manual rotation of α degrees of the probe around the tube's centre point with 1 degree of resolution. The probe includes a magnetic sensor as detector and an excitation coil of 131 turns. The excitation coil has an inner diameter of 12 mm and outer diameter of 26 mm. A FLUKE 5700A calibrator is used to excite the coil with a sinusoidal current of constant amplitude. The magnetic field sensor output voltage was measured through CH1 of DAQ and the current was measured through CH2 of DAQ using as 0.22 Ω sampling resistor (R_s) which is connected in series with the excitation coil. The signal conditioning includes an instrumentation amplifier INA118 from Texas Instruments with 40 dB of gain.

6.5 Magnetic Field Diffusion Along The Tube Wall

A commercial 3D FEM simulation software was used to study the field diffusion along the wall of the austenitic stainless steel tube AISI 304 without defect. The simulation was performed in a tube with 28 mm of external diameter and thickness equal to 1 mm. The simulation was made applying

a sinusoidal current with frequency equal to 1 kHz and amplitude equal to 100 mA (rms) to excite a coil placed in a fixed position into the tube, as depicted in Figure 6.5. The frequency was chosen in relation to the standard depth of penetration δ=1.35 mm. At this frequency, the magnetic field diffuses easily to the outside of the 1 mm thick steel tube. The axial magnetic field intensity along 70 mm of the inner and outer tube wall was obtained. In Figure 6.5, the dashed red lines marked along the tube wall represents the inner and the outer magnetic field paths obtained.

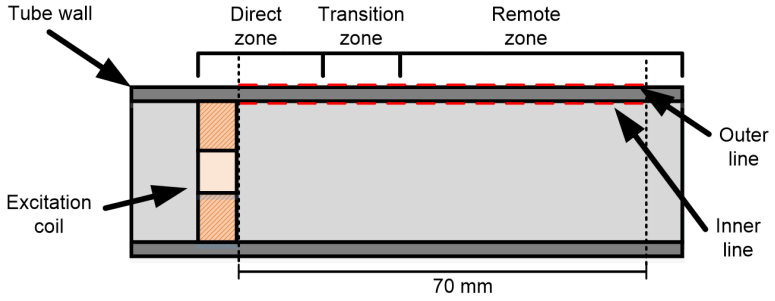

Figure 6.5: Illustration of the simulation model used to study the magnetic field diffusion along the tube wall.

The simulated axial magnetic fields along both inner and outer tube wall are depicted in Figure 6.6.

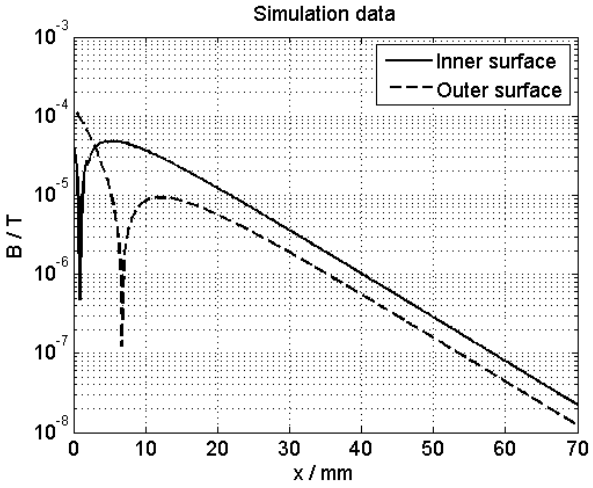

Figure 6.6: Axial magnetic field obtained with the FEM along the inner and the outer of the tube wall.

The simulation data represented in Figure 6.6 shows clearly the separation between the direct, the transition and the remote zones. The transition zone corresponds to the region where the magnetic field produced by the eddy currents begins to overlap the excitation magnetic field and creates a minimum in the magnetic field diffusion due to their opposing phases (x = 1 mm for the inner scan and x = 7 mm for the outer scan). In the remote zone, it is possible to observe that the field diffusion along the tube wall is of the same magnitude order both inside and outside the wall. This study helped to understand the range of remote field and proper placement of the detection sensor with respect to the excitation coil. As detector, the GMR sensor was used to measure the magnetic field along the inner and the outer surface of the tube wall. It should be noted that the sensing axis of the sensor was directed along the longitudinal direction of the tube in order to obtain the axial magnetic field close to the tube wall. The experimental results are depicted in Figure 6.7.

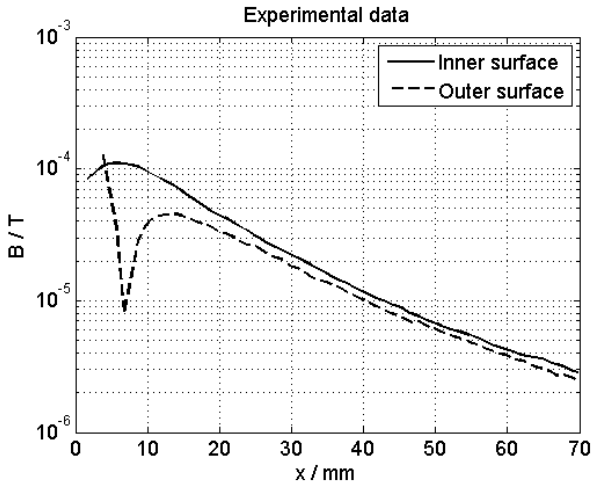

Figure 6.7: Magnetic field obtained with the experimental setup when the sensor moved along the inner and the outer tube wall.

The experimental data represented in Figure 6.7 does not clearly show the separation between the three zones. Observing the inner surface scan, the direct and transition zones are not visible due to the package size of the GMR sensor making it impossible to measure the magnetic field close to the coil. However, the remote zone is clearly visible in both inside and outside surface scans showing the approximately equal magnetic field diffusion along the tube wall. It is also possible to conclude that the distance between the excitation coil and the detector should be around 15 mm to ensure the equal magnetic field diffusion along the inner and the outer tube wall, with minimal attenuation. The phase difference of those fields in relation to the excitation current were also obtained and depicted in Figure 6.8.

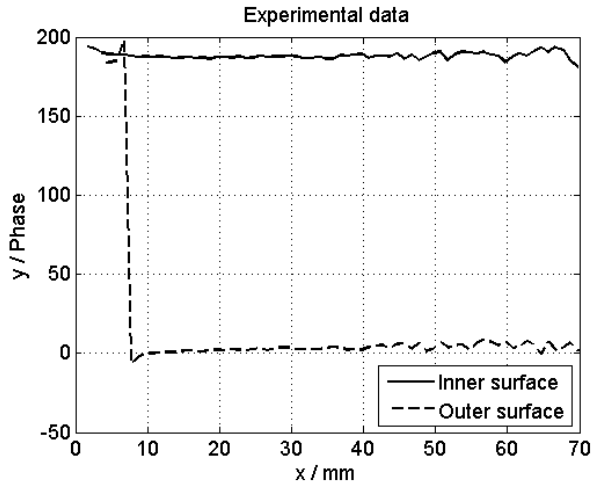

Figure 6.8: Phase difference between the amplitude of the GMR sensor output and excitation current obtained with the experimental setup when the sensor moved along the inner and the outer of the tube wall.

The phase difference represented in Figure 6.8 is compatible with the magnetic field amplitude surface obtained and presented in Figure 6.7. As expected, the phase value changes 180 degrees in the transition zone due to the phase opposition between the excitation field and the diffused magnetic field along the tube wall.This means that the sensed field inside the tube in the remote zone is due to

the eddy current and not to the primary excitation. From this conclusion, it is possible to say that the optimal distance between the excitation coil and the magnetic sensor depends on the data presented above, and must be determined and fixed for the construction of a RFECT probe. To be noted that several simulations were made with different excitation frequencies (1-100 kHz) and the position of the minimum magnetic field amplitude in the transition zone was not frequency dependent.

6.6 RFECT Probe

The choice of the optimal position for the detection sensor in a RFECT probe is very important for the defect detection and optimization. In this section, two probes are presented and the choice of the optimal position for the detectors is explained. Both probes were implemented with an 131 turns of excitation pancake coil with cross section equal to 7x7.3 mm and a magnetic sensor to measure the magnetic field. Experimental results were obtained for a fixed position of the excitation coil in the stainless steel tube (AISI 304) without defect and by moving the AMR and GMR sensors close to the inner wall in order to experimentally visualize the diffusion of the magnetic field along the tube wall, as depicted in Figure 6.9. The coil was excited with a sinusoidal current of 150 mA of amplitude at 5 kHz. The sensing axis of the sensors were directed along the longitudinal direction of the tube in order to obtain the axial magnetic field close to the tube wall.

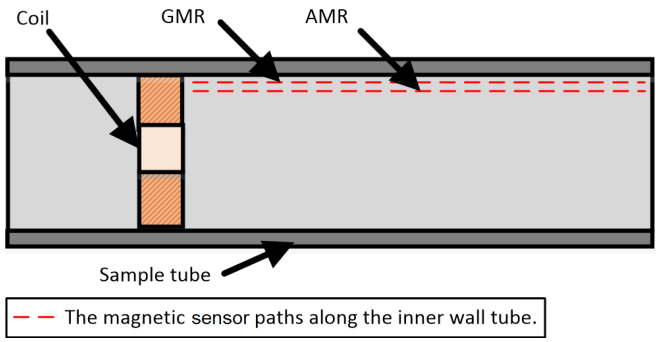

Figure 6.9: Illustration of the experimental test made to study the magnetic field diffusion along the inner tube wall using AMR and GMR sensors.

Figure 6.10 depicts the magnetic field intensity obtained experimentally along the inner tube wall using both sensors.

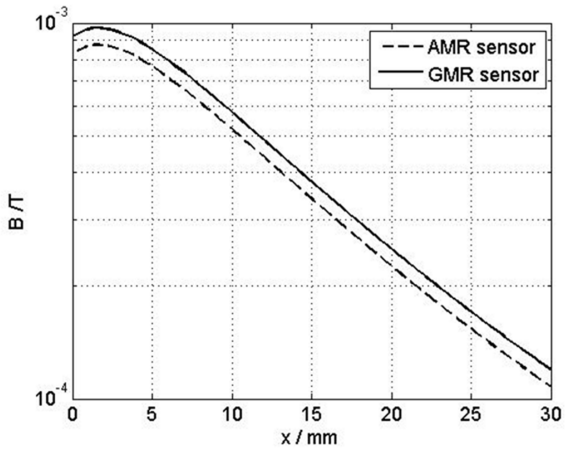

Figure 6.10: Magnetic field obtained with the experimental setup when the GMR sensor and the AMR sensor moved along the inner tube wall.

The magnetic field difference between the AMR and GMR output sensors observed in Figure 6.10 is due to the different distance between the detectors and the tube wall during the experimental scan. The GMR path is closer to the tube wall due to its smaller dimension. Besides that the direct and transition zones are not visible in the experimental data also due to the size of the package of the sensors that does not allow measuring the magnetic field close to the excitation coil. However, it is clearly possible to observe the remote field zone. The information given in Figure 6.10 shows that the distance between the excitation coil and the detector must be greater than 3 mm to ensure that the measured field inside the inner tube wall is in the remote zone. However, to ensure the equal magnetic field diffusion along the inner and the outer tube wall, the distance between the excitation coil and the detectors was chosen to be equal to 15 mm, as previously observed in Figure 6.7. The created probe structure for theAnisotropic Magnetoresistors (AMR) and the GMR probes is represented in Figure 6.11. Photographs of the constructed RFECT probes are given in Figure 6.12.

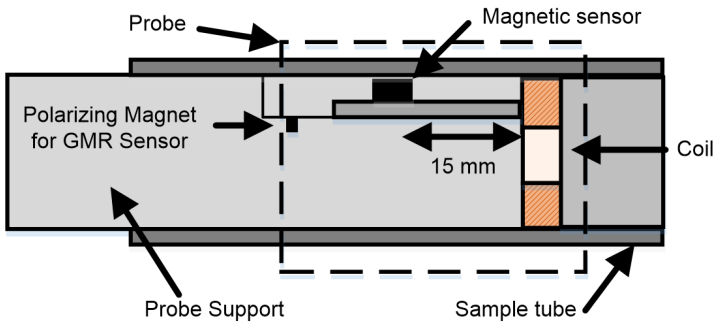

Figure 6.11: RFECT probe structure for AMR and GMR probes.

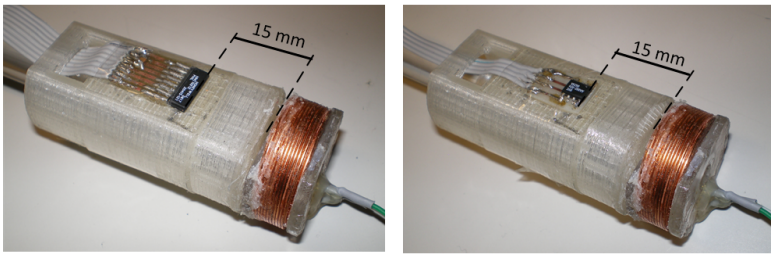

Figure 6.12: Photographs of the constructed RFECT probes: (a) AMR Probe with HMC 1021Z sensor; (b) GMR Probe with AA002-02E sensor.

6.7 Experimental Results in Defect Detection Using RFECT Probes with AMR and GMR Sensors

The experimental results were obtained by scanning two stainless steel tubes (AISI 304) with 1 mm of thickness, moving the RFECT probes inside the tubes. Photographs of the sample tubes are presented in Figure 6.13 with artificial machined defects (longitudinal or transversal geometry with 1 cm of length along their wall).

Figure 6.13: Photographs of the stainless steel tubes under test: (a) Sample tube with the longitudinal defect; (b) Sample tube with the transversal defect.

In this section, the applied excitation for all tests was sinusoidal with 150 mA of current amplitude at 5 kHz. It's important to remember that at this frequency the magnetic field diffuses easily to the outside of the stainless steel tube with 1 mm of thickness.

The first experimental test was made moving the probes along the inner surface of the tube that has a longitudinal defect. The output amplitudes of both sensors are depicted in Figure 6.14. The phase difference between the excitation current and each detector signal was also measured and depicted in Figure 6.15.

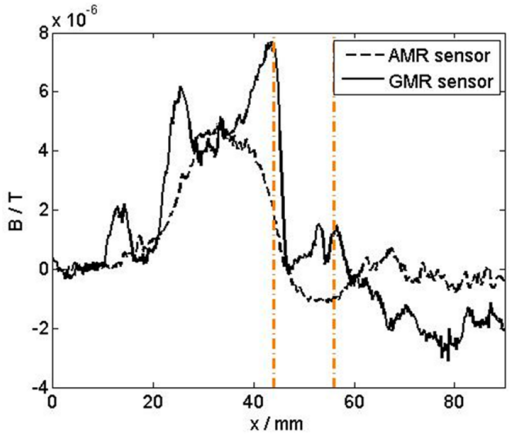

Figure 6.14: Output amplitudes (in tesla) obtained with the AMR and GMR sensors for detection of a longitudinal defect, applying a sinusoidal current with an amplitude of 150 mA at 5 kHz to the excitation coil.

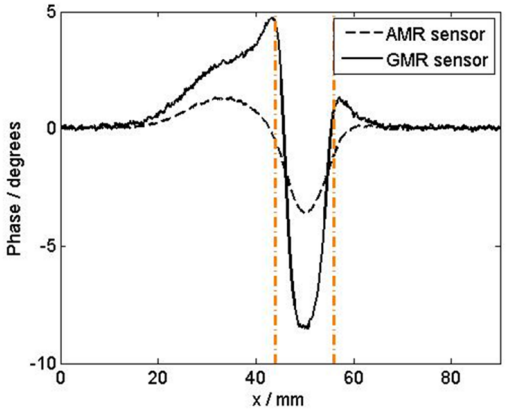

Figure 6.15: Phase difference between the excitation current and each sensor signal for defect detection of a longitudinal defect applying a sinusoidal current with an amplitude of 150 mA at 5 kHz to the excitation coil.

Figures 6.14 and 6.15 show an amplitude perturbation and phase perturbation when the probes passed under the longitudinal defect. The perturbation occurred between the positions x=45 mm and x=55 mm and corresponds to the defect position when the detector passed the defect. The defect zone is denoted by two orange colored vertical dotted lines. Observing the output amplitudes of the sensors depicted in Figure 6.14, a perturbation is present but it is not possible to conclude anything about the geometry of the defect. As we are dealing with high sensitive magneto-resistive sensors, the small non-constant distance between sensor and the tube wall during the experimental test causes strong fluctuations in the amplitude values. However, from the phase perturbation results depicted in Figure 6.15, the defect zone is clearly identified by a negative phase peak, matching approximately the real length of the longitudinal defect. The unexpected perturbation represented in Figure 6.14 and Figure 6.15 between x=20 mm and x=40 mm is caused by the passage of the excitation coil under the defect, changing the eddy current amplitudes. To split this effects, 30 mm were added to the chosen distance between the excitation coil and the sensors in order to ensure that the sensed magnetic field does not influence the excitation magnetic field variation. The magnetic field measured with this new modification was so small that it was impossible to detect the defect in test. Therefore, the 15 mm of

distance between the excitation coil and the sensors were maintained.

The same experimental scans were made applying a smaller sinusoidal current with an amplitude of 50 mA to the excitation coil. Figures 6.16 and 6.17 show the amplitude perturbation and phase perturbation when the probes passed close the defect.

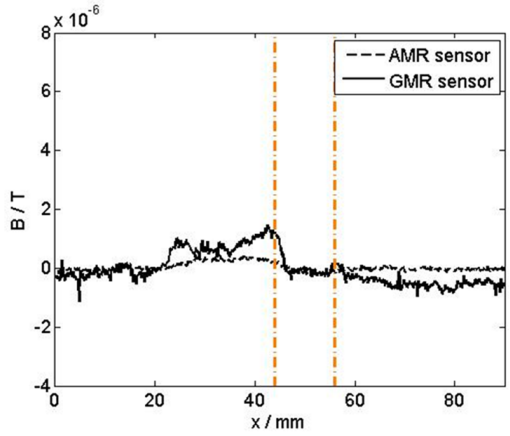

Figure 6.16: Output amplitudes (in tesla) obtained with the AMR and GMR sensors for detection of a longitudinal defect, applying a sinusoidal current with an amplitude of 50 mA at 5 kHz to the excitation coil.

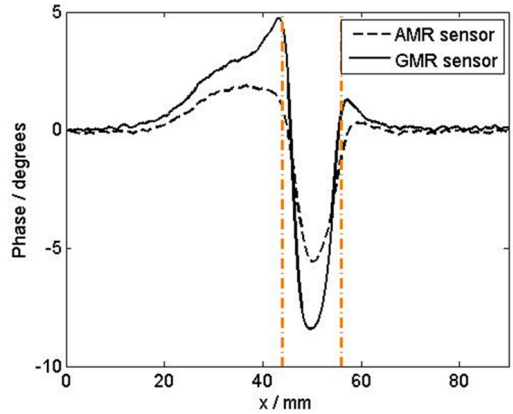

Figure 6.17: Phase difference between the excitation current and each sensor signal for defect detection of a longitudinal defect applying a sinusoidal current with an amplitude of 50 mA at 5 kHz to the excitation coil.

In Figure 6.16 the attenuation of the amplitude perturbation in both output signals is visible and the defect detection continue to be poor. However, Figure 6.17 shows that the phase perturbation continues to be presented between x=45 mm and x=55 mm with approximately the same variation type shown in Figure 6.15 for different current amplitude. This shows that the phase difference between the excitation current and the detector signal can be useful to detect and characterize defects with approximately the same information using different excitation current amplitudes.

The same comparison was made analysing the transverse defect. The results for the phase perturbation applying a sinusoidal amplitude current of 150 mA and 50 mA are depicted in Figure 6.18 and Figure 6.19, respectively. The defect position is marked with an orange line. Both figures show that the defect position is clearly identified by a negative phase peak for each probe.

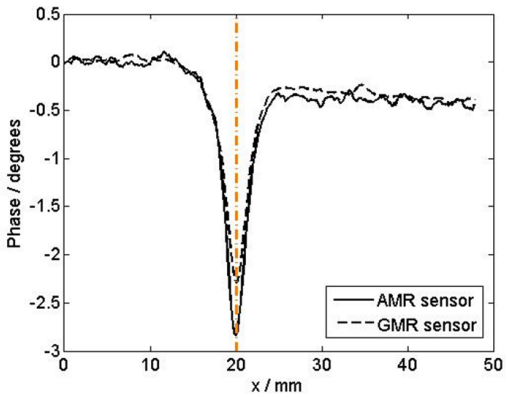

Figure 6.18: Output amplitudes (in tesla) obtained with the AMR and GMR sensors for detection of a transversal defect, applying a sinusoidal current with an amplitude of 150 mA at 5 kHz to the excitation coil.

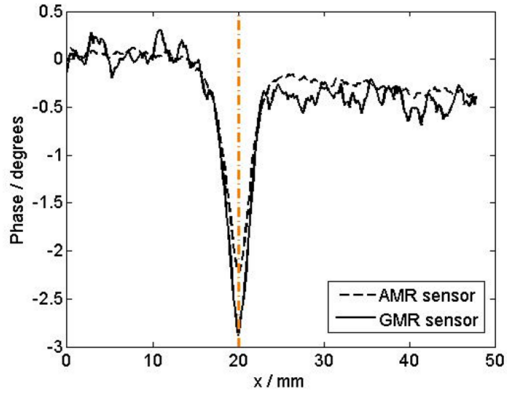

Figure 6.19: Phase difference between the excitation current and each sensor signal for defect detection of a transversal defect applying a sinusoidal current with an amplitude of 50 mA at 5 kHz to the excitation coil.

The unexpected perturbation presented when the longitudinal defect was scanned is not present when the excitation coil crosses the defect position. This is due to the circumferential nature of the excitation current because of the eddy current direction are parallel to the defect and perpendicular to the sensing axis of the detectors. It is also visible that the phase perturbation obtained between the excitation current and each sensor signal is maintained when a sinusoidal amplitude current of 150 mA or 50 mA is applied to the excitation coil.

6.7.1 Conclusions about the experimental study

The RFECT probes mounted with the AMR and GMR sensors as detectors seem to be good alternatives to the conventional RFECT probes that use coils as detectors. The main difference between these magneto-resistive sensors and coils is the possibility to use low frequency tests that allow an easy magnetic field penetration into thick wall tubes. The experimental results proved that these sensors are able to detect defects in stainless steel tubes using the remote field eddy current testing method. The results clearly show that the GMR sensor is more sensitive to the magnetic field than the AMR sensor. The results also show that the phase perturbation contains more clear information about defect presence when compared to the amplitude perturbation.

Furthermore, the phase perturbation remained unchanged for both 150 and 50 mA of excitation current, while the amplitude perturbation decreased with a decrement of the excitation current. This means that when the excitation current amplitude decreases, the amplitude output signal of both sensors becomes difficult to measure, however the phase still contains useful information caused by the defect presence.

Another important conclusion is related to the accuracy of the measurement of the geometrical sizes of the defects. Taken into consideration the phase measurements it is possible to conclude that we always got uncertainties under 5 mm for longitudinal defects. This quantity refers to the positions of the defect edges. For transverse circular defects the uncertainty is much lower, especially if the defect is perfectly circularly oriented.

6.8 Experimental Results in Defect Detection and Characterization Using RFECT Probe with a GMR Sensor

In this section, the experimental results were obtained by scanning the artificially machined longitudinal defect and the transversal defect of length equal to 1 cm, moving the GMR probe inside the wall tubes at several rotation angles. In this work, the distance between the excitation coil and the GMR sensor was adjusted to 17.5 mm. To accomplish the probe rotation, the probe support was attached to a rotating structure on the positioning system that allows the manually rotation of the probe with 1 degree of resolution. A set of 31 rotation angles from -90 to 90 degrees with 6 degrees steps (1 mm radial steps) were obtained, where 0 degrees matches the centre of the defect. Figure 6.20 depicts the obtained 2D map of the GMR output amplitude (in V) when the transversal defect was scanned. Figure 6.21 shows the obtained phase difference between the GMR output sensor and the excitation current. The experimental results were obtained by applying a sinusoidal current with amplitude of 200 mA at 5 kHz to the excitation coil.

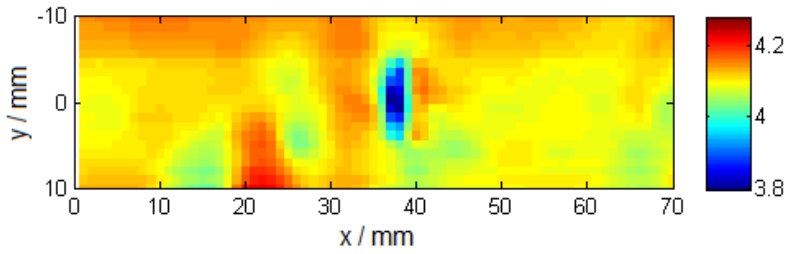

Figure 6.20: 2D amplitude map (in V) obtained by the GMR output voltage when the transversal defect was scanned.

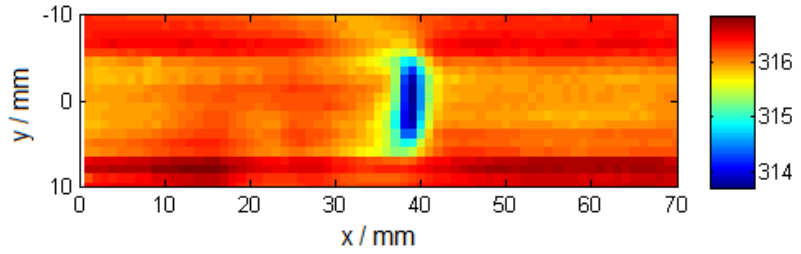

Figure 6.21: 2D phase map (in degrees) obtained by the phase difference between the GMR output sensor and the excitation current when the transversal defect was scanned.

Figures 6.20 and 6.21 show that an amplitude perturbation and phase perturbation are present between the positions 38 and 40 mm on the x-axis. It is also possible to observe that the phase perturbation has approximately 1.2 cm of length (y-axis) that approximately matches the real length of the defect. 2D experimental maps of amplitude and phase were also obtained scanning the longitudinal defect, and they are depicted in Figure 6.22 and 6.23, respectively.

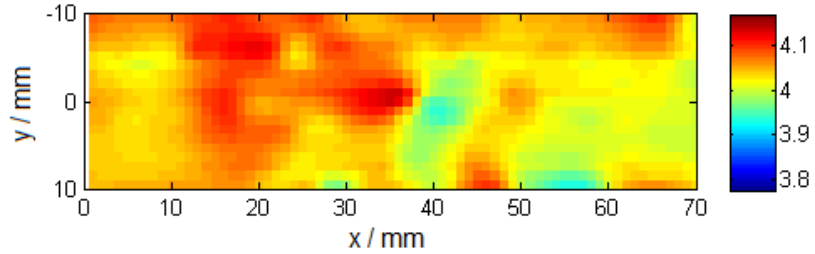

Figure 6.22: 2D amplitude map (in V) obtained by the GMR output voltage when the longitudinal defect was scanned.

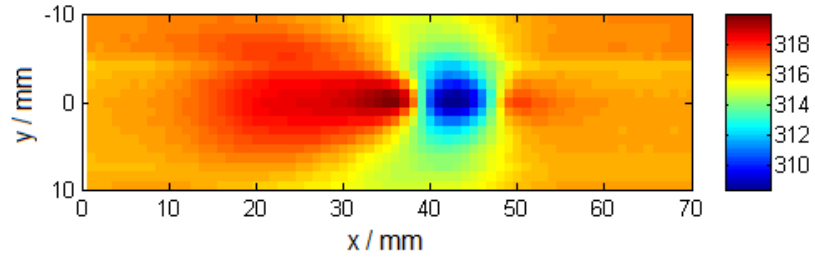

Figure 6.23: 2D phase map (in degrees) obtained by the phase difference between the GMR output sensor and the excitation current when the longitudinal defect was scanned.

From the 2D map of amplitude as depicted in Figure 6.22, it is not possible to conclude anything about the defect due to the low signal to noise ratio of the sensor output voltage. However, from the 2D map of phase depicted in Figure 6.23, it is visible that a phase perturbation is present between the positions 38 and 47 mm on the x-axis that approximately matches the real length of the longitudinal defect. The unexpected perturbation represented in Figure 6.23 between x=20 mm and x=38 mm is caused by the passage of the excitation coil under the defect due to the coil impedance change, as already mentioned in the previous section 6.7.

6.8.1 Conclusions about the Experimental Study

The GMR embedded in the RFECT probe as a magnetic sensor proved to be able to detect defects in stainless steel tubes. From the results, it is possible to conclude that the phase contains more information regarding the presence of a defect when compared to the amplitude. This was due to the low signal to noise ratio of the sensor output voltage. The length of the longitudinal and transversal defects was estimated from the phase difference between the GMR sensor output and the excitation current, and the determined values approximately matches with the real length of the defect. The passage of the excitation coil over the defect also affects the remote field perturbation due to the coil impedance change.

7

Final Remarks and Conclusions

Contents

7.1 Chapter Summary

This thesis is composed of new studies to evaluate cracks in non-ferromagnetic structures using eddy current testing (ECT) and imaging methods. Most of the presented work is based on the induction of eddy currents in metallic plates by applying a spatially invariant excitation field. The remote field eddy current testing was used for the wall inspection of metallic tubes. In this chapter, a summary of the developed work and the perspectives of the future development are presented.

7.2 Finite element method

Simulations were required and performed by finite element method FEM, to investigate the magnetic field response in the presence of defects using uniform excitation field. The lift-off effect, the edge effect, the current density, the depth of current penetration and the magnetic field perturbation around the defect were studied. When the lift-off changes, the results showed the magnetic field response also change. This should be taken in consideration in the analysis of the signals. A planar coil in contact with the specimen surface is a solution to maintain the constant distance between the probe and the sample, minimizing the lift-off effect. The results for the edge effect study showed that the influence of the edge on the invariant excitation field probe depends on the excitation frequency. A larger distance between the probe and the edge of the plate is needed when higher frequencies are used. Otherwise, signal corrections are required.

A study was made considering the perturbation of the magnetic field around linear cracks with different depths and lengths. The results for the current density, depth of current penetration and magnetic field perturbation around linear defects with different dimension showed that the estimation of the defect depth is harder than the estimation of the length, because the density of current that passes underneath the defect depends on the ratio of the length to the depth of the defect.

Another study regarding the measurement of the depth of surface and sub-surface cracks was performed. For linear cracks with a fixed length, 2D perturbation maps of the magnetic field around the cracks were obtained for a set of different crack depths. The results obtained with the planar probe showed that the complex signatures of the magnetic field maps contain relevant information about the depth of a crack. For surface and sub-surface defect cases, the obtained complex signatures showed that the amplitude peak of the magnetic field maps decreases with the decrease of the crack depth. For sub-surface cracks, the phase of the signatures changes in accordance with the crack depth.

7.3 Experimental Work

In the experimental work, a measurement system was adapted to make the inspection of cracks in metallic structures. Along the working period, the measurement system was modified according to the geometric profile of the inspected material (tube or plate) and the improvement of the probes. The setup, the implemented electronics, and the implemented signal processing methods that were used to perform the experimental work were explained in detail. The magneto-resistive sensors were

chosen due to their high sensitivity to the magnetic field variations and wide frequency bandwidth response.

New eddy current probes were built for the inspection of cracks in the aluminium plates. The technique was based on the induction of eddy currents in the conductive material originated by a sinusoidal magnetic field with an uniform spatial distribution in an area of few square centimetres at the surface. The probes included planar coils specially designed to provide the uniform magnetic excitation field surrounding a giant magneto-resistor GMR sensor that measures the perturbation component of the magnetic field in the region under test. 2D maps of the magnetic field component (B_x and B_y) were successfully obtained around different types of cracks. The lengths of the inspected cracks were between 5 mm and 20 mm. The first results showed that it is possible to evaluate cracks that are not parallel to the eddy current flow. A manual probe rotation was required to obtain additional information about each crack. However, the method was slow due to the requirement of several scans. Furthermore, small rotation errors were detected when measuring the magnetic field map due to mechanical misalignment of the probe. To overcome this difficulty, a faster excitation method and an improvement to the first probes were proposed and presented to induce uniform currents in the metallic plate in different directions without physical rotation of the probe during the scan. The method required the control of the amplitude and phase of two synchronized sinusoidal currents with two excitation coils, that are perpendicular to each other. It was possible to improve the time of the scan and the accuracy of the measurements. The proposed excitation method including the probe allowed to obtain the complete information about the geometry of a complex crack shape (star crack), showing its ability in the detection and the evaluation of cracks with arbitrary geometric profiles. Experimental results were obtained for surface and sub-surface crack evaluation.

For the inspection of cracks in the wall of tubes, the measurement system was modified in order to allow the manual rotation of the probe inside of tubes. Two probes, including circular excitation coil and a magneto-resistance sensor (GMR or AMR), were built and tested using remote field eddy current testing RFECT method. The experimental results showed that GMR and AMR sensors are good options to be implemented in RFECT systems. The results also showed that the phase perturbation contains clear information about the presence of the defect when compared to the amplitude perturbation. Furthermore, the phase perturbation remained unchanged for different excitation current amplitudes of 150 mA and 50 mA, while the perturbation of the amplitude decreases with the excitation current amplitude. This means that when the excitation current amplitude decreases, the amplitudes of the output signals of both sensors become difficult to measure. However, the phase still contains information caused by the defect.

7.4 The Inverse Problem

A new inverse problem algorithm was implemented to determine the spatial eddy current distribution (J) in the aluminium plates (from the map of the magnetic field component B_x, B_y or B_z). The main goal of the inversion method was the determination of the shape of the cracks using the recon-

structed eddy current pattern inside the aluminium plate. The method is an alternative approach to the state of the art approaches. The invariance of the primary excitation field for small spatial translations was essential for the success of the presented method to solve the inverse problem. The resulting excitation field is uniform which allows us the consideration of perturbation current component caused by the presence of the defect, as a collection of elemental current dipoles.

Due to the nature of the inverse problem being severely ill-conditioned, regularizations were required and implemented to suppress the effect of the noise in order to obtain a stable solution in the reconstructed image of J. To solve the problem, Tikhonov regularization and TV regularization (typically used in the de-noising image problems) were implemented and tested with successful results. In the context of our problem, the minimization problem using Tikhonov regularization was computationally faster when compared with the Total Variation (TV) regularization. To solve the determination of the regularization parameter value μ automatically, L-curve and Logarithmic energy derivative methods were implemented. Both methods were tested in experimental data considering that no-information about the cracks were known. The results showed that both methods were able to automatically return a optimal regularization parameter value giving a stable reconstructed image of J. The results showed that the reconstructed images of J (obtained by this inverse problem algorithm) provide relevant information about the length, the orientation and the geometry profile of cracks. This kind of combination of excitation method, probe geometry, and inversion process yields a good solution for evaluating cracks with arbitrary geometric profiles. Considering that the kernel map that inverts B on J is kept in memory, the processing time of the inverse problem algorithm, using a personal computer as we did in this work, was approximately 2 second which allows us to consider the application of this method in a complete automated ECT scanner. However, a limitation of this method is the two-dimensionality of the algorithm. For the sub-surface crack analysis, the distance between the GMR sensor and the layer under analysis must be considered in the inversion. Otherwise, the quality of the resulting images of the inversion is affected. Other tools have to be added to the algorithm to extract information about the depth of the cracks.

7.5 Future work

In the experimental work, it was possible to observe that the giant magnetic resistors GMR sensors are very sensitive to small perturbations of magnetic field (in the order of μT). The use of smaller GMR sensors is underlined in order to increase the resolution of the measured magnetic field, and consequently improve the quality of the reconstructed images of J. Nowadays, this could be possible due to the appearance of GMR sensors in the market with an area of 1 mm $\times$ 1.5 mm $\times$ 0.25 mm.

In the case of an industrial application, the scanning time of the inspected material could be reduced using an array of GMR sensors carefully oriented and positioned in the center of the invariance of the primary excitation field region. However, the calibration of a set of GMR sensors will be required. Each sensor will need to work in its linear region and their sensitivity compensated.

Another interesting further work is the use of multi-frequency excitation for the unknown location of sub-surface cracks in order to obtain additional information about the depth of cracks. The difficult task here will be to find a correlation between the real depth of the crack, the multi-frequency response and the arbitrary geometric profile of cracks.

Bibliography

[1] D. E. Bray and R. K. Stanley, *Nondestructive Evaluation: A Tool in Design, Manufacturing and Service*. CRC Press, 1997.

[2] J. Bowler and N. Harfield, "Evaluation of probe impedance due to thin-skin eddy current interaction with surface cracks," *IEEE Transactions on Magnetics*, vol. 34, no. 2, pp. 515–523, Mar. 1998.

[3] M. Tsuchimoto, A. Fukaya, and T. Honma, "An analysis of eddy current testing with sheet current," *IEEE Transactions on Magnetics*, vol. 29, no. 6, pp. 2455–2457, Nov. 1993.

[4] M. S. Safizadeh and M. Hasanian, "Gas pipeline corrosion mapping using pulsed eddy current technique," *International Journal Advanced Design and Manufacturing Technology*, vol. 5, no. 1, pp. 11–18, Dec. 2011.

[5] P. Y. Joubert and Y. L. Bihan, "Multi sensor probe and defect classification in eddy current tubing inspection," *Sensors and Actuators A*, vol. 129, no. 1-2, pp. 10–14, May 2006.

[6] W. Cheng, S. Kanemoto, I. Komura, and M. Shiwa, "Depth sizing of partial-contact stress corrosion cracks from ect signals," *NDT & E International*, vol. 39, no. 5, pp. 374–383, Jul. 2006.

[7] H. Ramos, O. Postolache, F. C. Alegria, and A. L. Ribeiro, "Using the skin effect to estimate cracks depths in metalic structures," *Proceedings of the IEEE Instrumentation and Measurement Technology Conference (I2MTC)*, pp. 1361–1366, 2009.

[8] B. P. C. Rao, *Practical Eddy Current Testing*. B. Raj and B. Venkatraman, Alpha Science International Ltd, 2007.

[9] J. H. Espina-Hernández, E. Ramírez-Pacheco, F. Caleyo, J. Pérez-Benitez, and J. Hallen, "Rapid estimation of artificial near-side crack dimensions in aluminium using a gmr-based eddy current sensor," *NDT & E International*, vol. 51, no. 1, pp. 94–100, Oct. 2012.

[10] C. Mandache and J. Lefebvre, "Transient and harmonic eddy currents: Lift-off point of intersection," *NDT & E International*, vol. 39, no. 1, pp. 57–60, Jan. 2006.

[11] A. L. Ribeiro, H. G. Ramos, and J. C. Arez, "Liftoff insensitive thickness measurement of aluminum plates using harmonic eddy current excitation and a gmr sensor," *Measurment*, vol. 45, no. 9, pp. 2246–2253, Nov. 2012.

[12] Y. He, F. Luo, M. Pan, F. Weng, X. Hu, J. Gao, and B. Liu, “Pulsed eddy current technique for defect detection in aircraft riveted structures,” *NDT & E International*, vol. 43, no. 2, pp. 176–181, Mar. 2010.

[13] Y.-K. Shin, D.-M. Choi, Y. J. Kim, and S.-S. Lee, “Signal characteristics of differential-pulsed eddy current sensors in the evaluation of plate thickness,” *NDT & E International*, vol. 42, no. 3, pp. 215–221, Apr. 2009.

[14] S. Yang, Y. Sun, L. Upda, S. S. Upda, and W. Lord, “3d simulation of velocity induced fields for nondestructive evaluation application,” *IEEE Transactions on Magnetics*, vol. 35, no. 3, pp. 1754–1756, May 1999.

[15] H. G. Ramos, T. Rocha, D. Pasadas, and A. L. Ribeiro, “Velocity induced eddy currents technique to inspect cracks in moving conducting media,” *IEEE International Instrumentation and Measurement Technology Conference*, pp. 931–934, May 2013.

[16] J. X. QIAO, J. P. HANSEN, and I. MAYES, “Automatic differential lift-off compensation (ad-loc) method in pulsed eddy current inspection,” *17th World Conference on Nondestructive Testing*, pp. 25–28, Oct. 2008.

[17] J. Kral, R. Smid, H. M. G. Ramos, and A. L. Ribeiro, “The lift-off effect in eddy currents on thickness modeling and measurement,” *IEEE TRANSACTIONS ON INSTRUMENTATION AND MEASUREMENT*, vol. 62, no. 7, pp. 1958–1968, Jul. 2013.

[18] J. G. Martín, J. G. Gil, and E. V.-Sánchez, “Non-destructive techniques based on eddy current testing,” *Sensors*, vol. 11, pp. 2525–2565, 2011.

[19] A. L. Ribeiro and H. G. Ramos, “Inductive probe for flaw detection in non-magnetic metallic plates using eddy currents,” *IEEE Instr. & Meas. Tech, I2MTC*, pp. 1447–1451, 2008.

[20] C. Carr, D. Graham, J. C. Macfarlane, and G. B. Donaldson, “Recent developments in squid nde,” *Physica*, vol. 16, no. 12, pp. 1387–1390, Nov. 2003.

[21] H. J. Krausen and M. V. kreutzbruck, “Hts squids for the nondestructive evaluation of composite structures,” *Physica C: Superconductivity*, vol. 368, no. 1–4, pp. 70–79, Mar. 2002.

[22] R. Nagendran, N. Chinnasamy, M. Janawadkar, R. Baskaran, L. Vaidhyanathan, and C. Sundar., “Optimum eddy current excitation frequency for subsurface defect detection in squid based non-destructive evaluation,” *NDT & E International*, vol. 43, no. 8, pp. 713–717, Nov. 2010.

[23] P. Ripka, “Advances in fluxgate sensors,” *Sensors and Actuators A: Physical*, vol. 106, no. 1–3, pp. 8–14, Sep. 2003.

[24] K. Kosmas, C. Sargentis, D. Tsamakis, and E. Hristoforou, “Non-destructive evaluation of magnetic metallic materials using hall sensors,” *Sensors and Actuators A: Physical*, vol. 161, no. 1–2, pp. 359–362, Apr. 2005.

[25] D. He, M. Shiwa, J. Jia, J. Takatsubo, and S. Moriya, “Multi-frequency ect with amr sensor,” *NDT & E International*, vol. 44, no. 5, pp. 438–441, Sep. 2011.

[26] A. Jander, C. Smith, and R. Shneider, “Magnetoresistive sensors for nondestructive evaluation,” *Nondestructive Evaluation for Health Monitoring and Diagnostics*.

[27] T. Dogaru and S. Smith, “Giant magnetoresistance-based eddy current sensor,” *IEEE Trans. Magnetics*, vol. 37, no. 5, pp. 3831–3838, Sep. 2001.

[28] D. Pasadas, H. G. Ramos, and F. Alegria, “Handheld instrument to detect defects in conductive plates with a planar probe,” *Instrumentation and Measurement Technology Conference (I2MTC)*, pp. 1–6, May 2011.

[29] D. Pasadas, T. Rocha, H. G. Ramos, and A. L. Ribeiro, “Evaluation of portable ect instruments with positioning capability,” *Measurment*, vol. 45, no. 1, pp. 393–404, Jan. 2012.

[30] V. P. Lunin, “Phenomenological and algorithmic methods for the solution of inverse problems of electromagnetic testing,” *Russian Journal of Nondestructive Testing*, vol. 42, no. 6, pp. 353–362, Jun. 2006.

[31] I. Elshafiey, L. Udpa, and S. S. Udpa, “Solution of inverse problems in electromagnetics using hopfield neural networks,” *IEEE Transactions on Magnetics*, vol. 31, no. 1, pp. 852–861, Jan. 1995.

[32] A. Bernieri, L. Ferrigno, M. laracca, and M. Molinara, “Crack shape reconstruction in eddy current testing using machine learning systems for regression,” *IEEE Transactions on Instrumentation and Measurement*, vol. 57, no. 9, pp. 1958–1968, Sep. 2008.

[33] H. G. Ramos, T. Rocha, J. Kral, D. Pasadas, and A. L. Ribeiro, “Assessing metal plate thickness: an svm approach with electromagnetic methods,” *Proc 12th IMEKO TC10 Workshop on Technical Diagnostics*, Jun. 2013.

[34] K. Koyama, H. Hoshikawa, and N. Taniyama, “Investigation of eddy current testing of weld zone by uniform eddy current probe,” *Proceeding of WCNDT*, 2000.

[35] E. Smith and T. Posluszny, “Uniform field generating eddy current testing processing method and apparatus,” *United States Patent 4594549*, 1986.

[36] M. P. Papaelias, M. C. Lugg, C. Roberts, and C. L. Davis, “High-speed inspection of rails using acfm techniques,” *NDT & E International*, vol. 42, no. 4, pp. 328–335, Jun. 2009.

[37] W. Li, X. Yuan, G. Chen, X. Yin, and J. Ge, “A feed-through acfm probe with sensor array for pipe string cracks inspection,” *NDT & E International*, vol. 67, pp. 17–23, Oct. 2014.

[38] G. Yang, Z. Zeng, Y. Deng, X. Liu, L. Udpa, A. Tamburrino, and S. Udpa, “3d ec-gmr sensor system for detection of subsurface defects at steel fastener sites,” *NDT & E International*, vol. 50, pp. 20–28, Sep. 2012.

[39] G. Yang, G. Dib, and L. Udpa, “Rotating field ec-gmr sensor for crack detection at fastener site in layered structures,” *IEEE Sensors Journal*, vol. 15, no. 4, pp. 463–470, Jan. 2015.

[40] M. Bertero and P. Boccacci, *Inverse Problems in Imaging*. IOP Publishing, 1998.

[41] B. Wang, W. Tan, Z. Huang, H. Ji, and H. Li, “Image reconstruction algorithm for capacitively coupled electrical resistance tomography,” *Flow Measurement and Instrumentation*, vol. 40, pp. 216–222, Dec. 2014.

[42] Z. Ren, C. He, and Q. Zhang, “Fractional order total variation regularization for image super-resolution,” *Signal Processing*, vol. 93, no. 9, pp. 2408–2421, Sep. 2013.

[43] C. V. Dodd and W. E. Deeds, “Analytical solution to eddy-current probe-coil problems,” *Journal of Applied Physics*, vol. 39, no. 6, pp. 2829–2837, 1968.

[44] J. H. Park, H. J. Kim, S. J. Song, J. W. Park, H. R. Yoo, Y. W. Rho, S. H. Cho, and D. K. Kim, “One-bed rfect system for inspection of circumferential cracks in 16 inch gas pipeline,” *10th International Conference on Ubiquitous Robots and Ambient Intelligence*, Nov. 2013.

[45] T. R. Schmidt, “History of the remote-field eddy current inspection technique,” *Materials Evaluation*, vol. 47, no. 1, pp. 14–22, Jan. 1989.

[46] D. J. L. Pasadas, A. L. Ribeiro, H. G. Ramos, and T. J. Rocha, “Defect detection in stainless steel tubes with amr and gmr sensors using remote field eddy current inspection,” *ACTA IMEKO*, vol. 4, no. 2, pp. 62–67, Jan. 2015.

[47] C. Multiphysics, COMSOL AB, ©1998-2013.

[48] N. C. Haywood and J. R. Bowler, “Eddy-current imaging of buried cracks by inverting field data,” *IEEE Trans. on Magn.*, vol. 28, no. 2, pp. 1336–1339, 1992.

[49] S. J. Norton and J. R. Bowler, “Theory of eddy current inversion,” *J. Appl. Phys.*, vol. 73, pp. 501–512, 1993.

[50] J. R. Bowler, “Eddy-current interaction with an ideal crack. i. the forward problem,” *J. Appl. Phys.*, vol. 75, no. 12, pp. 8128–8137, 1994.

[51] J. W. Brown and R. V. Churchill, *Complex Variables and Applications*. McGraw-Hill Education, 2004.

[52] A. L. Ribeiro, H. G. Ramos, and O. Postolache, “A simple forward direct problem solver for eddy current non-destructive inspection of aluminum plates using uniform field probes,” *Measurment*, vol. 45, pp. 213–217, 2012.

[53] A. Tikhonov and V. Arsenin, “Solution of ill-posed problems,” *V.H.Winston & Sons,Washington*, 1977.

[54] J. Lei, S. Liu, Z. Li, and M. Suns, “An image reconstruction algorithm based on the extended tikhonov regularization method for electrical capacitance tomography,” *Measurments*, vol. 42, pp. 368–376, 2009.

[55] J. Dias and M. A. T. Figueiredo, “A new twist: Two-step iterative shrinkage/thresholding algorithms for image restoration,” *IEEE Trans. on Image Processing*, Dec. 2007.

[56] D. J. Pasadas, A. L. Ribeiro, H. G. Ramos, and T. J. Rocha, “Ect image analysis applying an inverse problem algorithm with tikhonov/tv regularization,” *IEEE International Instrumentation and Technology Conf. (I2MTC)*, May 2015.

A

List of Contributions

A.1 Papers published in Journals

- D. J. Pasadas, A. L. Ribeiro, H. G. Ramos, T. J. Rocha, *Inspection of Cracks in Aluminum Multilayer Structures Using Planar ECT Probe and Inversion Problem*, IEEE Transactions on Instrumentation and Measurement, Vol. 66, No. 5, pp. 920-927, May 2017.
- D. J. Pasadas, A. L. Ribeiro, H. G. Ramos, T. J. Rocha, *Automatic parameter selection for Tikhonov regularization in ECT Inverse problem*, Sensors and Actuators A: Physical, Vol. 246, pp. 73-80, August 2016.
- D. J. Pasadas, A. L. Ribeiro, T. Rocha, H. G. Ramos, *2D surface defect images applying Tikhonov regularized inversion and ECT*, NDT& E International, Vol. 80 pp. 48-57, June 2016.
- T. J. Rocha, H. G. Ramos, A. L. Ribeiro, D. J. Pasadas, *Evaluation of Sub-Surface Defects Using Diffusion of Motion Induced Eddy Currents*, IEEE Trans. on Instrumentation and Measurement, Vol. 65, No. 5, pp. 1182-1187, May 2016.
- T. J. Rocha, H. G. Ramos, A. L. Ribeiro, D. J. Pasadas, *Magnetic sensors assessment in velocity induced eddy current testing*, Sensors and Actuators A-Physical, Vol. 228, pp. 55-61, June 2015.
- A.L. Ribeiro, D.J. Pasadas, H.G. Ramos, T. Rocha, *Defect detection in stainless steel tubes with AMR and GMR sensors using remote field eddy current inspection*, ACTA IMEKO, Vol. 4, No. 2, June 2015.
- T. J. Rocha, H. G. Ramos, A. L. Ribeiro, D. J. Pasadas, C. S. Angani, *Studies to optimize the probe response for velocity induced eddy current testing in aluminium*, Measurement, Vol. 67, pp. 108-115., May 2015.
- A.L. Ribeiro, D. Pasadas, H.G. Ramos, T. Rocha, *Determination of Crack Depth in Aluminum Using Eddy Currents and GMR Sensors*, Review of Progress in Quantitative Nondestructive Evaluation, 2015.
- A. L. Ribeiro, D. Pasadas, H.G. Ramos, T. Rocha, *Using Excitation Invariance in the Characterization of Defects by Eddy Current Image Constructions*, Procedia Engineering, Vol. 86, pp. 440-451, 2014.
- H.G. Ramos, T. Rocha, J. Král, D. Pasadas and A. L. Ribeiro, *An SVM Approach with Electromagnetic Methods to Assess Metal Plate Thickness*, Measurement, Vol. 54, pp. 201-206, 2014.
- D. J. Pasadas, A. L. Ribeiro, H. G. Ramos, T. J. Rocha, *Remote Field Eddy Current Tube Inspection Using Giant Magneto-Resistance Sensors*, International Journal of industrial electronics and drives, Vol. 1, No. 3, pp. 167-173, 2014.

- A. L. Ribeiro, H.G. Ramos, D. Pasadas, T. Rocha, *Regularization Methods to Assess the Eddy Current Density Inside Conductive Non-Ferromagnetic Media*, Review of Progress in Quantitative Nondestructive Evaluation, 2014.
- H.G. Ramos, T. Rocha, D. Pasadas and A. L. Ribeiro, *Faraday Induction Effect Applied to the Detection of Defects in a Moving Plate*, Review of Progress in Quantitative Nondestructive Evaluation, 2013.
- A. L. Ribeiro, H. G. Ramos, D. J. Pasadas, T. J. Rocha, *Eddy Current Mapping Inside a Plane Conductor with Flaws*, Review of Progress in Quantitative Nondestructive Evaluation, 2013.

A.2 Papers Published in Conferences

- A. L. Ribeiro, D. Pasadas, H.G. Ramos, T. Rocha, *Current Density by Inversion of One Measured Component of the Resulting Magnetic Field Perturbation*, 17th International Symposium on Applied Electromagnetics and Mechanics (ISEM), September 2015.
- R. F. Menezes, H. G. Ramos, D. J. Pasadas, T. Rocha, A. L. Ribeiro, *Evaluation of defect depth using three different eddy current methods*, 10th Conference on Telecommunications Conftele, September 2015.
- A. L. Ribeiro, D. Pasadas, H.G. Ramos, T. Rocha, *Regularization of the Inversion Process in Eddy Current Characterization of Superficial Defects*, International Workshop on Electromagnetic Nondestructive Evaluation (ENDE), September 2015.
- A. L. Ribeiro, D. Pasadas, H.G. Ramos, T. Rocha, *Measurement of the Fatigue Crack Depths in Aluminium Plates*, International Conference on Mechanics and Materials in Design, July 2015.
- H. G. Ramos, A. L. Ribeiro, T. J. Rocha, D. J. Pasadas, *Using a Mouse in ECT detectors*, International Conference on Mechanics in Design, July 2015.
- A. L. Ribeiro, D. J. Pasadas, H. G. Ramos, T. J. Rocha, *The Filtering Effect of the Tikhonov Regularization*, IEEE Metrology for Aerospace Conference (MetroAeroSpace), June 2015.
- D. J. Pasadas, A. L. Ribeiro, H. G. Ramos, T. J. Rocha, *ECT Image Analysis Applying an Inverse Problem Algorithm with Tikhonov/TV Regularization*, IEEE International Instrumentation and Technology Conf. (I2MTC), May 2015.
- T. J. Rocha, H. G. Ramos, A. L. Ribeiro, D. J. Pasadas, *Sub-Surface Defect Detection with Motion Induced Eddy Currents in Aluminium*, IEEE International Instrumentation and Technology Conf. (I2MTC), May 2015.
- A. L. Ribeiro, H. G. Ramos, D. J. Pasadas, T. J. Rocha, *Eddy Current Evaluation of Fatigue Crack Depths in Planar Metallic non-Ferromagnetic Materials*, RELACRE, 3^a Conferência Nacional em Ensaios Não Destrutivos (3CNEND), December 2014.

- H. G. Ramos, T. J. Rocha, D. J. Pasadas, A. L. Ribeiro, *Using a Mouse as a Positioning device in an Handheld Detector of Sub-Surface Cracks*, RELACRE, 3^a Conferência Nacional em Ensaios Não Destrutivos (3CNEND), December 2014.

- A. L. Ribeiro, D. J. Pasadas, H. G. Ramos, T. J. Rocha, *Determination of Crack Depth in Aluminum Using Eddy Currents and GMR Sensors*, Review of Progress in Quantitative Nondestructive Evaluation (QNDE), July 2014.

- H. G. Ramos, T. J. Rocha, A. L. Ribeiro, D. J. Pasadas, *Probe Optimization for Velocity Induced Eddy Current Testing in Aluminium*, 12th IMEKO TC10 Workshop on Technical Diagnostics, June 2014.

- A. L. Ribeiro, D. J. Pasadas, T. J. Rocha, H. G. Ramos, *Remote Field Eddy Current NDT in Tubes Using Anisotropic Magneto-Resistors*, 12th IMEKO TC10 Workshop on Technical Diagnostics, June 2014.

- H. G. Ramos, T. Rocha, A. L. Ribeiro, D. Pasadas, *GMR Versus Differential Coils in Velocity Induced Eddy Current Testing*, IEEE Instrumentation and Measurement Technology Conf. (I2MTC), May, 2014.

- D. J. Pasadas, A. L. Ribeiro, T. J. Rocha, H. G. Ramos, *Open Crack Depth Evaluation Using Eddy Current Methods and GMR Detection*, IEEE Metrology for Aerospace Conference (MetroAeroSpace), May 2014.

- A. L. Ribeiro, D. J. Pasadas, H. G. Ramos, T. J. Rocha, *Using Excitation Invariance in the Characterization of Defects by Eddy Current Image Constructions*, International Conf. on Structural Integrity (ICONS), February 2014.

- H. G. Ramos, T. J. Rocha, D. J. Pasadas, A. L. Ribeiro, *Determination of Linear Defect Depths from Eddy Currents Disturbances*, Review of Progress in Quantitative Nondestructive Evaluation (QNDE), July 2013.

- A. L. Ribeiro, H. G. Ramos, D. J. Pasadas, T. J. Rocha, *Regularization methods to assess the eddy current density inside conductive non-ferromagnetic media*, Review of Progress in Quantitative Nondestructive Evaluation (QNDE), July 2013.

- D. Pasadas, T. Rocha, A. L. Ribeiro, H. G. Ramos, *ECT Characterization of a Linear Defect from Multiple Angle Measurements*, 19th IMEKO TC 4 Symposium, July 2013.

- T. Rocha, D. Pasadas, H. G. Ramos, A. L. Ribeiro, *Metal Plate Thickness Classification In Eddy Current Testing Using Support Vector Machine*, 19th IMEKO TC 4 Symposium, July 2013.

- A. L. Ribeiro, D. J. Pasadas, H. G. Ramos, T. J. Rocha, *Using Tikhonov Regularization to Determine the Eddy Current Density in a Plate*, 18th International Workshop on Electromagnetic Nondestructive Evaluation (ENDE), June 2013.

- H. G. Ramos, T. J. Rocha, J. Kral, D. J. Pasadas, A. L. Ribeiro, *Assessing Metal Plate Thickness: an SVM Approach with Electromagnetic Methods*, 12th IMEKO TC10 Workshop on Technical Diagnostics, June 2013.
- H. G. Ramos, T. J. Rocha, D. J. Pasadas, A. L. Ribeiro, *Defect Detection with Velocity Induced Eddy Currents Effect Detection with Velocity Induced Eddy Currents Using a Permanent Magnet*, 18th International Workshop on Electromagnetic Nondestructive Evaluation (ENDE), June 2013.
- A. L. Ribeiro, H. G. Ramos, D. J. Pasadas, T. J. Rocha, *Using Giant Magneto-Resistance Sensors in Remote Field Eddy Current Tube Inspection*, IMEKO TC10 Workshop on Technical Diagnostics, June 2013.
- T. Rocha, D. J. Pasadas, A. L. Ribeiro, H. G. Ramos, *Defect Detection with Motion Induced Eddy Currents in Aluminum*, Conf. on Telecommunications (ConfTele), May 2013.
- D. J. Pasadas, T. J. Rocha, A. L. Ribeiro, H. G. Ramos, *Remote field eddy current testing of stainless steel tubes with GMR*, Conf. on Telecommunications (ConfTele), May 2013.
- H. G. Ramos, T. J. Rocha, D. J. Pasadas, A. L. Ribeiro, *Velocity Induced Eddy Currents Technique to Inspect Cracks in Moving Conducting Media*, IEEE Instrumentation and Measurement Technology Conf., May 2013.
- A. L. Ribeiro, H. G. Ramos, D. J. Pasadas, T. J. Rocha, *Remote Field Eddy Current Inspection of Metallic Tubes Using GMR Sensors*, IEEE Instrumentation and Measurement Technology Conf., May 2013.
- H. G. Ramos, T. J. Rocha, D. J. Pasadas, A. L. Ribeiro, *Eddy Current Nondestructive Testing Using Faraday Induction to Produce the Excitation*, IMEKO World Congress, October 2012.
- A. L. Ribeiro, H. G. Ramos, D. J. Pasadas, T. J. Rocha, *Image Processing of Data Obtained in Eddy Current Nondestructive Evaluation of Metallic Plates*, IMEKO World Congress, October 2012.
- A. L. Ribeiro, H. G. Ramos, D. J. Pasadas, T. J. Rocha, *Eddy Current Mapping Inside a Plane Conductor with Flaws*, Review of Progress in Quantitative Nondestructive Evaluation (QNDE), July 2012.
- H. G. Ramos, T. J. Rocha, D. J. Pasadas, A. L. Ribeiro, *Faraday Induction Effect Applied to the Detection of Defects in a Moving Plate*, Review of Progress in Quantitative Nondestructive Evaluation (QNDE), July 2012.
- T. J. Rocha, D. J. Pasadas, A. L. Ribeiro, H. G. Ramos, *Caracterization of Defects on Rivets using a Eddy Current Technique with GMRs*, IEEE International Instrumentation and Technology Conf. (I2MTC), May 2012.

- A. L. Ribeiro, H. G. Ramos, D. J. Pasadas, T. J. Rocha, *Current around a Crack in an Aluminum Plate under Nondestructive Evaluation Inspection*, IEEE Instrumentation and Measurement Technology Conf. (I2MTC), May 2012.
- H. G. Ramos, A. L. Ribeiro, D. J. Pasadas, T. J. Rocha, *Modeling Eddy Current Inspection of a Metallic Sample with Round Hole Defects*, IMEKO 17th Symp. IMEKO TC 4 - Measurement of Electrical Quantities, October 2011.